INVESTIGATION OF SPIN-TRANSFER TORQUE ON IRON GARNETS

A Dissertation

Presented to the Faculty of the Graduate School

of Cornell University

in Partial Fulfillment of the Requirements for the Degree of

Doctor of Philosophy

by

Colin L. Jermain

January 2017

INVESTIGATION OF SPIN-TRANSFER TORQUE ON IRON GARNETS

Colin L. Jermain, Ph.D.

Cornell University 2017

Spin-transfer torque provides an important mechanism for controlling thin films of magnetic material with thicknesses on the nanometer scale, and can significantly effect the orientation of a magnet to cause reversal and switching. I examine the iron garnets, yttrium iron garnet ($Y_3Fe_5O_{12}$, YIG) and lutetium iron garnet ($Lu_3Fe_5O_{12}$, LuIG), to investigate the interaction of spin-torque on electrically-insulating magnets. This insulating property prevents electrical current from shunting through the iron garnet magnet, which improves the amount of current available to generate spin-torque with the spin-Hall effect in an adjacent heavy metal. I demonstrate that nanometer-scale devices can be fabricated out of ultra-thin YIG and LuIG, and explore their switching behavior. I construct a ferromagnetic resonance measurement system to characterize the YIG and LuIG material and understand their properties. Using this system, I explore the magnetic damping in ultra-thin LuIG, and YIG at low-temperatures to explain the relaxation phenomena that occur in these systems. Overall, this research provides a significant step forward in understanding the properties of thin-films of iron garnet, and the feasibility of using spin-transfer torque on electrically-insulating materials.

BIOGRAPHICAL SKETCH

Colin Jermain was born on June 11th, 1989 to David and Kimberly Jermain, in the small town of Essex, Massachusetts USA. He grew up with his two brothers Aaron and Nate, and enjoyed getting outdoors - especially sailing. As he started racing sailboats, Colin developed his mechanical and problem solving skills, and applied them out on the water. In high school he discovered programming when learning how to use a graphing calculator, and from there developed his skills and started his own freelance business building websites. During that time, Colin achieved the Eagle Scout Award, an honor that both of his brothers also received.

Having a love of solving technical problems on both the software and hardware side, Colin attended the University of Massachusetts Amherst (UMass). During Freshman year, he decided to pursue a Physics degree, enjoying the mathematical rigor and the application of algebra and calculus to practical problems. Sophomore year, Colin joined the lab of Professor Mark Tuominen and lead a project to detect the Berezinskii-Kosterlitz-Thouless phase transition in superconducting vortices contained in fabricated nanostructures. Colin greatly enjoyed the breath of experiences he engaged in during this project; analyzing data with models, soldering pipes, drafting machine parts, writing automation software, fabricating nanometer-scale devices, among many other experiences. The mentorship and friendship of Professor Tuominen and the graduate students in the group greatly motivated Colin to continue his studies as a researcher. He enjoyed working in the UMass clean-room so much, that he decided to pursue a graduate program that had the facilities to support nanometer-scale research, of which Cornell is one of the best.

Joining Cornell University as a graduate student, Colin met Professor Dan Ralph at the annual Cornell Nanofabrication Facility (CNF) meeting. He took an opportunity to work in Professor Ralph's lab, and the rest is the subject of this thesis. During his time at Cornell, Colin remained engaged with his software and business aspirations; publishing open-source software to solve research problems and leading the graduate entrepreneurship club (Technology Entrepreneurship at Cornell). Moving forward, he looks to take his scientific problem solving and analytic skills back to the business world and apply them to building products and businesses.

To my brothers Aaron and Nate.

ACKNOWLEDGEMENTS

There are many people that have helped me along the way in putting together this thesis. I would like to take this opportunity to thank my colleagues, friends, and family for their support.

First, I would like to thank Professor Dan Ralph for his consistent encouragement and support throughout the process. He has always provided insightful suggestions on the physical mechanisms that I have encountered through out my work. I appreciate the care that he takes to deliver constructive feedback, and his aptitude for teaching aspiring scientists. He has also taught me a great deal on how to tell a story from a scientific experiment, and the elements of leading the reader through the details.

I would also like to thank Professor Robert Buhrman for his insights and suggestions on the scientific papers that we have worked on together. In many ways, I have benefited from the resources and facilities in the Buhrman group, and I appreciate this support.

I would like to acknowledge Sriharsha Aradhya for providing a voice of reason on many occasions. His significant mentorship and support as a sounding board has lead to many fruitful discussions and breakthroughs. He has played a major role in the majority of my research, and I am deeply grateful for this.

I would like to acknowledge Graham Rowlands for his mentorship on magnetic computations and modeling. I have enjoyed our mutual passion for software, and through this lens he has taught me a great deal about magnetism. This has also lead to the publication of research software from projects we have collaborated on, that has been an important facilitator for my research.

I would like to acknowledge the many collaborators that I have worked with throughout my research. Aaron Rosenberg has been extremely easy to work

with. I appreciate his careful scanning SQUID measurements, and the fluid communication that we have had, which makes a long-distance collaboration possible. John Kirtley, Professor Katja Nowack, and Professor Kathryn Moler have also played an important role in these scanning SQUID measurements. I would like to acknowledge Hanjong Paik for his considerable work in growing iron garnets through molecular-beam epitaxy. His insights into the crystal structure and characterization have made a significant impact on my work, and the films he has grown were essential to it. Professor Darrell Schlom also gave advice on these crystals and enabled our research. I would like to acknowledge Professor Fengyuan Yang for facilitating the growth of yttrium iron garnet films (grown by Jack Brangham and Hailong Wang), and our many conversations on the ferromagnetic properties. I appreciate Jason Bartell for his significant work in characterizing the yttrium iron garnet devices using the longitudinal Spin-Seebeck effect, and his insights into their magnetic properties. Professor Greg Fuchs also made significant contributions, and I appreciate that he has always been open to discussion and provided sound advice.

From the Buhrman group, Praveen Gowtham and Junbo Park have provided significant mentorship to me over the years. I would also like to acknowledge Neal Reynolds for his enthusiasm and excitement, and for being a great office-mate over the years. I also appreciate the Ralph, Buhrman, and Fuchs group members (past and present); Eugenia Tam, Ted Gudmundsen, Chen Wang, Lin Xue, Wan Li, Alex Mellnik, Colin Heikes, Marcos Guimaraes, David MacNeill, Jen Grab, Greg Steihl, Jonathan Gibbons, Ruofan Li, Alexander Molina Schlotterback, Alison Rugar, Minh-Hai Nguyen, Yongxi Ou, Shengjie Shi, Ryan Tapping, Chi-Feng Pai, Luqiao Liu, Luis Leao, Feng Guo, Darryl Ngai, among others.

I would like to acknowledge Nate Ellis for teaching me how to machine. His design and mechanical insights have been essential to the success of the ferromagnetic resonance system, and his friendly advice has always been appreciated. I am also grateful to the Clark Hall machinists, particularly Rodney Bowman, for always being open to help.

There are many members of the Cornell Nanofabrication Facility (CNF) staff that have shared their advice and expertise, for which I am greatly indebted. Noah Clay, Rob Illic, Daron Westly, John Treichler, Aaron Windsor, Garry Bordonaro, Alan Bleier, Tom Pennell, among others, have greatly helped to guide and facilitate the device fabrication part of my research. I would also like to acknowledge Jon Shu, Steve Kriske, and Darren Dale at the Cornell Center for Materials Research (CCMR), who have facilitated many of the necessary instruments for these studies, and given advice and training on their use. I also appreciate Maura Weathers, for her help in X-ray measurements. Boris Dzikovski and Curt Dunnam, also shared their considerable expertise in electron-spin resonance and cavity systems, that was essential to the low-temperature cavity experiments.

I am greatly indebted to Pamela Nasr for her constant support and encouragement throughout this process. I am also grateful for the support and encouragement from my family and friends.

TABLE OF CONTENTS

LIST OF TABLES

LIST OF FIGURES

CHAPTER 1

INTRODUCTION

Understanding the physical mechanisms that control the orientation of a magnetic moment provides important groundwork for improving computing and memory technologies, which use the non-volatile magnetic moment to represent a logical state. While the application of a magnetic field can reorient a magnet, the long-range nature of a sufficiently strong magnetic field can have adverse effects on other magnets in proximity. In a dense group of devices, there is a significant advantage to use an interfacial mechanism that can act directly on the magnet of interest. In this chapter, I provide an overview of the interfacial mechanism of spin-transfer torque, which has been shown in metallic ferromagnets to reliably switch the magnetic orientation of an adjacent layer. The focus of this dissertation is to extend these experiments to explore iron garnets, which are electrically-insulating magnetic materials that have promising advantages over previous materials. I conclude this chapter with an overview of the dissertation.

1.1 Spin-transfer torque

The orientation of a magnetic material evolves in time based on the Landau-Lifshitz-Gilbert (LLG) equation.

$$\frac{d\vec{m}}{dt} = -\gamma\vec{m} \times \vec{H}_{\text{eff}} + \alpha\vec{m} \times \frac{d\vec{m}}{dt} \tag{1.1}$$

Here, the magnetization unit vector $\vec{m} = \vec{M}/M_s$ is the total moment $\vec{M}$ over the saturation magnetization M_s. The first term expresses the precessional motion

of the magnetization around the effective field $\vec{H}_{\text{eff}}$, in terms of the gyromagnetic ratio γ. The effective field $\vec{H}_{\text{eff}}$ combine the effects of an applied external field, demagnetization, anisotropy, and other behavior that contributes to the free energy F of the magnetization. From the free energy, the effective field can be derived as $\vec{H}_{\text{eff}} = -\frac{\partial F}{\partial \vec{M}}$ [4]. The second term represents the damping motion that brings the magnetization into alignment with the effective field, in terms of the Gilbert damping coefficient α. Equation 1.1 illustrates that the free energy landscape of the magnetic moment dictates the orientation of the moment, which can be actuated by changing the applied field.

Spin-transfer torque provides a method for affecting the magnetic orientation without an applied field, by transferring spin-angular momentum to the magnet at the interface. Slonczewski initially developed the expression for spin-transfer torque, with which we can extend the LLG equation [5].

$$\frac{d\vec{m}}{dt} = -\gamma\vec{m} \times \vec{H}_{\text{eff}} + \alpha\vec{m} \times \frac{d\vec{m}}{dt} + \gamma\frac{\hbar}{2\mu_o M_s t} J_s(\vec{m} \times \vec{\sigma} \times \vec{m}) \tag{1.2}$$

The third term expresses the spin-transfer torque in terms of the reduced Plank's constant $\hbar$, the permeability of free space μ_o, the thickness of the magnetic material t, the spin-current density J_s and the spin polarization $\vec{\sigma}$. For very thin films ($t \lesssim 20$ nm) and large spin-current densities, this term can become sufficiently large to compete with the damping term. When $\vec{\sigma}$ is along $\vec{H}_{\text{eff}}$ the spin-transfer torque increases the damping. However, when $\vec{\sigma}$ is anti-aligned with $\vec{H}_{\text{eff}}$ the spin-transfer torque acts against the damping, as an anti-damping torque that can reverse the state of the magnet. This depends on the strength of the spin-current density and the direction of the spin polarization. In Eq. (1.2), there is also the possibility of an effective-field spin-orbit torque that goes as $\vec{\sigma} \times \vec{m}$,

which expresses the exchange magnetic field from the spin accumulation. This effective-field term is typically small in comparison to Slonczewski term, and can be considered as an addition to $\vec{H}_{\text{eff}}$ (although it does not conserve energy). Overall, spin-transfer torque motivates the need for efficient generation of spin current.

The spin-Hall effect provides an effective method for generating a spin current. In heavy metals such as Pt [6], β-Ta [1], and β-W [7] the spin-orbit coupling causes spin-dependent scattering of the conduction electrons, so that at the interfaces there is a net spin-polarization. This produces a net spin current with an efficiency governed by the spin-Hall angle θ_{SH}, and involves the electron charge e.

$$\vec{J_s} = \theta_{\text{SH}} \frac{\hbar}{2e} \vec{\sigma} \times \vec{J_c} \tag{1.3}$$

Here the spin polarization and charge current density $\vec{J_c}$ directions produce a perpendicular spin-current density $\vec{J_s}$ that can be used to affect an adjacent magnetic material with spin-transfer torque. The sign of θ_{SH} and the direction of the charge current determine if the spin-transfer torque acts as a damping or as an anti-damping torque.

1.2 Iron garnets

Iron garnets are of interest for spin-transfer torque since they are electrically-insulating and can have low magnetic damping. In this work, I focus on yttrium iron garnet ($Y_3Fe_5O_{12}$, YIG) and lutetium iron garnet ($Lu_3Fe_5O_{12}$, LuIG), where

the Fe^{3+} ions exclusively provide the magnetism and leads to common material properties among the two materials. The lack of conduction electrons allows iron garnets to have significantly reduced damping compared to metallic ferromagnets, since in metals conduction electrons couple to the lattice to provide additional relaxation channels. The low damping provides one of the main motivations for exploring iron garnets, since lowering the damping increases the effect of spin-transfer torque in an anti-damping reversal. As we will discuss in Chapters 3, 4, and 5 my work has encountered many other loss mechanisms that can affect the actual damping values in a thin-film device with an adjacent spin-Hall material. However, there is considerable opportunity to improve in these areas.

Iron garnets have a complex crystal structure, which differs considerably from metallic ferromagnets such as CoFeB and NiFe (Py), which are typically grown as amorphous films. In YIG, each unit cell has 8 formula units of $Y_3Fe_5O_{12}$, yielding 24 Y^{3+}, 40 Fe^{3+}, and 96 O^{2-} ions [8]. Of the magnetic Fe^{3+} ions, 16 occupy *a*-sites surrounded by 6 O^{2-} ions (octahedral) and 24 occupy *d*-sites surrounded by 4 O^{2-} ions (tetrahedral). The symmetry of the oxygen *p*-orbital with respect to the iron *d*-orbital and the bond angle between the *a*- and *d*-sites (126.6°) is responsible for the super-exchange interaction, which causes anti-ferromagnetic coupling between the *a*- and *d*-site iron ions [4, 8]. This coupling forms anti-aligned magnetic sub-lattices in a ferrimagnetic configuration. The difference in the population of *a*- and *d*-site Fe^{3+} ions provides a net moment. On length scales greater than a nanometer YIG and LuIG behave as ferromagnets.

The electrically-insulating property of iron garnets eliminates an important

loss mechanism in spin-current generation adjacent to metallic ferromagnets, where the charge current can be shunted into the magnet instead of generating spin current in the adjacent layer. This can provide improvement for the efficiency of spin-transfer torque in spin-Hall metals. Topological insulators, which show promising spin-current generation [9, 10], can have a significant improvement in spin-transfer torque efficiency, since these materials are highly resistive and are more susceptible to shunting loses.

1.3 Outline for the dissertation

Exploring the use of spin-transfer torque on iron garnets is the focus of this dissertation. Throughout the work, we collaborated with groups who are experts at growing iron garnets. This necessitated the characterization of the iron garnet material that we received, to understand the magnetic properties and predict their impact on the use of spin-torque. In Chapter 2, I introduce the ferromagnetic resonance (FMR) system that I built to measure the magnetic damping of iron garnet films. Since the growth of ultra-thin iron garnets (less than 20 nm) is still being optimized, the FMR system became an important tool in understanding the growth process. In collaboration with the Schlom group at Cornell University, I characterized lutetium iron garnet films that were the first to be grown by molecular-beam epitaxy, and extended the viable thickness of iron garnets below 10 nm [2]. Chapter 3 details the measurements on lutetium iron garnet films, and examines the effect of two-magnon scattering at these thicknesses.

Our low-temperature measurement technique for investigating spin-torque on iron garnet magnets motivated a comprehensive study of the damping

behavior at these temperatures. Working with members of the Ralph and Buhrman groups at Cornell University, I extended the FMR capability of our room temperature system to work at cryogenic temperatures. I used this cryogenic FMR system to study the behavior of yttrium iron garnet films grown by off-axis sputtering, in collaboration with the Yang group at Ohio State University. I discuss the dramatic damping increase that we observe at low-temperatures in Chapter 4, and present frequency-dependent data that suggests a slowly-relaxing impurity mechanism is responsible. The additional magnetic characterization of the saturation magnetization and effective magnetization provide important insight into the spin-torque effect.

In Chapter 5, I present the spin-torque experiments on iron garnet nanomagnets. I demonstrate the fabrication technique for building devices of iron garnet on the nanometer-scale, and highlight the challenges in working with the material. We collaborate with the Moler group at Stanford University, who are experts in detecting magnetic fields using scanning Superconducting Quantum Interference Device (SQUID) magnetometry. We demonstrate that the scanning SQUID provides an accurate method for determining the state of our nanomagnet device, but we do not observe spin-torque driven switching in our devices. Using the magnetic characterization of our earlier measurements, I present estimates for the critical current required for a single-domain magnet to switch by anti-damping spin-torque. In light of these estimates, I suggest future improvements for the device design and material properties. I conclude the thesis in Chapter 6, by presenting two additional experiments that demonstrate electrical characterization of spin-transfer torque on iron garnets, and build important groundwork for future experiments.

CHAPTER 2

FERROMAGNETIC RESONANCE MEASUREMENT SYSTEM

2.1 Introduction

Recent advances in the growth of iron garnet films necessitate their magnetic characterization, to both ensure their quality for applications and understand the growth mechanisms. Ferromagnetic resonance (FMR) provides a technique to determine the magnetic damping, effective magnetization, and anisotropy fields, which are essential to using these films in spin-transfer torque devices. The FMR technique relies on the application of two magnetic fields; a large static field $\vec{H}$ that saturates the magnetic moment, and a small field $\vec{h}$ at GHz-frequency f that excites a precessional motion around the static field direction (Fig. 2.1(a)). When H reaches the resonance field H_r for the given frequency f, the sample absorbs the microwave power of the GHz field. The detection of changes in the microwave power P provides a precise measurement of the resonance condition.

The earliest FMR measurements of bulk crystalline iron garnets were performed in resonance cavity systems [11] (Fig. 2.1(b)), which apply a uniform $\vec{h}$ field across the sample. These cavity systems are limited to a narrow band in frequency, typically around 9.4 GHz and other specific values. Without multiple cavities of different resonance frequencies, broadband measurements are not possible in this configuration. This prevents the measurement of the magnetic damping and effective magnetization, which are determined by the frequency dependence of the FMR linewidth and resonance field respectively.

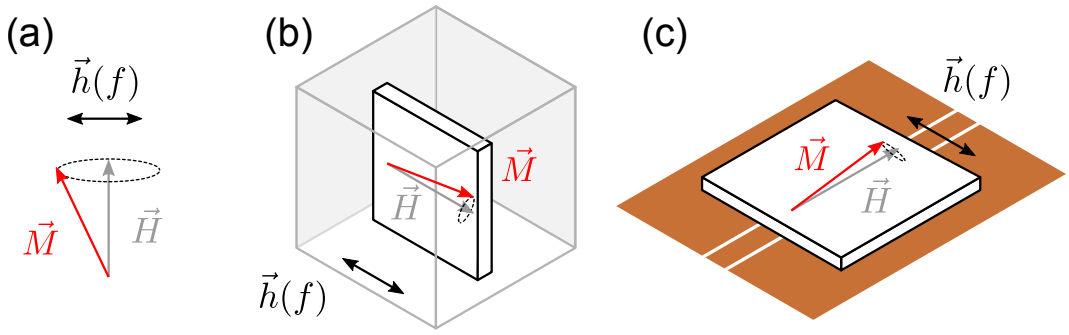

Figure 2.1: (a) Illustration of the ferromagnetic resonance precession, showing the magnetic moment $\vec{M}$ which rotates around the static applied-field $\vec{H}$, excited by the microwave field $\vec{h}$. This excitation field is generated by either a (b) resonant cavity or a (c) broadband waveguide.

To overcome these limitations, broadband ferromagnetic resonance systems were developed that use the Oersted-field that emanates from a waveguide to excite the precession [12, 13] (Fig. 2.1(c)). These planar waveguides are particularly well suited for the excitation of thin films of magnetic material, where the sample can be simply placed adjacent to the waveguide to be in proximity of the localized $\vec{h}$ field. However, the caveat of broadband systems is that their quality factor, proportional to their signal-to-noise, is significantly worse than cavity systems. This is partially a result that resonance cavities excite the full volume of the sample, while broadband systems only excite the region directly above the waveguide. In Chapter 4, I present FMR measurements using both types of systems. Despite the signal-to-noise reduction, the necessity to determine the magnetic damping from the frequency dependence motivates the use of broadband systems, and in practice the signal-to-noise is sufficient to make precise quantitative statements about the relevant parameters.

In this chapter, I discuss the construction of a broadband FMR system that I built to characterize iron garnet films. Building off of the work of Kalarickal *et al.*

and Bilzer *et al.* [12, 13], I made unique improvements to the FMR system that enhance the precision and efficiency of conducting measurements. Most notably, I discuss the use of power-modulation in tandem with field-modulation to provide enhanced noise rejection. I also discuss the lock-in detection and acquisition scheme that enables rapid measurements with a high degree of precision that I developed to reduce the measurement time. While discussing the overall operation of the apparatus, I present these improvements and suggestions for future enhancements, which can significantly impact the characterization of both iron garnet films specifically, and magnetic materials in general. This system provides the basis for the measurements of Chapter 3 and 4.

2.2 Measurement apparatus

2.2.1 Field and power modulation

Conventional FMR systems use field-modulation to achieve a high sensitivity by rejecting signals that are not field-dependent [12]. In this mode, the FMR spectra represents the derivative power absorption dP/dH. In early versions of the FMR system, I experienced significant noise in the FMR spectra, rectified by the lock-in amplifiers as an offset in dP/dH. The most significant source is the unsheilded RF cables, which pick up the field-modulation from the Helmholtz coils. Given the limited dynamic range of a lock-in amplifier, the noise offset reduces the precision of the measurement and introduces an additional fitting parameter, which can in some cases depend on field or frequency (i.e. the background can be difficult to remove in the analysis stage).

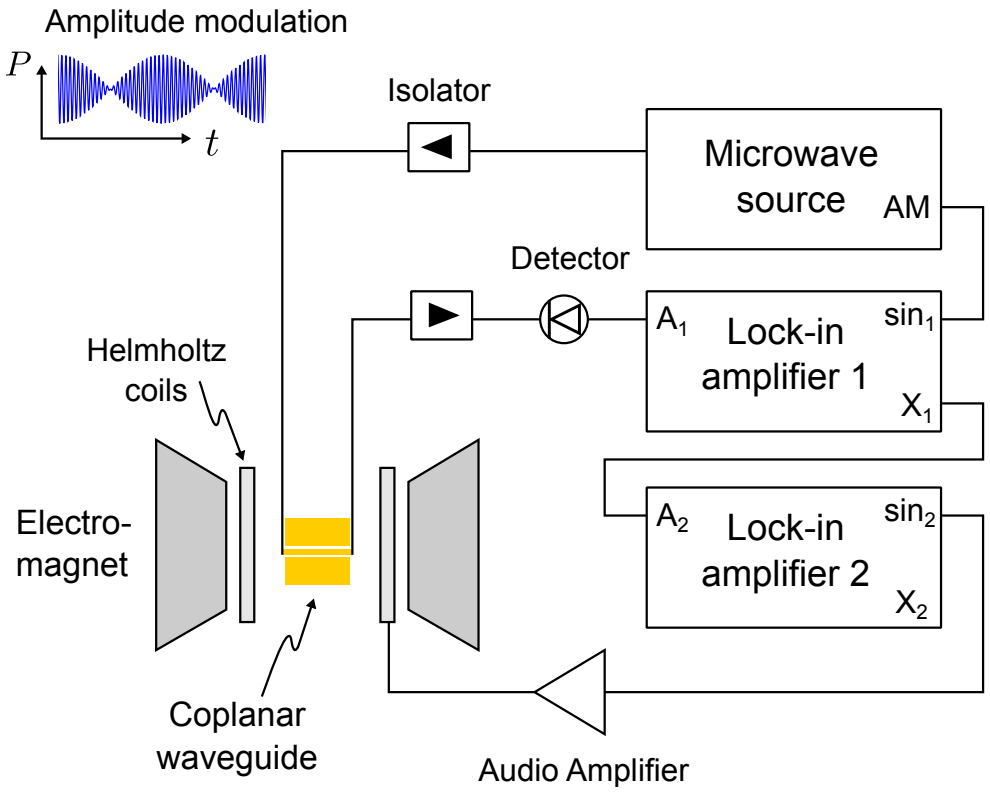

Figure 2.2: Schematic of the broadband FMR system.

I extended the field-modulation technique by introducing power-modulation in tandem. Since the FMR spectra is strictly proportional to the RF power (in the linear regime), the tandem modulated signal has the same lineshape as the conventional field-modulated signal. Therefore, the analysis of the FMR spectra is the same. Changing the strength of the field from the Helmholtz coils does not introduce an offset in this mode, which is a significant advantage when using large modulation fields to detect broad resonances.

Figure 2.2 shows a schematic of our FMR system. I use an Anritsu MG3692C microwave source to provide the RF power between 0.1 and 20 GHz, which flows over 50 Ω flexible cables (Fairview Microwave SKPS086-048B model) to

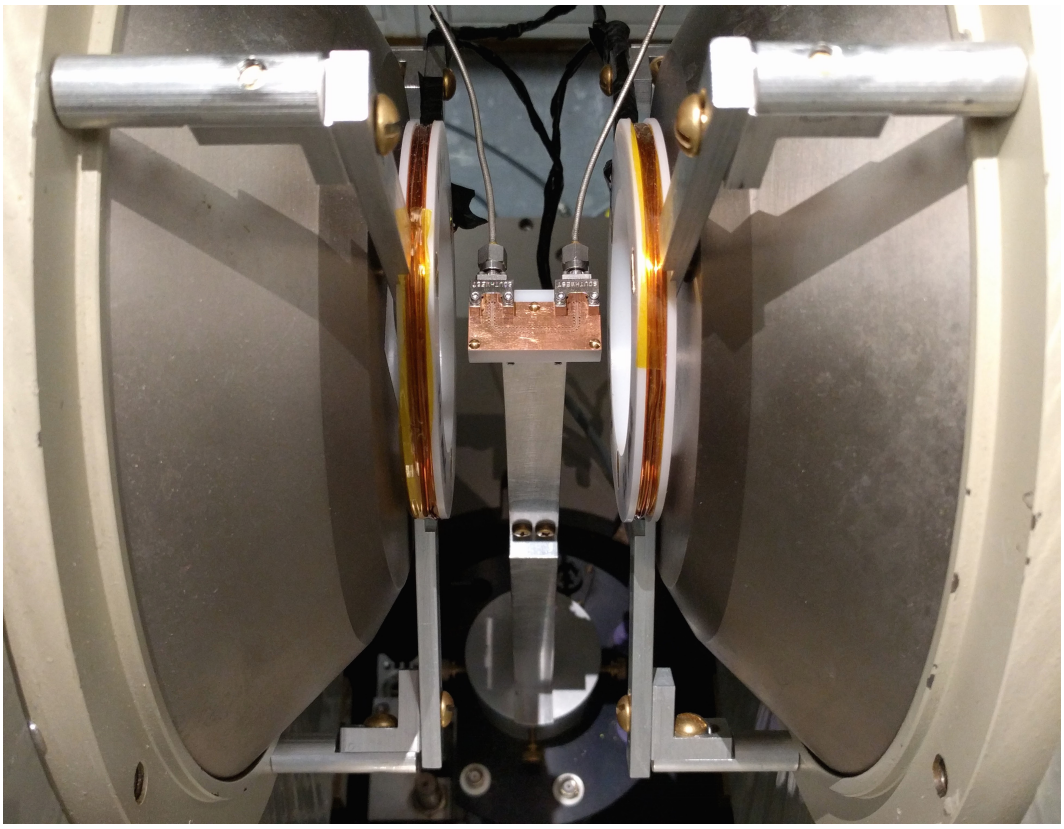

Figure 2.3: Photograph of the coplanar waveguide and Helmholtz coils mounted in the electromagnet.

the coplanar waveguide. We modulate the amplitude of this RF power at 101.97 kHz, using the external synchronization from lock-in amplifier 1. Therefore the power $P(t)$ represents a beat-frequency with kHz and GHz frequencies, as illustrated in Fig. 2.2. Two isolators, implemented as broadband directional couplers with 50 Ω loads at the reflection end, damp out reflections in the microwave circuit to provide considerable signal-to-noise improvement. The sample, placed on the coplanar waveguide, absorbs RF power when the applied field from the electromagnet matches the resonance condition for the given GHz frequency. The detector diode (Agilent 8474E model) converts the power to an voltage that we measure in lock-in amplifier 1. All the lock-in amplifiers in the system are Stanford SR830 models, which are convenient, since they provide a

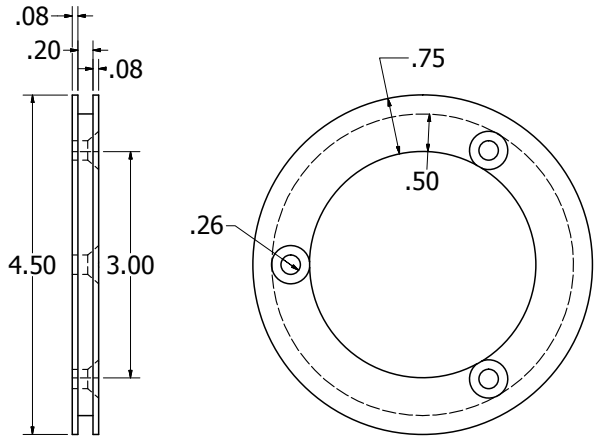

Figure 2.4: Schematic of the Helmholtz coil spool, made of Delrin. All dimensions are in inches.

fast-output with 100 kHz bandwidth that generates a ±10 V signal proportional to the X or Y channel.

The first lock-in amplifier rectifies the kHz power-modulation. Using a time constant of 30 μs, lower frequency signals (than roughly 5 kHz) are passed through to the fast-output, which allows the field-modulation to be performed in tandem. I adjust the phase of this first lock-in amplifer such that the full signal is on the X channel. The fast-output for X is then connected to the input of lock-in amplifier 2, which rectifies the field-modulation.

The Helmholtz coils [14, 15] provide the AC field for the field-modulation that we superimpose on the applied-field from the electromagnet. I built the coils by first machining spools out of Delrin with a 3" inner diameter. Figure 2.4 shows the coil spool schematic. Each spool contains 25 wraps of 20 AWG magnet wire, which are secured with wraps of Kapton tape. To mount the coils to our GMW 3474 electromagnet, I designed an adjustable system with three points of contact to the coils, so that they could be rigidly attached. The rigidity

of the coils helps to reduce the measurement noise. In the electromagnet, the distance between the coils is roughly 2.5". While this distance is slightly out of the Helmholtz configuration, it does not significantly impact the field uniformity in the region of interest. I amplify the sine voltage signal from the second lock-in amplifier with a Europower EP4000 audio amplifier, and monitor the AC current that flows across the circuit with an analog meter. Driving the coils at 1.9211 kHz, the circuit impedance of 5.4 Ω provides the load by which current flows when the voltage is applied by the amplifier. The coils produce 5.4 Oe/A with a maximum of 40 Oe at 7.4 A. To provide reproducible measurements, the sine voltage amplitude, digitally controlled by the second lock-in amplifier, actuates the AC current and resulting AC field. I calibrated the system so that the field per sine voltage amplitude is 8 Oe/V, which can take values from 4 mV to 5 V.

2.2.2 Time efficient measurements

The importance of measuring FMR at many frequencies to determine the damping and effective magnetization motivates optimizing the time efficiency of a single measurement. After building an initial system that swept the field in a digital step sequence, I found this technique to be limited by the stabilization time required at each field, the cost of which is amplified by the number of field points in the scan. Instead of sweeping the field in this manor, the final system that I present continuously sweeps the field over a few minutes and synchronously measures the derivative absorption and field at each moment. This has the significant advantage that the sweep time can be adjusted in conjunction with the time constant of the field-modulation lock-in amplifier to achieve sig-

nal averaging in a time efficient way. In addition, the number of sample points can be significantly higher without affecting the efficiency.

I measure the applied field of the electromagnet during the sweep using lock-in amplification. A third lock-in amplifier provides a sine voltage signal to an AKM Semiconductor HG-302A Hall probe, and measures the resulting voltage proportional to the applied field. Using a frequency of 99.66 kHz, the applied field rejects the AC field-modulation at 1.9211 kHz, which is a significant advantage to this technique. The time constants of the second and third lock-in amplifiers are set to the same value to ensure a consistent relationship to the sweep time. The caveat of this approach is that the dynamic range of the third lock-in amplifier restricts the overall field range of the system. In the interest of measuring sharp iron garnet linewidths, I optimized the sensitivity and offset of the third amplifier to enable measurements with 0.1 Oe field precision between 0 and 4.5 kOe. I calibrate the Hall probe by correlating the current applied by the electromagnet power supply, the X channel voltage measured by the Hall probe, and the field measured by a gaussmeter. In practice, I find these quantities to scale linearly.

The system acquires the ±10 V fast-output of the X and Y channels of the second and third lock-in amplifiers through a data acquisition board (National Instruments PCI-6052E and BNC-2110). This provides a 16-bit representation of the analog voltage, which can be acquired significantly faster than the time scale of the continuous field sweep. I adjust the phase of the second lock-in amplifier so that the derivative absorption occurs on the X channel. In practice, this phase adjustment is important to update when using new samples.

I built measurement software that plots the FMR spectra in real-time as they

are acquired. The details of this software are discussed in Appendix A. The software makes use of the PyMeasure package that I developed in collaboration with a number of colleagues. The advantage of this software is that multiple frequencies can be scheduled to run in succession, which greatly enhances the efficiency of running a broadband set of measurements. Overall, a full broadband measurement can be made in less than 1 hour, where each scan takes roughly 3-5 minutes depending on the desired averaging.

2.2.3 Broadband coplanar waveguide

In our broadband system, the impedance governs the power transmission through the waveguide. Minute changes in the capacitance and inductance over parts of the RF circuit can dramatically reduce the transmission, since these are amplified by the large GHz-frequency. Therefore, the design of the coplanar waveguide and the connections to it are of particular importance. I used both existing technical reports [16], books on coplanar waveguides [17–19], and finite-element simulations in Sonnet to optimize the waveguide design to approach 50 Ω impedance.

Figure 2.5 shows the schematic of the coplanar waveguide. The limited pole gap of the electromagnet sets the overall dimensions of the board and the connector locations, introducing a bend in the waveguide to allow the connectors to come out adjacent to the poles. I ordered a batch of over 20 boards from PCB Universe (Vancouver, Washington) on the substrate Rogers 4003 of 12 mil thickness. Using two ounce copper gives a metal thickness of 2.6 mil. The channel width and spacing are 18.5 and 5 mil respectively, which I calculated to achieve

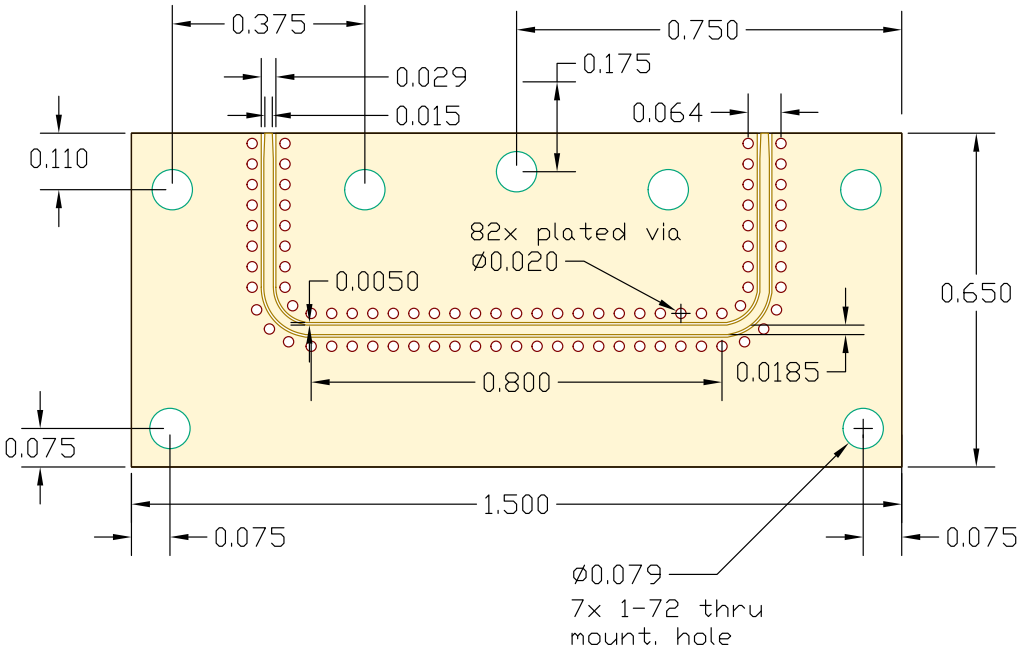

Figure 2.5: Schematic of the coplanar waveguide for the FMR system. Dimensions are in inches.

a 50.09 Ω impedance at GHz-frequencies given the substrate and metal properties. I designed the tapper in the launch geometry, where the RF connectors attach, based on a technical report by Southwest Microwave (Tempa, Arizona) that pertains to their board-mountable connectors [16]. I use the Southwest Microwave 292-07A-5 SMA connectors, which are advantageous in that they can be easily replaced, do not require soldering, and are reasonably non-magnetic. The diameter of the connector pin, which connects to the center line of the coplanar waveguide, governs the tapper in the launch geometry. Figure 2.6 shows a photograph of the assembled coplanar waveguide and SMA connectors.

I measure the frequency-dependent transmission of the coplanar waveguide and circuit using a vector network analyzer (VNA). Figure 2.7 shows the transmission (S_{21}) and reflection (S_{11}) scattering parameters as a function of fre-

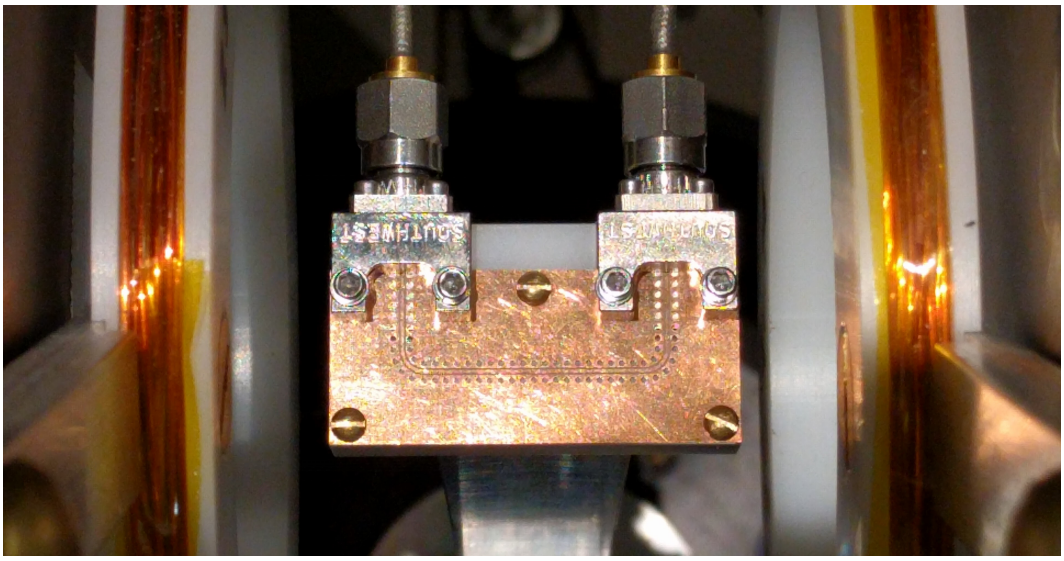

Figure 2.6: Photograph of the assembled coplanar waveguide and SMA connectors.

quency (f). The transmission losses are smaller than -5 dB up to 30 GHz, which is a good performance for a waveguide intended for a 0.1 to 20 GHz operating bandwidth. I explored a number of other waveguide designs, including a stripline geometry, but found this original design had the best transmission performance. In Fig. 2.7, the increasing transmission losses at higher frequencies illustrate why frequency modulation is not practical for FMR, since the transmission changes would distort the measurement.

2.2.4 Field-orientation mounts

I built two mounting systems for the coplanar waveguide to enable applied-fields with both in-plane and out-of-plane orientation. Since our GMW 3474 electromagnet was previously employed as a vibrating sample magnetometer (VSM), it has a circular mount of 2" inner diameter that has four screws, which

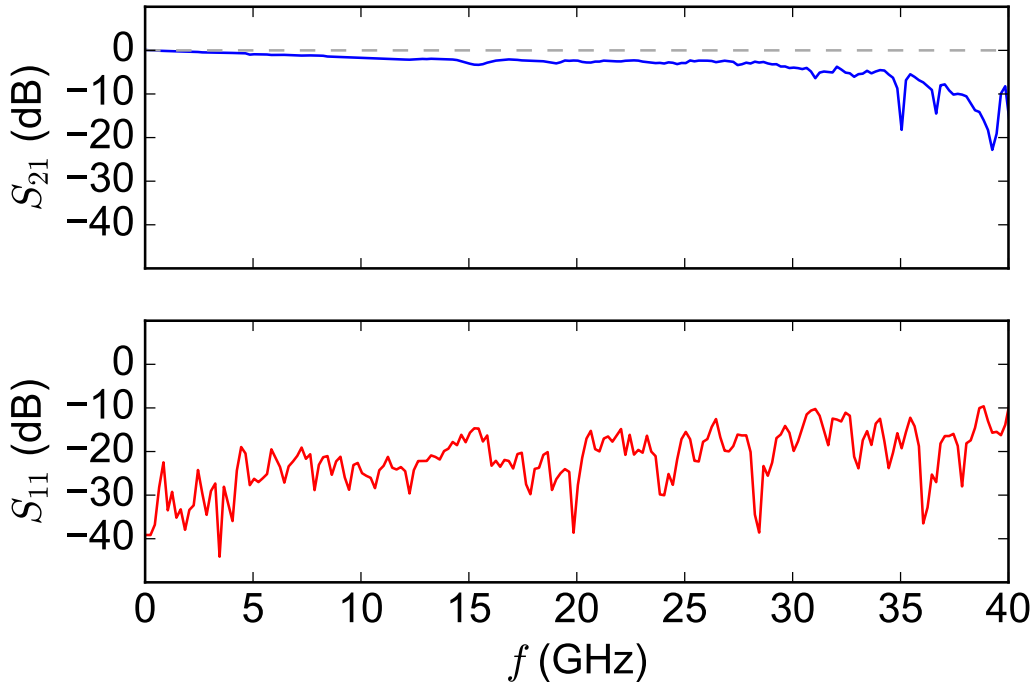

Figure 2.7: Scattering parameters of the coplanar waveguide, showing the (solid blue) transmission (S_{21}) and (solid red) reflection (S_{11}) as a function of frequency (f).

can be tightened to secure a boss feature. This allows mounts to be made that rigidly hold the waveguide in the uniform field of both the electromagnet and the Helmholtz coils. By machining two mounts, one perpendicular and another parallel to the pole faces, we can apply in-plane and out-of-plane fields.

Figure 2.8 shows the mounting systems for both in- and out-of-plane applied-fields. The sample sits on the waveguide, film-side down, with Kapton tape to secure it if necessary. The waveguide excites the region of the film placed on the waveguide, which is an important distinction in samples that vary in composition across the sample area. I address these effects in Sections 3.3.3, with the FMR data.

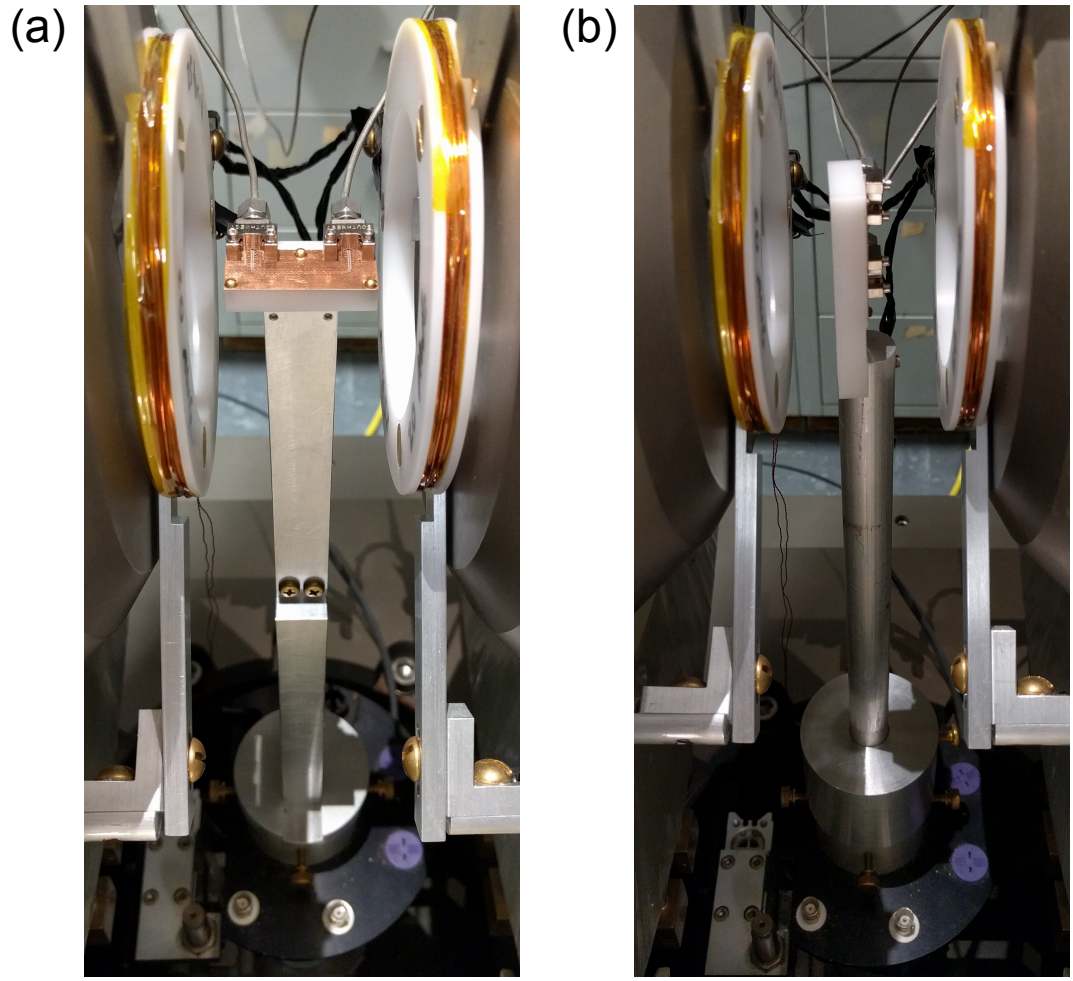

Figure 2.8: Photographs of the mounting systems for (a) in-plane and (b) out-of-plane applied magnetic fields. The same coplanar waveguide and launch connectors are used in both systems.

2.3 Discussion

While the introduction of power-modulation and the time efficiency improvements greatly enhance the accuracy and practicality of the FMR system, there are additional enhancements that can be made. In this section, I discuss three separate areas of the setup that can be improved and outline strategies for implementing them. These areas are the field detection, sample timing, and waveguide design.

As discussed in Section 2.2.2, we use a Hall probe and lock-in amplifier to measure the applied magnetic field. Although this technique has the considerable advantage that it rejects the AC field modulation and provides significant precision, it suffers the disadvantage that the field range is limited by the lock-in sensitivity. Currently this field range is set once by adjusting the lock-in amplifier settings to make the best use of the range, and then calibrating the Hall probe to determine the voltage-field relation. There are two possible solutions to problem: (i) include an analog circuit to controllably subtract from the Hall voltage signal, and (ii) use multiple ranges that have increasing sensitivity and decreasing precision at higher fields. Option (i) requires the use of an instrumentation amplifier to perform the analog subtraction. The difficulty in this method is that the signal is oscillating, so a phase-locking component must be included in the circuit. Option (ii) is considerably easier to implement, since it can be done purely in the software. By storing the lock-in amplifier settings for each range, including the sensitivity, offset, and expansion parameters, each range can be loaded into the amplifier on demand. Calibration curves for the voltage and field are needed for each range, but this capability is a simple extension of the existing calibration software. The disadvantage of option (ii) is that each increasing sensitivity range yields less precession when represented by the 16-bit DAQ. Luckily, the linewidth of YIG films increase with increasing field, so that the 0.1 Oe precision in the current design is not necessary for resonances with resonance fields above 4 kOe. Implementing the multiple field range method can enable YIG measurements to higher frequencies that those presented in Chapters 3 and 4, and open up the potential for higher field measurements on other materials.

The system allows the user to control both the measurement time for the

analog sweep of field, and the time constant over which to average the sample. However, this leaves the user to determine the appropriate settings to achieve accurate measurements. If the time constant is too long, then the FMR spectra acquires a low-pass filtering that may not be obvious to inexperienced users. To balance the sweep time with the time constant, the software can be improved to give a suggestion for the optimal time constant once the user enters the sweep time, and vice versa. The suggestion can ensure that each sample is measured after 5 times the time constant. This can improve the measurements of novice users, and simplify the optimization of parameters, while allowing more advanced users to still have direct control of the settings.

The waveguide design places considerable restrictions on the pole gap in the electromagnet, as well as the distance between the Helmholtz coils (and therefore the coil radius). This limits the total field that both the electromagnet and the coils can produce. In our system, the Helmholtz coils are most affected, where the AC field scales inversely with the radius. Therefore, the reduction of the overall dimensions of the waveguide can enable higher AC fields at the same current level. This would improve the measurement of broad linewidths, and reduce the heating that occurs at AC fields above 20 Oe RMS. The use of micro-miniature (SMPM) RF connectors can enable significantly reduced waveguide dimensions, compared to the SMA connectors currently in use. We use these SMPM connectors in the low-temperature FMR system described in Chapter 4. The coplanar waveguide design from Section 2.5 can be adapted to a straight design, with side-mount SMPM connectors. With proper design, the waveguide and connectors can be reduced from taking roughly 1.75″ down to 1″. A 1.5″ pair of Helmholtz coils can increase the AC field strength by over 160% relative to the 2.5″ gap in the present design. This improvement takes considerable

modification to the system, but can enable research on materials with broad linewidths.

2.4 Conclusion

In this chapter, I have presented our FMR system and the unique improvements that I made to enhance the accuracy and efficiency of characterizing magnetic films. The suggestions that I make in Section 2.3 provide an outline for future improvements to the field capability, ease of use, and linewidth detection. Overall, the system facilitates the characterization of the magnetic damping and relaxation process, which are fundamental for spin-transfer torque research and the understanding of anti-damping torque. Besides iron garnets, the system has been used to measure multi-layer CoFeB devices, spin-pumping in rare-earth metals, and a number of conducting magnetic systems. In Chapters 3 and 4, I describe the measurements that I performed using the system to characterize ultra-thin iron garnets and explore loss mechanisms at low-temperatures in yttrium iron garnet.

CHAPTER 3

DAMPING CHARACTERIZATION OF ULTRA-THIN LUIG FILMS

3.1 Introduction

Insulating ferrimagnets are of interest for spintronic applications because they can possess very small damping parameters, as low as 10^{-5} in the bulk [11]. They also provide the potential for improving the efficiency of magnetic manipulation using spin-orbit torques from heavy metals [1, 20] and topological insulators [9, 10], because ferrimagnetic insulators will not shunt an applied charge current away from the material generating the spin-orbit torque (discussed further in Chapter 5). Making practical devices from ferrimagnetic insulators requires techniques capable of growing very thin films (a few tens of nm and below) while maintaining low damping. Much of the previous research in this field has focused on yttrium iron garnet ($Y_3Fe_5O_{12}$, YIG) grown by pulsed-laser deposition or off-axis sputtering [21–25], but YIG is just one in a family of rare earth iron garnets with potentially useful properties [26].

In this chapter, we examine the magnetic and structural properties of thin, (111)-oriented films of lutetium iron garnet ($Lu_3Fe_5O_{12}$, LuIG) grown by an alternative method, molecular-beam epitaxy (MBE) [27]. This work is a collaboration with the Schlom group at Cornell University, where Hanjong Paik established the optimal MBE growth parameters for these films, and I performed the magnetic damping characterization. We find that MBE is capable of providing sub-10-nm films with very low values of damping, rivaling or surpassing other deposition techniques. We are able to grow LuIG films down to 2.8 nm, or 4 layers along the interplanar spacing d_{111} (0.71 nm) [21, 26], while retaining

high crystalline quality. We report in- and out-of-plane ferromagnetic resonance measurements as a function of film thickness, demonstrating reduced two-magnon scattering compared to previous work. We achieve effective damping coefficients as low as $11.1(9) \times 10^{-4}$ for 5.3 nm LuIG films and $32(3) \times 10^{-4}$ for 2.8 nm films, which can be compared to the best previous report for very thin YIG, 38×10^{-4} for a 4 nm film.[21]

As an iron garnet, LuIG has ferrimagnetic properties similar to YIG. The magnetic moments in both materials arise from their Fe^{3+} ions, which interact via super-exchange through oxygen atoms [3, 26]. In bulk samples, LuIG has a slightly higher room-temperature saturation magnetization (1815 Oe) than YIG (1760 Oe) [3, 26, 28]. The bulk lattice parameters for LuIG (12.283 Å) and YIG (12.376 Å) differ by 0.75% [29, 30]. Both materials can be grown on isostructural gadolinium gallium garnet ($Gd_3Ga_5O_{12}$, GGG) substrates, which have a cubic lattice parameter of 12.383 Å. The resulting mismatch causes biaxial tensile strain with a maximum value of 0.81% and 0.07% for LuIG and YIG, respectively. High-quality YIG films have been grown previously using off-axis sputter deposition [25, 31–34] and pulsed-laser deposition (PLD) [21, 35–41]. The best reported damping values for thin YIG films grown by PLD to date include 2.3×10^{-4} for a 20 nm film [21], 3.2×10^{-4} for a 10 nm film treated with a post-growth etching procedure [42], and 0.7×10^{-4} for a 20 nm film treated with a post-growth high-temperature anneal [43]. For off-axis sputtering, the best reported values include 6.1×10^{-4} for a 16 nm film [34], 12.4×10^{-4} for a 10.2 nm film [32], and 0.9×10^{-4} for a 22 nm film with a post-growth high-temperature anneal [33]. Previous measurements of films thinner than 10 nm recorded significant two-magnon scattering [21, 32], and much larger damping parameters of 38×10^{-4} for a 4 nm film and 16×10^{-4} for a 7 nm film [21].

3.2 Growth by molecular-beam epitaxy

The MBE technique uses physical evaporation of the constituent elements to grow a stoichiometric film, by tuning the relative rates of evaporation. In the case of iron garnets, we supply Fe and rare-earth elements (Y or Lu) through evaporation, and the oxygen through ozone gas in the growth chamber. Hanjong Paik in the Schlom group developed the procedure for growing iron garnets, by exploring the optimal growth parameters using feedback from the crystal properties. In this section, I present the growth technique that Hanjong used to grow LuIG films of thickness down to 2.8 nm. I discuss growing YIG films by MBE and an outlook on the growth technique for iron garnets in Section 3.4.

The epitaxial growth of iron garnets depends on the substrate, which provides a lattice template to seed the crystal structure. With cubic lattice parameters for YIG and LuIG of 12.376 Å and 12.283 Å respectively, isostructural gadolinium gallium garnet ($Gd_3Ga_5O_{12}$, GGG) substrates with a lattice parameter of 12.383 Å provide a compatible template. The resulting mismatch causes biaxial tensile strain with a maximum value of 0.07% and 0.81% for YIG and LuIG respectively. We prepare GGG substrates by annealing at 1300°C for 3 hours in an air furnace to produce atomically smooth terraces interrupted by atomic steps, which act to seed layer-by-layer growth. Figure 3.1 shows an atomic force microscope image of a GGG substrate after annealing. For (111)-oriented films, each step corresponds to the d_{444} spacing (0.177 nm).

During growth, we simultaneously co-supply Lu and Fe with an accuracy of ±5%, to achieve the stoichiometric atomic ratio of Lu:Fe=3:5. Distilled ozone (O_3), at a background pressure of 1.0×10^{-6} Torr, provides the oxidant. The

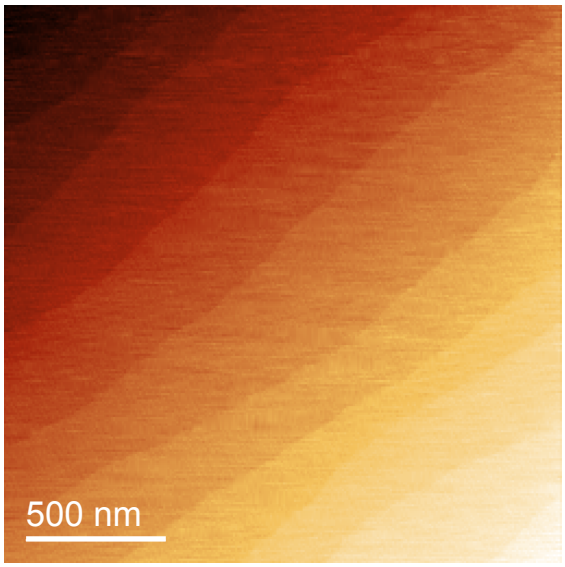

Figure 3.1: Atomic force microscope image of a (111) GGG substrate showing a stepped terrace structure. Published in Ref. [2] supplementary material.

growth temperature is 950 to 970°C, achieved by radiatively heating the backside of the GGG substrate, which is coated with 400 nm of Pt to enhance thermal absorption. This technique can cause slight variations in the growth temperature over the full chip, which I discuss further in Section 3.3.3.

The quality of crystal growth is monitored using *in-situ* reflection high-energy electron diffraction (RHEED). For the (111)-oriented films, we measure RHEED along both the $[1\bar{1}0]$ and $[11\bar{2}]$ in-plane azimuthal directions. The RHEED intensity oscillations (Fig. 3.2(a)) indicate layer-by-layer growth [44], with an oscillation period corresponding to the d_{444} spacing, which is a quarter of a single LuIG layer (d_{111} = 0.71 nm) along the (111)-orientation. We also observe sharp RHEED features and clear Kikuchi lines during growth, as seen in Fig. 3.2(b,c) for a 10 nm film, demonstrating that our films are of high crystalline quality. These features are not observed if the flux drifts more than ±5%, or if the growth temperature is less than 900°C. We do not perform any post-growth

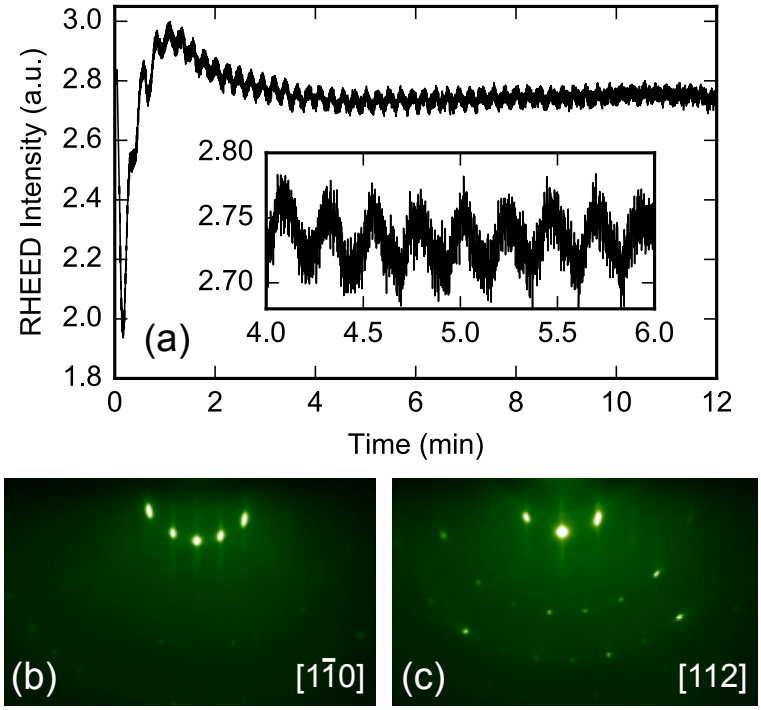

Figure 3.2: (a) RHEED intensity oscillations of a 10 nm thick LuIG film grown on a (111) GGG substrate, indicating layer-by-layer growth. Each oscillation peak-to-peak corresponds a single d_{444} ($d_{111}/4$) spacing. (b,c) Kikuchi lines in the RHEED image taken along both [1$\bar{1}$0] and [11$\bar{2}$] azimuthal directions. Published in Ref. [2].

annealing on our films.

3.2.1 Crystal properties

We quantify the strain state of our films and verify the crystalline quality with four-circle X-ray diffraction (XRD) measurements. The normalized rocking curves for LuIG films with thicknesses 5.3, 10, 20, and 40 nm are shown in Fig. 3.3. All of these samples have full-width at half-maximum (FWHM) values that are less than 0.004°, limited by the GGG substrate. This indicates that

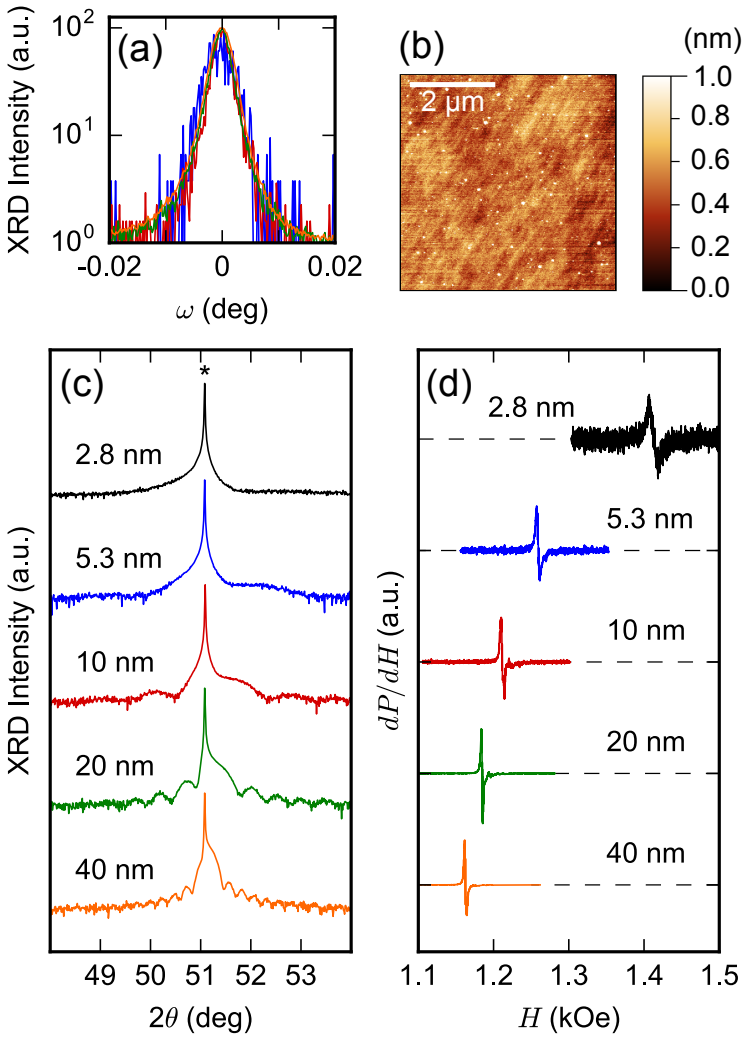

Figure 3.3: (a) X-ray diffraction (XRD) rocking curves for LuIG films of different thickness. (b) Representative atomic force microscopy image of the surface of the 2.8 nm film, showing a RMS roughness of 0.26 nm over 5 μm x 5 μm scan size, which indicates the roughness is substrate limited. (c) $\theta/2\theta$ XRD scans of LuIG thin films grown on (111) GGG substrates as a function of film thickness. The asterisk marks the 444 GGG substrate reflection. (d) Normalized derivative-absorption FMR spectra of the corresponding samples taken at 5 GHz show narrow linewidths that decrease for increasing thickness. The resonance position also depends on the thickness. Published in Ref. [2].

the LuIG films are commensurately strained, and are at the maximal strain state of 0.81% set by the lattice mismatch with the substrate. The rocking curve measurements on a thinner 2.8 nm LuIG film lacks sufficient signal-to-noise for an accurate quantitative analysis, but the results from the thicker films suggest that the strain state is also commensurate for this film. The surfaces of the films are characterized by atomic force microscopy. Figure 3.3(b) shows the 2.8 nm film, with a measured surface roughness of 0.26 nm (RMS) over a 5 μm x 5 μm scan area. This indicates that the surface quality is substrate limited, which we observe for all thicknesses. Figure 3.3(c) shows the $\theta/2\theta$ XRD patterns of the LuIG thin films for all thicknesses grown. The visible Laue oscillations confirm thickness measurements we make with the RHEED intensity oscillations and flux calibrations. Low-angle X-ray reflectively (XRR) determines the film thicknesses as 2.84(1), 5.33(2), 9.94(2), 20.16(3) and 40.37(10) nm, which we nominally report as 2.8, 5.3, 10, 20, and 40 nm.

3.3 Ferromagnetic resonance measurements

The magnetic properties of the MBE-grown LuIG films are characterized by measuring the frequency and thickness dependence of ferromagnetic resonance (FMR), using the system described in Chapter 2. The samples are placed, LuIG-side down, on a broadband coplanar waveguide so that the Oersted field of the waveguide excites FMR at GHz frequencies [12]. We measure the FMR spectra at fixed frequency by sweeping the applied magnetic field, oriented either in-plane (IP) parallel to the coplanar waveguide or out-of-plane (OOP). For the IP measurements, we position the film so that the applied magnetic field is always along the $[11\bar{2}]$ crystal orientation. The measured signal corresponds

to the derivative absorption, which we detect via the voltage from a detector diode. We achieve optimal sensitivity using lock-in amplification by modulating both the input power and the applied field. All of the FMR measurements are performed at room temperature.

3.3.1 Gyromagnetic ratio determination

The analysis of the FMR data requires that determination of the gyromagnetic ratio γ. We establish this parameter by measuring the out-of-plane resonance fields $H_r^{\perp}$ as a function of frequency f. Once the films are fully saturated (for scans above 3 GHz), the resonance fields follow the Kittel equation, for an out-of-plane applied field [45],

$$H_r^{\perp} = \frac{2\pi f}{|\gamma|} + 4\pi M_{\text{eff}}, \tag{3.1}$$

in terms of the effective magnetization M_{eff}. By fitting this equation to the data, we find a gyromagnetic ratio of $|\gamma|/2\pi = 2.77(2)$ MHz/Oe and effective magnetizations of $4\pi M_{\text{eff}} = 1442(10)$ and $1522(10)$ Oe for 20 and 40 nm LuIG films respectively, which can include additional uniaxial anisotropy. The gyromagnetic ratio is consistent with the typical YIG value of 2.8 MHz/Oe [45].

3.3.2 Two-magnon scattering analysis

Figure 3.3(d) shows the IP-FMR response at 5 GHz for LuIG samples with different thicknesses. Two trends are apparent as the film thickness is reduced:

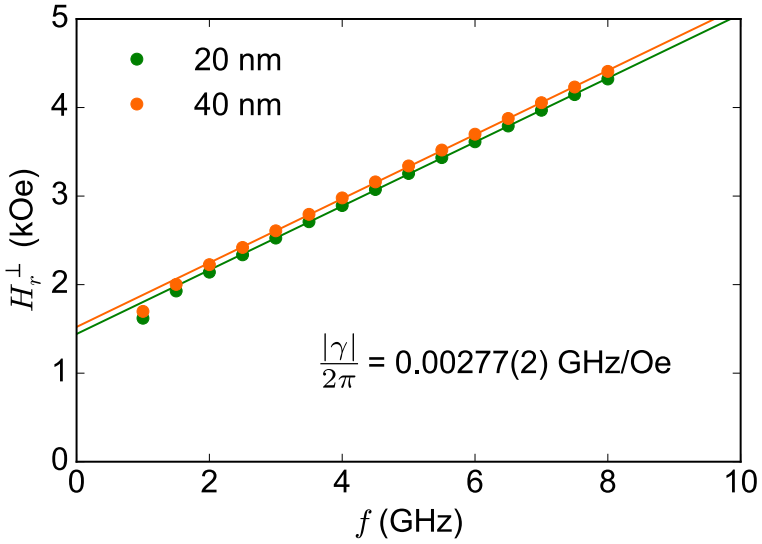

Figure 3.4: The out-of-plane FMR resonance fields for both the (green circles) 20 nm and (orange circles) 40 nm LuIG films, with comparisons to fits to the OOP Kittel equation (solid lines). Published in Ref. [2] supplementary material.

(i) the resonance position shifts to higher fields and (ii) the linewidth increases substantially. Below we show that both of these effects can be explained by two-magnon scattering [46–48]. We focus first on the behavior of the resonance fields. We have measured the IP-FMR resonances for each film thickness at frequencies from 1 to 10 GHz. The evolution as a function of frequency is shown in Fig. 3.5(a) and as a function of thickness in Fig. 3.5(b).

In the presence of two-magnon scattering, the IP resonance field $H_r^\parallel$ predicted by the Kittel equation in the thin-film limit takes the form [46, 49]

$$H_r^\parallel(f,t) = \sqrt{\left(\frac{4\pi M_{\text{eff}}(t)}{2}\right)^2 + \left(\frac{2\pi f}{|\gamma|} + \Delta H_r(t)\right)^2} - \frac{4\pi M_{\text{eff}}(t)}{2}, \tag{3.2}$$

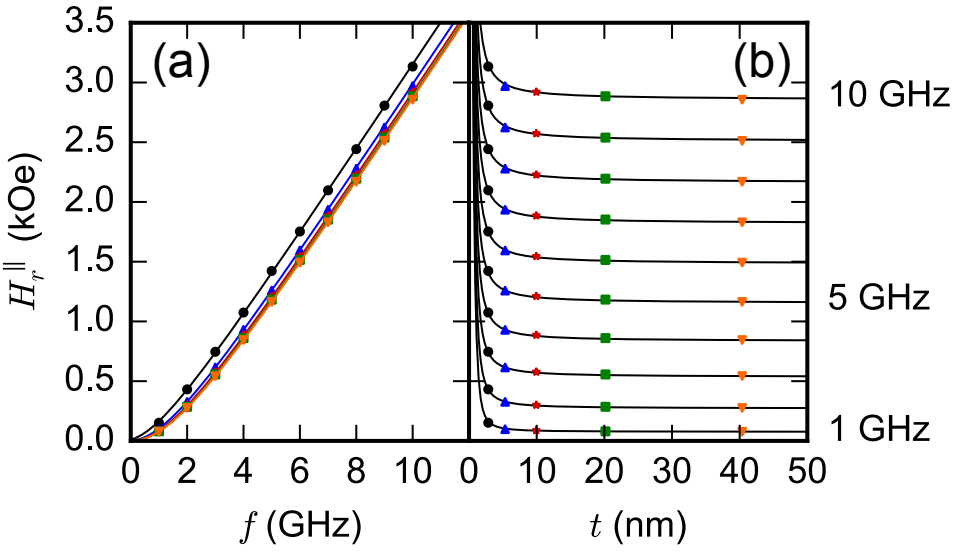

Figure 3.5: (a,b) In-plane FMR resonance fields of each LuIG sample (a) as a function of frequency for different sample thicknesses and (b) as a function of thickness for different frequencies. The solid lines in (a) and (b) represent simultaneous fits to Eq. (3.2) with the 3 fitting parameters r, $4\pi M_s$, and K_s. The symbols correspond to different LuIG thicknesses: black circles = 2.8 nm, blue triangles = 5.3 nm, red stars = 10 nm, green squares = 20 nm, and orange upside-down triangles = 40 nm. Published in Ref. [2].

with f the excitation frequency, t the film thickness, ΔH_r a renormalization shift associated with two-magnon scattering, and γ the gyromagnetic ratio from Section 3.3.1. The effective anisotropy field $4\pi M_{\text{eff}}$ is expected to depend on the film thickness, because it contains contributions from both bulk demagnetization and surface anisotropy:

$$4\pi M_{\text{eff}} = 4\pi M_s + \frac{2K_s}{M_s t}. \tag{3.3}$$

Here M_s is the saturation magnetization and K_s is the surface anisotropy energy. The renormalization shift produced by two-magnon scattering can be related to

the surface anisotropy as [46, 49]

$$\Delta H_r(t) = r\left(\frac{2K_s}{M_s t}\right)^2, \tag{3.4}$$

where r is a parameter characterizing the strength of two-magnon scattering.

We performed a global least-squares fit of Eqs. (3.2)-(3.4) to all the data in Fig. 3.5 using three fitting parameters r, $4\pi M_s$, and K_s. As shown by the lines in Fig. 3.5, we find excellent fits assuming that all three parameters are independent of film thickness, obtaining the values $r = 4.9(2)\times10^{-4}$ Oe^{-1}, $4\pi M_s = 1609(1)$ Oe, and $K_s = -8.52(8) \times 10^{-3}$ erg/cm^2. We also attempted to fit the data without the two-magnon contribution (i.e., with the constraint $r = 0$ Oe^{-1}), but we found significant discrepancies for the 2.8 film, especially at low frequencies. The non-zero value of r implies that the two-magnon mechanism is active. For our 2.8 nm film, the renormalization shift is $\Delta H_r = 110$ Oe, similar to that found in a 2.7 nm NiFe film [49]. The value of $4\pi M_s$ determined by the fit is significantly lower than the bulk LuIG value of 1815 Oe [28]. This reduction is qualitatively consistent with the tensile strain in our films from the GGG substrate. The tensile strain is expected to enhance the antiferromagnetic super-exchange interaction between the two inequivalent Fe^{3+} lattices in the LuIG and therefore reduces the overall saturation magnetization [3, 26]. Another contribution to the small value of M_s could come from tetrahedral Fe^{3+} vacancies, particularly at the film surface [36, 50]. By reducing the M_s value these can also increase the surface anisotropy field ($2K_s/M_s t$), and therefore increase the damping through two-magnon scattering. The negative sign that we find for K_s indicates that the surface anisotropy reduces the effective demagnetization field $4\pi M_{\text{eff}}$ compared to the bulk value. The magnitude of K_s is relatively weak, however (e.g.,

more than two orders of magnitude smaller than K_s for annealed CoFeB [51], but close to the value predicted for (111)-oriented YIG [50], $K_s = -5.2 \times 10^{-3}$ erg/cm^2). With our values for $4\pi M_s$ and K_s, only for extremely thin LuIG films, < 0.8 nm, might the magnetic anisotropy be turned perpendicular to the sample plane. For any thickness above this, $4\pi M_{\text{eff}}$ favors in-plane magnetization.

3.3.3 Multi-resonance model and inhomogeneity

Next we consider the FWHM linewidths (ΔH) of the IP FMR resonances for our LuIG films as a function of thickness and FMR frequency. The linewidths of our samples are sufficiently narrow that small inhomogeneities in the films can result in overlapping but distinguishable resonances, as has often been seen previously in measurements on thin garnet films [21, 38, 52]. To make an accurate determination of the intrinsic linewidths, we fit each measured curve to the sum of multiple (2 in this analysis) Lorentzian derivative curves with their widths constrained to be identical. This procedure produces values for the linewidth that are consistent with the results for films that can be cleaved into samples sufficiently small to isolate a single resonance.

Figure 3.6 shows the FMR spectra of the 40 nm film at 1 and 10 GHz. While the low-frequency scan can be fit reasonably well to a single Lorentzian derivative, at 10 GHz the resonance shape is clearly more complex. We show in Fig. 3.6(b), that a simple sum of two Lorentzian derivatives can account well for the 10 GHz data, by allowing the two amplitudes to vary but assuming that the linewidths are the same for both.

We interpret the observation of multiple resonances as due to the presence

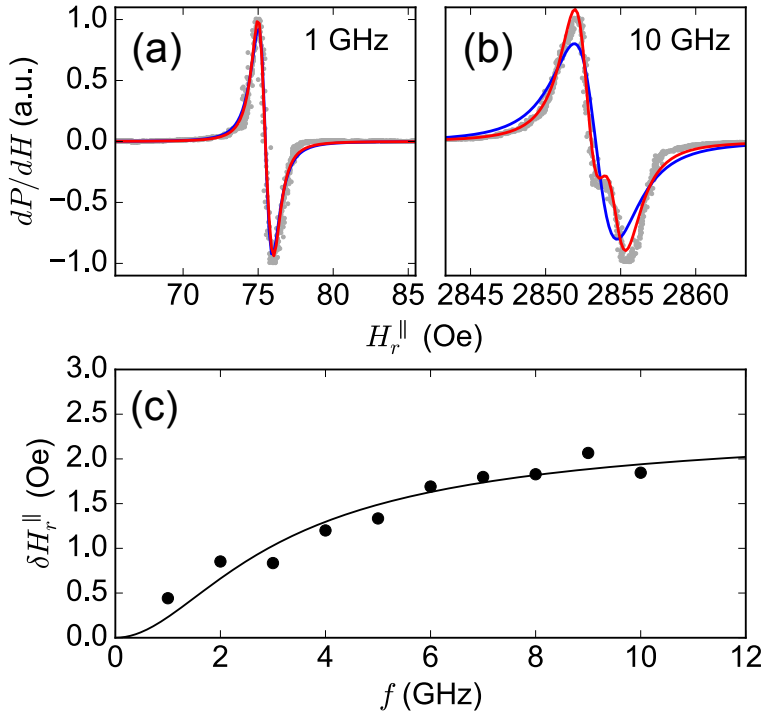

Figure 3.6: FMR spectra (grey) for a 40 nm LuIG film at (a) 1 and (b) 10 GHz, with fits (blue) to a single Lorentzian derivative and (red) to the sum of two Lorentzian derivatives. At low frequency, the differences between the models are not significant, but at higher frequencies the single-Lorentizan model over-estimates the linewidth and does not capture the features in the resonance. (c) The difference between the resonance positions of the two Lorentzian derivatives extracted from fits. The line is the frequency difference expected from the Kittel equation if the effective magnetizations differ by 0.3%. Published in Ref. [2] supplementary material.

of spatially separate regions of the LuIG film with slight different values of M_{eff}. Consider two regions of the sample with effective magnetization $M_{\text{eff}}^{(1)}$ and $M_{\text{eff}}^{(2)}$, which differ due to either slight variations in stoichiometry or surface anisotropy. The difference in the resonance fields $\delta H_r^{\parallel} = H_r^{\parallel}(M_{\text{eff}}^{(2)}, f) - H_r^{\parallel}(M_{\text{eff}}^{(1)}, f)$ determines the degree to which the Lorentzian-derivative lineshapes of each region will overlap. Figure 3.6(c), shows that $\delta H_r^{\parallel}$ from the two-resonance fits for the 40 nm film at different values of the FMR frequency agree well with the

frequency dependence expected from the Kittel equation. Because of the very narrow resonances of LuIG, even very small differences in M_{eff} can produce visible splitting in the resonance; from the fit in Fig. 3.6(c) for the 40 nm film the two values of M_{eff} differ by only 0.3%. The ratio of the amplitudes of the two resonances is essentially constant, at 0.72(6), across frequency. This behavior is consistent with expectations for separate contributions from two regions of the film that have fixed volumes. We observed qualitatively similar behaviors for all of our film thicknesses from 2.8 to 40 nm film.

We also find that by dicing a sample into smaller millimeter pieces it is possible to approach the isolation of a single resonance. Figure 3.7 shows the effect of dicing the center 4×4 mm^2 section of the original 10×10 mm^2 sample. This removes edge sections that may have experienced minor thermal gradients during the growth process, and subsequently have slightly different M_{eff}. We find that the linewidths of the near-single resonances agree with the values extracted from fitting the resonances of the larger-area samples to two Lorentzian derivatives. However, by limiting the volume being excited into precession, dicing a sample reduces the overall signal-to-noise significantly. Therefore the dicing procedure is not practical for the measurement of the thinnest films.

3.3.4 Damping characterization

Figure 3.8(a) shows the measured frequency dependence of the linewidth for each of our films. We observe a linear dependence on frequency up to roughly 8 GHz. At higher frequencies, the linewidths deviate from linearity, most obviously for the 2.8 and 5.3 nm films. This high-frequency curvature is qualitatively

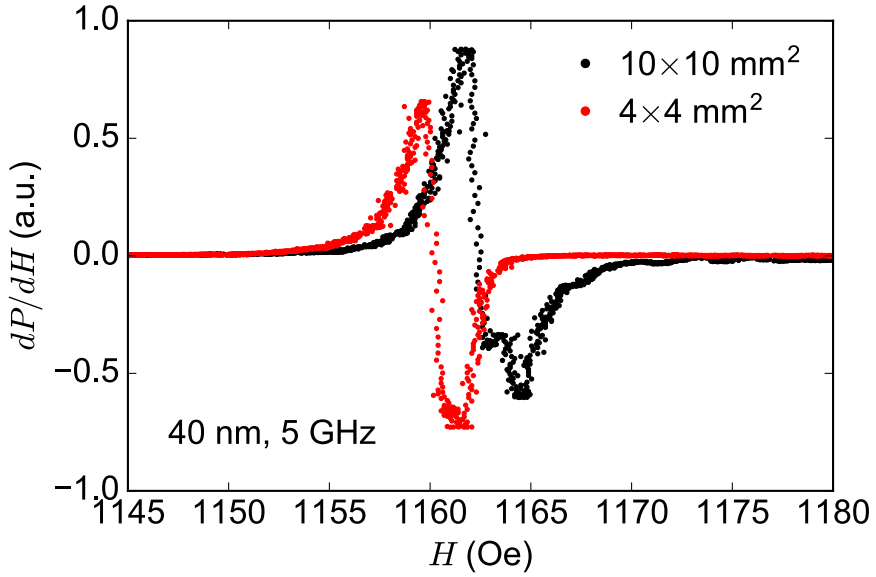

Figure 3.7: Normalized FMR spectra for a 40 nm LuIG film (black circles) before dicing the original 10×10 mm^2 sample, and (red circles) after dicing the center 4×4 mm^2 section. The noticeable shift in resonance field is a combination of minor in-plane misalignment and the reduction of lower M_{eff} regions at the sample edges. Published in Ref. [2].

consistent with the effect of two-magnon scattering, as observed previously in PLD-grown YIG films [21]. Using the expression [12]

$$\Delta H(f) = \frac{4\pi\alpha f}{|\gamma|} + \Delta H_0, \tag{3.5}$$

we can define an effective Gilbert damping parameter, α, for each value of film thickness based on linear fits to the data below 8 GHz (Fig. 3.8(b)). The zero-field linewidth ΔH_0 represents the extrinsic contributions to the linewidth in this model, and increases in proportion to the two-magnon scattering strength [47]. The line shown in Fig. 3.8(b) is a fit to a phenomenological form

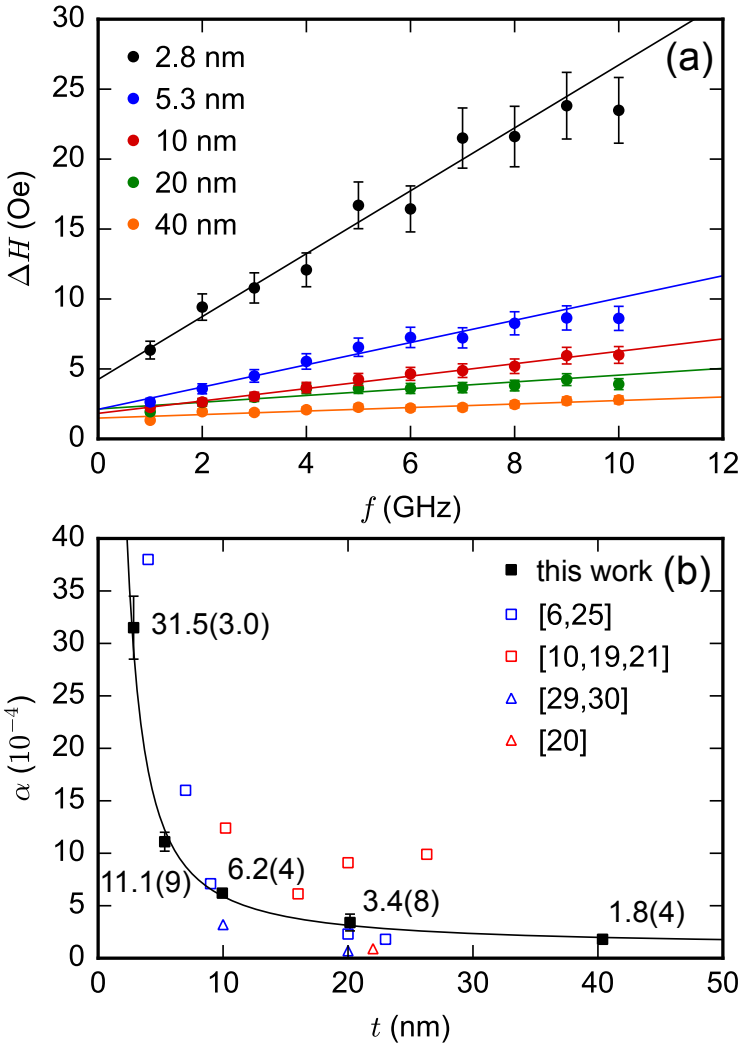

Figure 3.8: (a) Frequency dependence of the FMR linewidth, for LuIG films of different thickness. The linewidths are fit to straight lines up to 8 GHz, after which the linewidths start to roll off, following the signature of two-magnon scattering. (b) Thickness dependence our measured values of magnetic damping (black squares). The line depicts the phenomenological form of Eq. (3.6). Previously-reported results for damping in thin YIG films are shown for films deposited by PLD (open blue symbols) PLD and off-axis sputtering (open red symbols). Open triangles represent post-processed films. Published in Ref. [2].

$$\alpha = \alpha_G + \alpha_{2M}\left(\frac{A}{t^2} + \frac{B}{t}\right), \tag{3.6}$$

with $\alpha_G = 0.9(6) \times 10^{-4}$, $A\alpha_{2M} = 125(45) \times 10^{-4}$ nm^2, and $B\alpha_{2M} = 36(11) \times 10^{-4}$ nm.

3.4 Discussion

Our results demonstrate that molecular-beam epitaxy is a viable method for growing iron garnets. In this section, I discuss some of the remaining challenges in the use of this technique. Specifically I address the inhomogeneity issues and the weak value of M_s. I end with an outlook on using MBE to grow other types of rare-earth iron garnets.

As we show in Section 3.3.3, the complex FMR spectra that we measure for our LuIG films can be understood as slight variations in the effective magnetization. From our experiments dicing the samples, the variation appear to be on the millimeter length scale. However, we also found that the edges were most prone to these inhomogeneity issues. This greatly limits the viable area for fabricating devices, since the samples are already only 10×10 mm^2 in area. Therefore, it is advantageous to optimize future MBE growth to eliminate the variation. The most promising area of improvement is the thermal heating system, since in our film growth the sample had different thermal conductivities surrounding it. Mounted in a metal puck, the sample edges have the highest ability to dissipate heat compared to the sample center. Its not clear at this point how significant a variation is needed to cause noticeable effects in the FMR, so the first step is to quantify the spacial temperature dependence during growth. Future experiments growing LuIG using larger GGG substrates also examine

this hypothesis. Overall, demonstrating single-resonance FMR spectra is an important next step in using MBE for iron garnet growth.

The weak value of M_s that we determine from the two-magnon scattering analysis in Section 3.3.2, may indicate the presence of vacancies or Fe^{3+} substitutions at the film surface. This behavior has been investigated theoretically with a single-ion model, that predicts the surface anisotropy in (111)-oriented YIG that is in reasonable agreement with our LuIG analysis [50]. Since M_s has been show to be reduced by tetrahedral Fe^{3+} vacancies in YIG [36], this suggests that the surface anisotropy field, $\frac{2K_s}{M_s t}$, increases by this effect. The damping contribution from two-magnon scattering scales with this surface anisotropy field, so a decrease in M_s is expected to increase the damping. This provides an opportunity for future improvements. In the film, Fe^{3+} vacancies are always accompanied by O^{2-} vacancies that compensate the charge. By reducing the number of O^{2-} vacancies during growth, the damping may decrease even further for the thinnest films where two-magnon scattering dominates. Future experiments growing in a higher ozone pressure may achieve this reduction in O^{2-} vacancies to produce iron garnets with very low damping even at thicknesses of a few nanometers.

The growth of high-quality LuIG films by MBE suggests that other iron garnets may be grown by this technique. Hanjong Paik has demonstrated the growth of YIG films with comparable damping values, although these results remain unpublished at this time. Besides LuIG and YIG, there are a number of iron garnets with more exotic properties [26], such as a compensation point in temperature where the sub-lattice moments in the ferrimagnet momentarily form an anti-ferromagnet ($4\pi M_s = 0$ Oe). Consider the material holmium iron garnet ($Ho_3Fe_5O_{12}$, HoIG), which has a compensation temperature between 130

and 140 K [53]. By growing a YIG/HoIG/Pt structure, a future project could investigate the spin-pumping signal as a function of temperature to compare the results to the YIG/NiO/Pt measurements that demonstrated spin-transport through the anti-ferromagnetic layer NiO [54]. The ability to tune the saturation magnetization M_s also allows for thermally actuated changes in spintronic properties; such as spin-transfer torque (with a critical-current scaling proportional to M_s), spin-pumping (scaling inversely proportional to M_s), and the thermal energy barrier (proportional to M_s). The successful growth of these iron garnet materials in thicknesses less than 20 nm can enable a number of interesting experiments that yield new insight into spintronic physics.

3.5 Conclusion

The damping values of our LuIG films are among the best reported for any garnet film, and extend the viable thickness of low-damping thin films well below 10 nm. We measure $\alpha = 11.1(9) \times 10^{-4}$ for 5.3 nm LuIG films and $32(3) \times 10^{-4}$ for 2.8 nm films. We speculate that our MBE growth procedure minimizes the amount of surface roughness and other defects even for very thin LuIG films, compared to other deposition techniques, and thereby provides a reduced level of two-magnon scattering. Similar MBE growth procedures may also allow the production of sub-10-nm films made from YIG and other garnets, assisting in the development of a wide variety of spintronic devices incorporating these materials. Future experiments that optimize the growth temperature uniformity and Fe^{3+} vacancies provide additional ways to improve the film homogeneity and further reduce the damping for these ultra-thin films.

CHAPTER 4

LOW-TEMPERATURE DAMPING ENHANCEMENT IN YIG

4.1 Introduction

Yttrium iron garnet ($Y_3Fe_5O_{12}$, YIG) thin films are of considerable interest for applications in spintronics and magnonics, since YIG can have one of the lowest damping coefficients of any magnetic material at room temperature [11]. High-quality films of YIG and related garnets with thicknesses on the 10's of nm scale and below can be grown by pulsed-laser deposition (PLD) [21, 35–41], off-axis sputtering [25, 31–34], and molecular-beam epitaxy (MBE)[2] (see Chapter 3). Ferromagnetic resonance (FMR) measurements at room temperature for films grown by all of these techniques show that the FMR linewidth increases with decreasing film thickness, and the frequency dependence of the linewidth has a nonlinear functional form for very thin films [2, 21, 55]. This behavior has been attributed to two-magnon scattering at the film interfaces that becomes increasingly dominant as the film thickness decreases [46, 47].

We are interested in extending the use of ultra-thin YIG films to cryogenic temperatures, for example so that we can use scannning SQUID microscopy [56] to study the manipulation of YIG devices by spin-orbit torques [1, 20], as I discuss in Chapter 5. In the course of this work we have found that even apparently high-quality YIG films, which possess small FMR linewidths at room temperature, can have linewidths that increase dramatically with decreasing temperature. The 15 nm YIG film featured in this chapter has a linewidth that increases by a factor of 28 as the temperature is lowered from room temperature to 25 K. The linewidth of this thin YIG film also shows an increasingly nonlin-

ear frequency dependence as the temperature is lowered. We argue that these strong temperature dependencies cannot be explained by two-magnon scattering from the YIG interfaces. Instead, we suggest that the increased linewidth at low temperature is due to magnetic damping associated with impurity mechanisms that have been studied previously in bulk YIG samples [11, 57–59].

I start this chapter with an overview of the cryogneic measurement system that I built in collaboration with members of the Ralph and Buhrman groups, to extend the FMR system that I describe in Chapter 2. From there, I discuss the material growth of YIG films in collaboration with the Yang group at Ohio State University. All of the characterization measurements focus on a single YIG film of 15 nm, which gives a comprehensive view of the material. These measurements provide a basis for the interpretation of the spin-torque experiments in Chapter 5, and the results serve as an important caveat to low-temperature magnetic applications.

4.2 Cryogenic apparatus for ferromagnetic resonance

In this section, I describe the cryogenic apparatus for ferromagnetic resonance (FMR) that I built in collaboration with Neal Reynolds, Shengjie Shi, and Graham Rowlands. The system extends the room-temperature FMR setup that I built, described in Chapter 2, by introducing a modified waveguide and a cryogenic dipper for mounting the waveguide into the existing system. We use the same measurement electronics and automation software to perform measurements in the cryostat. The only electronics addition is the LakeShore 331 Temperature Controller, that regulates the heater elements on the Janis Supertran-

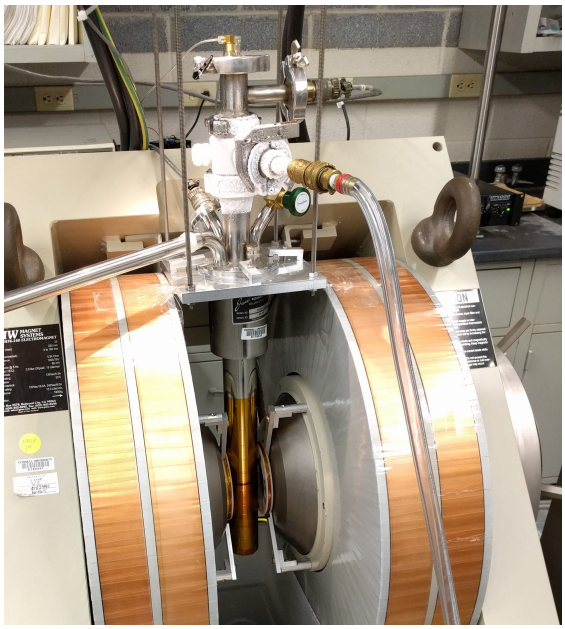

Figure 4.1: Photograph of the cryogenic apparatus mounted in the GMW 3474 electromagnet between the Helmholtz coils (see Chapter 2 for details).

VP cryostat. With a liquid He dewar, this continuous-flow system provides stable temperatures from room temperature down to 4 K. Overall, the system allows the broadband detection of FMR and provides insight into the dependence of the resonance on temperature.

4.2.1 Modified waveguide and RF circuit

I adapted the waveguide from Section 2.2.3 to fit the confined geometry in the cryostat, keeping other dimensions and specifications constant. Figure 4.2 shows the schematic of the waveguide design. A surface mount version of the micro-miniature (SMPM) connectors (TE Connectivity 1757639-1) replaces the SMA connectors in the original design. These new connectors have a considerably smaller footprint on the board (see Detail A in Fig. 4.2), and have a sim-

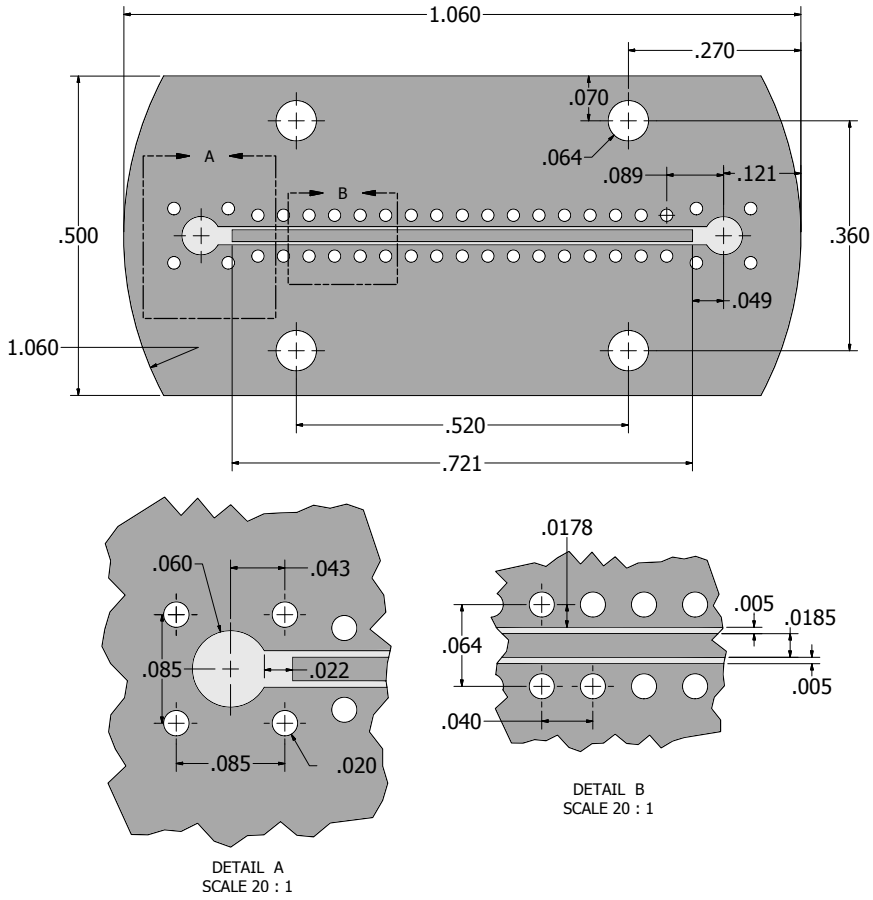

Figure 4.2: Schematic of the FMR waveguide for use in the low-temperature cryostat. All dimensions are in inches.

pler push-connector attachment system. We use solder paste (MG Chemicals 4900P-25G) to solder the SMPM connectors onto the boards. Additional waveguides are made for other RF measurements (such as spin-torque FMR), which are adaptations of this design with a center region cut out. These boards allow wire bonding from the RF lines to a sample, and are compatible with the cryogenic dipper. All of the boards were purchased from PCB Universe (Vancouver, Washington).

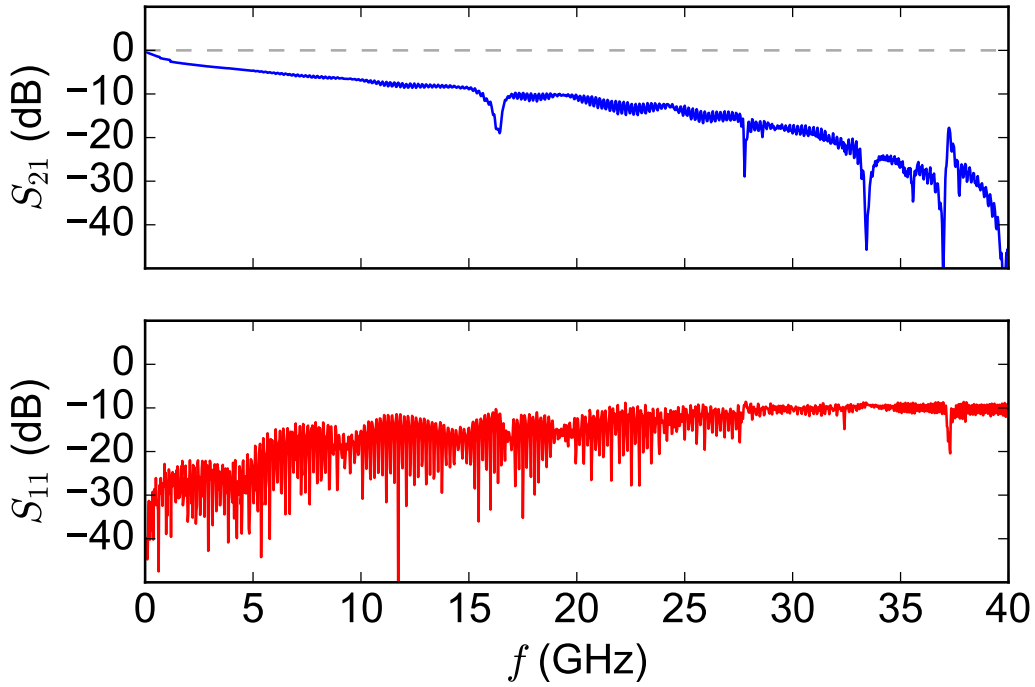

Figure 4.3: Scattering parameters of the full RF circuit of the cryostat at room temperature, including the coplanar waveguide, the transmission lines, and the bulkhead connectors, showing the (solid blue) transmission (S_{21}) and (solid red) reflection (S_{11}).

Adapters (Pasternack PE91301) from SMPM to SMA join the connectors on the waveguide to the RF cables (Pasternack PE34735LF-21 with RG405 Coax), which have 2.92 mm connectors. While compatible with SMA, the 2.92 mm connectors have bandwidth up to 40 GHz, nearly twice typical SMA specifications. The adapters to SMPM are SMA instead of 2.92 mm since the cost is 4 times greater for these parts specifically. The 2.92 mm cables connect through a KF flange by hermetically sealed 2.92 mm bulkhead connectors (Pasternack PE9647). From there, the RF circuit matches the room temperature system, described in Chapter 2.

I measure the frequency-dependent transmission of the full RF circuit of the cryostat at room temperature, including the coplanar waveguide, the trans-

mission lines, and the bulkhead connectors, using a vector network analyzer (VNA). Figure 4.3 shows the transmission (S_{21}) and reflection (S_{11}) scattering parameters as a function of frequency (f). The full circuit has less than 10 dB losses below 15 GHz. Compared to the orignal waveguide (Fig. 2.7), there are higher losses in this system. A large part of those losses is in the long cables that run down the cryogenic dipper, and the numerous connectors/adapters in the path. At lower temperatures, transmission slightly improves; for 33 K, 10 dB losses occur above 20 GHz. This effect is not significant enough to influence the measurements present in this chapter. Overall, the transmission through the RF circuit and waveguide is sufficient for generating the excitation field in FMR and detecting the power absorption.

4.2.2 Cryogenic dipper

The cryogenic dipper provides the structural support for the waveguide and the RF circuit to mount into the Janis cryostat. At the top, a brass KF flange houses the two 2.92 mm bulkhead connectors and connects to two threaded 1/4"-20 stainless steel rods. These rods hang below the flange and support the baffles and the base mount, to which the waveguide attaches. The baffles are made of 1.060" O.D. disks of Delrin. They have holes for the stainless steel rods, and slots for the RF cables to add rigidity to the system. Each baffle mounts onto the rods with 1/4"-20 nuts at each side. The nuts are low-profile to ensure they do not stick out beyond the 1.060" O.D. of the dipper.

The waveguide attaches to the base mount, which sits at the bottom of the stainless steel rods. The thermometer has a placement hole in the base mount,

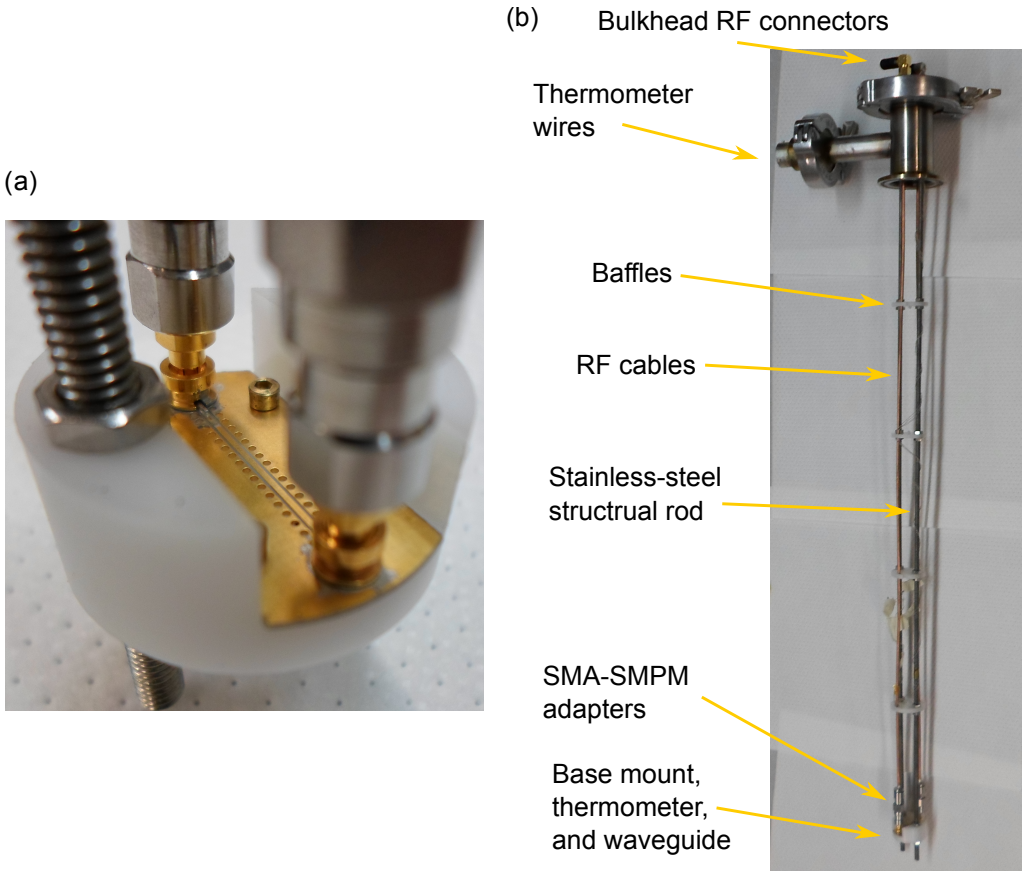

Figure 4.4: Photographs of (a) a close up view of the base and waveguide, and (b) the cryogenic dipper with the relevant parts marked.

which allows it to make thermal contact to the copper waveguide. This ensures that the thermometer accurately measures the waveguide temperature, which should closely reflect the actual sample temperature after stabilization. I use Ducco cement to attach the sample to the waveguide, by placing cement on the four corners of the sample, with the sample film-side down. This adhesive can be easily removed with Acetone/IPA, but ensures that the sample remains rigidly attached at low-temperatures. In converse, I found that Kapton tape did not stay fixed through a full thermal cycle.

4.3 Growth by off-axis sputtering

In collaboration with the Yang group at Ohio State University, we grow our YIG films using off-axis sputter deposition on (111)-oriented GGG substrates in a chamber with a base pressure of 5×10^{-9} Torr, with an Ar/O_2 pressure of 11.5 mTorr and an O_2 concentration of 1% [25, 31, 34]. We prepare our epi-ready GGG substrates with solvent cleaning followed by ultra-violet and oxygen (UVO) cleaning for 2 min, which oxidizes the substrate surface with ozone to remove organic contaminants. During YIG deposition, we heat the substrate to 750°C and rotate at 10 deg/sec. We use a 60 W radio-frequency power, which results in a deposition rate of 0.26 nm/min. We use a 15.4 nm film for the YIG characterization in this study. This thickness is representative of the YIG films that we use in the switching experiments of Chapter 5, so the results provide important insight into the magnetic parameters. We determine the thickness by measuring the X-ray reflectivity, as shown in Fig. 4.5, and fitting the intensity oscillations using the Rigaku GXRR3 software to extract the YIG thickness.

4.4 Magnetic characterization

Before examining the ferromagnetic resonance, in this section I present saturation magnetization and substrate susceptibility measurements. Establishing the saturation magnetization is necessary for the analysis we perform on two-magnon scattering and impurity relaxation mechanisms. Examining the substrate susceptibility also provides the evidence to later eliminate this as an important contributor to the FMR results.

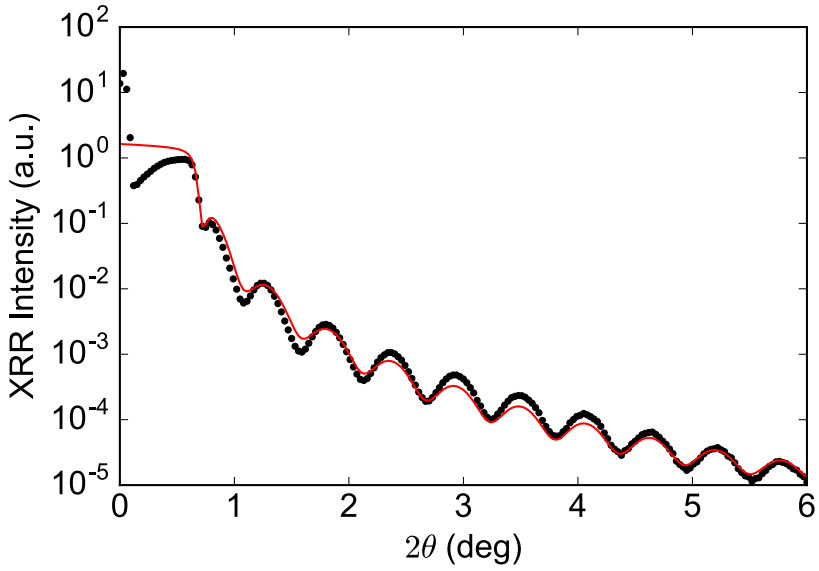

Figure 4.5: (black circles) X-ray reflectivity measurements of the YIG sample on GGG. The fit (red line) yields a YIG thickness of 15.40(3) nm and roughness of 0.10(6) nm at a density of 5.11 g/cc.

We characterize the saturation magnetization through vibrating sample magnetometry (VSM), shown in Fig. 4.6. The paramagnetic Gd ions in GGG produce a background slope in the VSM measurements as a function of in-plane applied magnetic field (inset, Fig. 4.6(b)), that grows strongly with decreasing temperature [60, 61]. To determine the saturation magnetization M_s of the YIG film we fit the sloped background to straight lines above and below the hysteretic switching region, and measure the difference between these lines associated with the reversal of the YIG magnetization. These measurements confirm that the YIG magnetization increases monotonically with decreasing temperature, by approximately 35% between room temperature and cryogenic temperatures, consistent with the expected behavior for ferrimagnetic YIG [3].

A molecular-field model successfully describes the temperature dependence of the saturation magnetization for YIG [3], by considering the combined effect

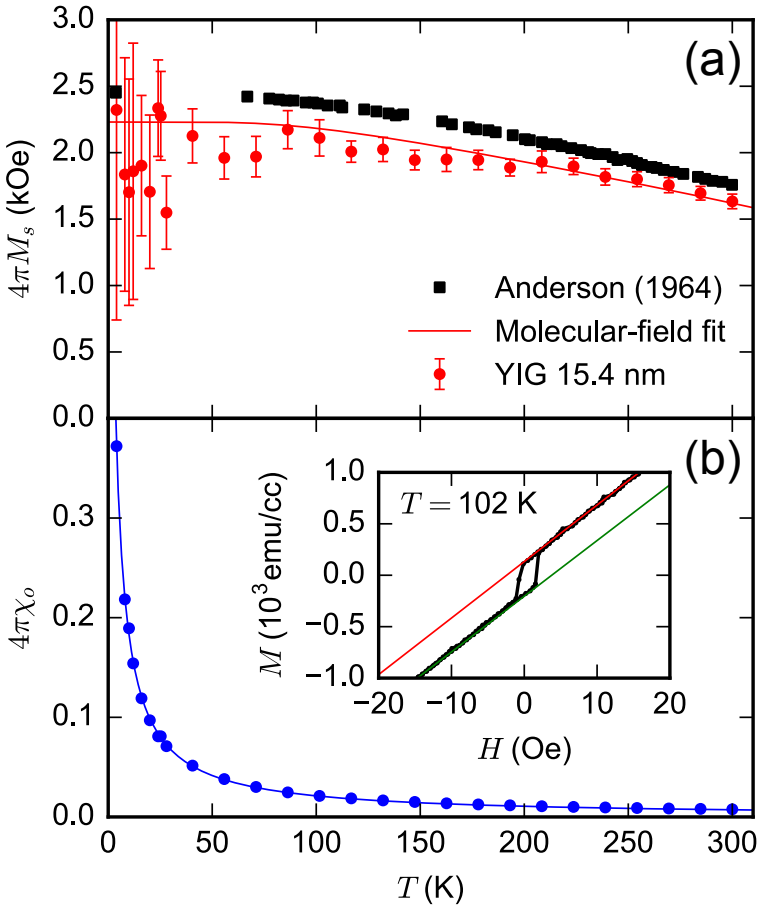

Figure 4.6: (a) Temperature dependence of the saturation magnetization of the YIG film, comparing (red circles) our measured values to (red line) a fit to molecular-field theory and (black squares) previous literature values [3]. (b) (blue circles) Magnetic susceptibility of the GGG substrate, from the linear background slope of the VSM measurements as a function of applied magnetic field. The blue line is a fit to the Curie-Weiss law. (inset) A representative VSM measurement of $M(H,T)$ of a YIG film on GGG at 102 K. The red and green lines are linear fits to the background above and below the switching points of the YIG film.

of the two Fe sub-lattices, which we will refer to as the a and d sites. The total saturation magnetization $M_s(T)$ is the sum of the site-dependent magnetizations, $M_s^{(a,d)} = \rho\sigma_{a,d}$, which are expressed in terms of the magnetization per unit mass $\sigma_{a,d}$ and the YIG density $\rho = 5.11$ g/cc. The site-dependent magnetizations per unit mass are coupled in the form,

$$\sigma_a = \sigma_{a0} B_{5/2}\left((\lambda_{ad}\sigma_d - \lambda_{aa}\sigma_a) \cdot \frac{3.359 \times 10^{-4}}{T}\right) \tag{4.1}$$

and

$$\sigma_d = \sigma_{d0} B_{5/2}\left((\lambda_{ad}\sigma_a - \lambda_{dd}\sigma_d) \cdot \frac{3.359 \times 10^{-4}}{T}\right), \tag{4.2}$$

in terms of the temperature T, the Brillouin function $B_{5/2}$, and the zero-temperature magnetization per unit mass $\sigma_{a0,d0}$. The molecular-field coefficients λ_{ij} quantify the coupling between the sub-lattices, with $\lambda_{ad} = \lambda_{da}$.

We solve Eq. 4.1 and 4.2 simultaneously to generate a theoretical model for $M_s(T)$. Using the values from Anderson [3] as initial parameters, we fit the VSM data in Fig. 4.6(a) with this $M_s(T)$ model. Table 4.1 provides the best fit parameters. We extract values for $4\pi M_s$ of 1630 Oe at room temperature and 2200 Oe when extrapolated to 0 K.

4.4.1 Substrate susceptibility

From the magnitude of the background slope in the VSM measurements, (inset, Fig. 4.6(b)), we can also determine the magnetic susceptibility χ_0 of the

Table 4.1: Molecular-field coefficients for YIG

	σ_{a0} (emu/g)	σ_{d0} (emu/g)	λ_{aa} (cm^{-1})	λ_{dd} (cm^{-1})	λ_{ad} (cm^{-1})
Jermain *et al.*	77.14	111.48	47,820	70,717	22,394
Anderson[3]	75.70	113.55	47,820	71,505	22,394

GGG substrate (Fig. 4.6(b)). The strong temperature dependence we observe for χ_0 corresponds to a Curie-Weiss law, $\chi_0 = C/(T - T_c)$, with a Curie constant $C = 624(5)$ emu/(cm^3 Oe), and a Curie temperature $T_c = -1.8(1)$ K, consistent with previous reports [60, 61]. The relatively large error bars at the lowest temperatures in our determination of M_s (Fig. 4.6(a)) are a consequence of the very large background slope for the VSM signal in this regime. We will revisit the susceptibility of the GGG substrate in the context of the FMR results to show that this behavior can not explain our observations.

4.5 Ferromagnetic resonance measurements

4.5.1 Broadband results

Using our cryogenic FMR system (described in Section 4.2), we measure the broadband response of the YIG sample. Figure 4.7(a) and (b) show room temperature FMR results at 3 and 13 GHz respectively, for a 15 nm film as deposited (*i.e.*, without post-annealing). The resonances correspond well to derivatives of individual Lorentzians, to which we fit to extract the linewidth and resonance field. In Fig. 4.7(c) we plot the Lorentzian full-width at half maximum (FWHM)

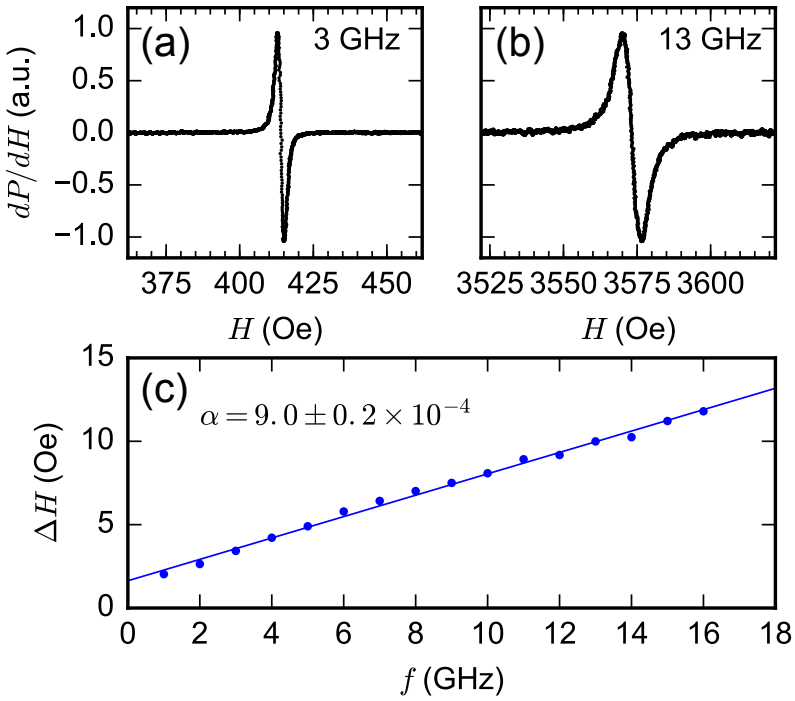

Figure 4.7: Normalized ferromagnetic resonance spectra at (a) 3 GHz and (b) 13 GHz for a 15 nm YIG film at room temperature, with an in-plane applied magnetic field. (c) The frequency dependence of the linewidth corresponds to an effective Gilbert damping constant α = (9.0 ± 0.2) $\times 10^{-4}$.

linewidth ΔH versus frequency. The slope of this curve corresponds to an effective Gilbert damping parameter α = (9.0 ± 0.2) $\times 10^{-4}$. This agrees well with previous measurements of a 14.0 nm YIG film grown by off-axis sputtering [32], which had a damping parameter α = (11.6 ± 0.7) $\times 10^{-4}$, and is within the range of measurements on PLD films of similar thickness [21].

Figure 4.8 shows how the in-plane FMR spectra of the same YIG film vary as a function of temperature. With decreasing temperature the data show a very large increase in the linewidth ΔH, a shift in the resonance field, and a reduction in the amplitude of the signal, visible in the normalized curves as a reduction of the signal-to-noise ratio. The reduction in signal amplitude is

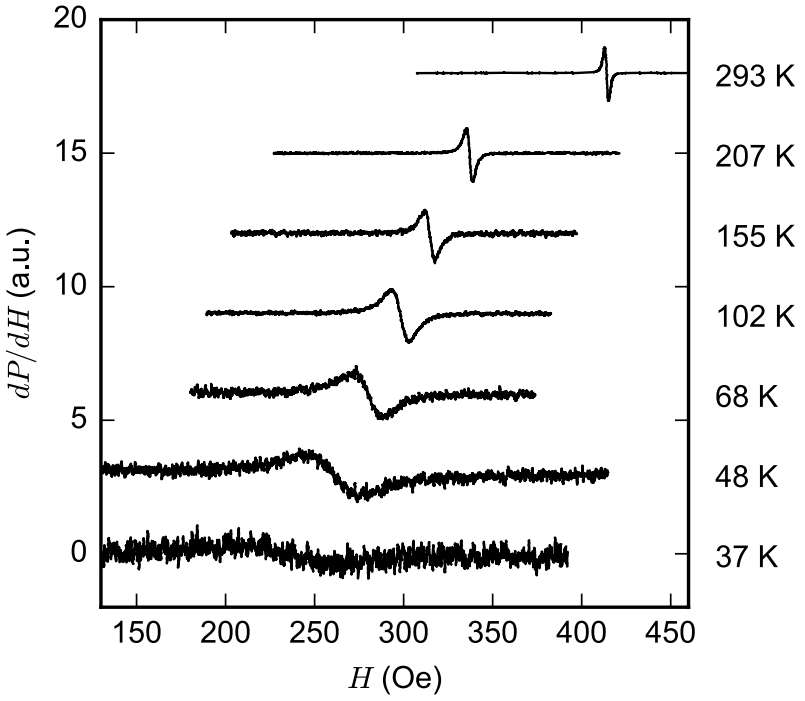

Figure 4.8: Normalized ferromagnetic resonance spectra at 3 GHz with an in-plane applied magnetic field for the YIG film at different temperatures. Different normalization factors are used for data at different temperatures; the actual amplitude of the resonances decreases strongly with decreasing temperature, as reflected in the decreasing signal-to-noise ratio. With decreasing temperature, we observe a large increase in the resonance linewidth.

consistent with the linewidth increase, given that the amplitude is expected [45] to scale with $(\Delta H)^{-2}$. Below roughly 37 K, the resonances become so broad that they are no longer distinguishable using the coplanar waveguide system. This strong temperature dependence is similar to results reported by Shigematsu *et al.* [62], but it is not universal in ultra-thin YIG films: *e.g.,* Haidar *et al.* have observed in YIG films grown by PLD a damping coefficient that decreased by approximately a factor of two upon decreasing T from room temperature to 8 K [55].

By analyzing similar FMR resonances obtained at different values of microwave frequency, we can extract both the frequency and temperature dependencies of ΔH (Fig. 4.9). The frequency dependence at room temperature has an approximately linear dependence, similar to previous studies of high-quality YIG thin films in this thickness range [21, 25, 42]. As a function of decreasing temperature not only does the overall magnitude of the linewidth grow by a large factor, but at the same time there are strong deviations from linearity in the frequency dependence. These nonlinearities are qualitatively similar to what one might expect from two-magnon scattering from defects at the interfaces of the YIG film, but as we will argue below this mechanism cannot explain the very strong variations with temperature. We will instead argue that these changes can be accounted for by impurity relaxation within the YIG film.

4.5.2 Fixed-frequency results

We can obtain greater sensitivity in the FMR experiments, and thereby extend our study to temperatures lower than 37 K, by performing measurements in an X-band cavity. This comes at the cost of operating at fixed frequency (9.4 GHz). We perform measurements in a Bruker Elexsys 500 system designed for electron-spin resonance (ESR) spectroscopy. We mount the sample in the cavity using Teflon tape and a glass rod, and fill the cavity with He exchange gas to ensure good thermalization. We rotate the sample to achieve in- and out-of-plane applied magnetic fields by minimizing or maximizing the resonance field, respectively. We characterize the background signals in the cavity data via comparisons between the measurements with parallel and perpendicular orientations. Since the resonance fields are significantly different between the

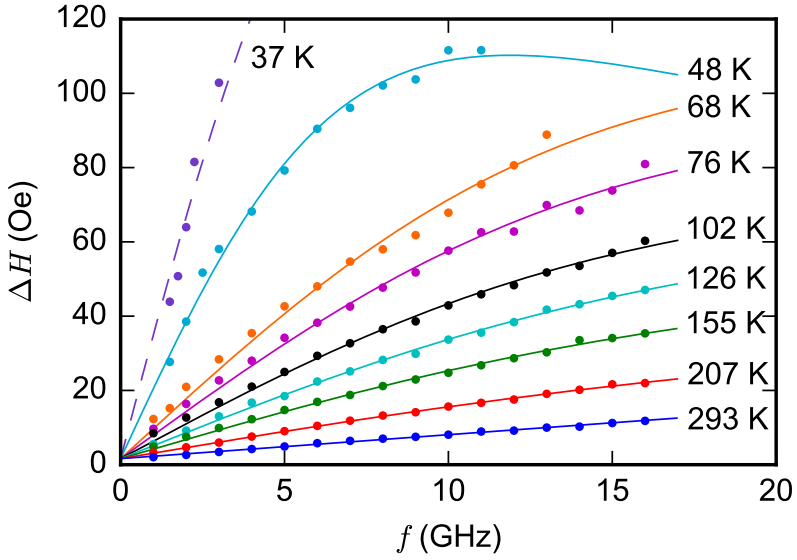

Figure 4.9: Linewidths (Lorentzian FWHM) from the in-plane FMR spectra measured at different temperatures. Solid lines are fits to the sum of the frequency dependence expected from a slowly-relaxing impurity mechanism in addition to the room temperature linear behavior. The dashed line for 37 K is a guide to the eye.

two orientations, an orthogonal FMR spectrum contains only the background signal in the field region of interest for each resonance. These background signals correspond to excitations in the substrate and other elements in the glass container that are not related to the YIG film.

Figure 4.10 shows the T dependence of the FMR linewidth in these cavity measurements, with a comparison to the broadband coplanar waveguide results. (The waveguide values are interpolated from measurements at 9 and 10 GHz.) We find excellent quantitative agreement between the two types of measurements. The cavity measurements reveal that ΔH has a maximum near 25 K, with a clear decrease at lower temperatures. The maximum linewidth is 28 times larger than the room temperature result at this frequency.

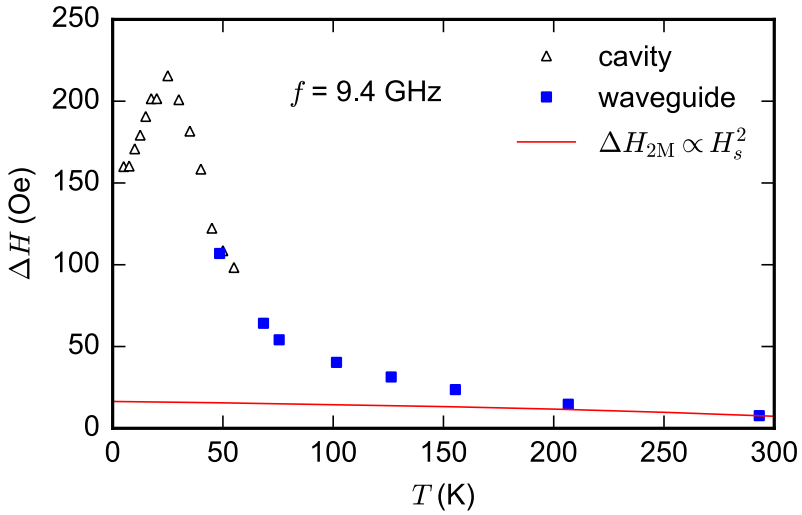

Figure 4.10: FMR linewidth at 9.4 GHz as measured by two techniques: (open black triangles) cavity measurements and (blue squares) coplanar waveguide measurements. We observe a peak near 25 K, where ΔH is 28 times larger than at room temperature. The solid red line indicates temperature dependence expected from two-magnon scattering; this dependence is too weak to explain the variation in ΔH.

4.5.3 Resonance field analysis

In order to evaluate possible mechanisms for these very strong changes in linewidth with temperature, we must first characterize how the magnetic anisotropy in the YIG film varies with temperature. We do this based on the measured FMR resonance fields, fitting to the Kittel equation for a magnetic thin film with an in-plane magnetic field [45]

$$f = \frac{|\gamma|}{2\pi}\sqrt{H_r^{\parallel}(H_r^{\parallel} + 4\pi M_{\text{eff}})}. \tag{4.3}$$

Here γ is the gyromagnetic ratio, $H_r^{\parallel}$ is the in-plane resonance field for a given fixed frequency f, and $4\pi M_{\text{eff}}$ parameterizes the shape anisotropy and any addi-

tional contributions to the perpendicular magnetic anisotropy. We obtain good fits (see Fig. 4.11(a)) with no additional in-plane anisotropy contribution. In Eq. (4.3) we do not include a renormalization shift in the resonance frequency that can result from two-magnon scattering because this is small on the scale important to our analysis [46, 47]. We also neglect a shift in resonance field that can arise from a static dipole interaction between the YIG and the paramagnetic GGG substrate [63, 64] because this is also small, less than a 1% shift for temperatures above 15 K. The values of $4\pi M_{\text{eff}}$ we obtain from the fits to Eq. (4.3) at different temperatures are shown in Fig. 4.11(b). We find that $4\pi M_{\text{eff}}$ is significantly larger than the simple shape anisotropy generated by the YIG saturation magnetization, $4\pi M_s$ (determined from vibrating sample magnetometry (VSM) measurements presented in Section 4.4), indicating the presence of a positive uniaxial anisotropy, $H_s = 4\pi M_{\text{eff}} - 4\pi M_s$, favoring an in-plane magnetization. We have confirmed the value of H_s and the form of its temperature dependence using FMR measurements with an out-of-plane magnetic field. Figure 4.11(a) shows the frequency dependence of the resonance position with an out-of-plane field at room temperature, and Fig. 4.11(b) shows the extracted value of $4\pi M_{\text{eff}}$ as a function of temperature from both waveguide and cavity FMR measurements. The large value of H_s is greater than expected from surface anisotropy [2] or magneto-crystalline anisotropy [45] of cubic YIG alone, so we tentatively ascribe the result to a growth-induced anisotropy, such as caused by tetragonal distortion. This is consistent with predictions and observations in YIG films grown by PLD [36], where the anisotropy is highly dependent on the growth conditions. The temperature dependence of H_s that we obtain is qualitatively consistent with the spin fluctuation model [65, 66], which predicts $H_s(T) \propto [M_s(T)]^2$.

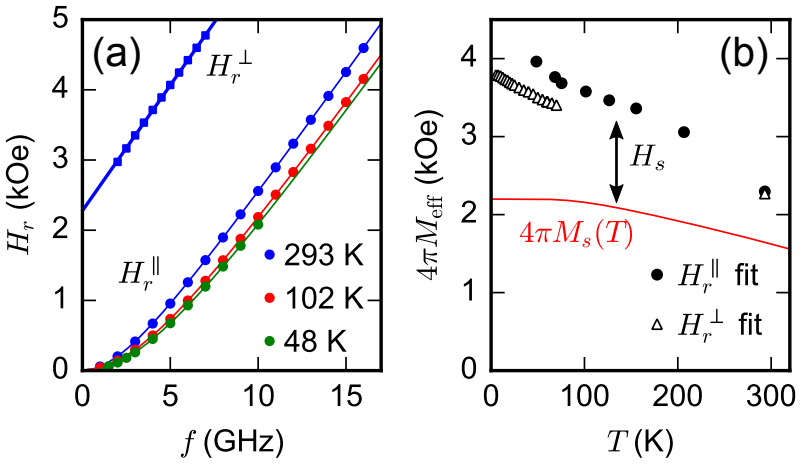

Figure 4.11: FMR resonance field as a function of frequency for (squares) an out-of-plane applied magnetic field at room temperature and (circles) and in-plane applied fields at various temperatures. Solid lines are fits to the Kittel equation. (b) Temperature dependence of the effective magnetization, determined from the Kittel fits for (black circles) in-plane and (open triangles) out-of-plane applied magnetic fields. The open triangles below 50 K are from cavity measurements. The red line is 4π times the saturation magnetization, from a fit to VSM measurements (see Section 4.4). The effective magnetization reflected in the magnetic anisotropy is significantly greater than the saturation magnetization.

4.5.4 Relaxation mechanism analysis

Given this characterization of $H_s(T)$, we can now evaluate whether two-magnon scattering from surface defects, a mechanism that is expected to be active for ultra-thin YIG films at room temperature [2, 21], is capable of explaining the large increase in the linewidth ΔH that we observe at low temperature. This effect causes a linewidth that is nonlinear with frequency f, following the form [48]

$$\Delta H_{2M} = \Gamma(T) \sin^{-1} \sqrt{\frac{\sqrt{\omega^2 + (\omega_0/2)^2} - \omega_0/2}{\sqrt{\omega^2 + (\omega_0/2)^2} + \omega_0/2}}, \tag{4.4}$$

where $\omega = 2\pi f$ and $\omega_0 = \gamma 4\pi M_{\text{eff}}(T)$. The temperature dependence in this equation is dominated by the scattering coefficient $\Gamma(T)$, whose expected temperature dependence [46] is $\Gamma(T) \propto [H_s(T)]^2$. Given our determination of $H_s(T)$ above (using M_{eff} from $H_r^{\parallel}$ fits as a worst-case scenario), the temperature dependence expected from the two-magnon scattering mechanism is illustrated by the red line in Fig. 4.10. This mechanism can explain at most a factor of 4 increase in the linewidth as the temperature is reduced from 300 to 0 K, far less than the factor of 28 that we observe. It also is incapable of explaining the peak in ΔH we measure near 25 K. Similar conclusions follow if one assumes [65, 66] that $H_s(T) \propto [M_s(T)]^2$, together with our VSM measurements of $M_s(T)$.

An alternative mechanism that can account for a much stronger temperature dependence for ΔH is impurity relaxation, for example due to rare earth or Fe^{2+} impurities in the YIG film. Researchers in the 1960's produced a rich body of literature which shows that the linewidth in bulk YIG samples can increase dramatically at low temperatures when impurity relaxation is active [11, 57–59, 67]. The frequency and temperature dependence of ΔH in our samples can be explained well using a model of slowly-relaxing impurities [11, 59, 68]. The contribution to the linewidth from this mechanism is expected to have the form

$$\Delta H_{SR} = A(T) \frac{\omega\tau}{1 + (\omega\tau)^2}, \tag{4.5}$$

where $A(T)$ is a frequency-independent prefactor and τ is a temperature-dependent time constant. The lines in Fig. 4.9 are fits assuming that

the linewidths are governed by this functional form plus a linear-in-frequency temperature-independent background contribution equal to the room-temperature dependence (Fig. 4.7(c)). The maximum near 25 K in the temperature dependence of ΔH (Fig. 4.10) is very similar to previous measurements in bulk YIG [11], and corresponds within the slowly-relaxing impurity model to the condition $\omega\tau \approx 1$.

Figure 4.12 shows the values of the fitting parameters extracted from the fits plotted in Fig. 4.9. For each value of temperature below room temperature, we fit the measured frequency dependence of the linewidth to the form

$$\Delta H = \frac{4\pi\alpha f}{|\gamma|} + \Delta H_o + A\frac{2\pi f\tau}{1+(2\pi f\tau)^2}, \tag{4.6}$$

with two adjustable fitting parameters at each temperature: A and τ. We used fixed values for the parameters $\alpha = 9.0\times10^{-4}$ and $\Delta H_o = 1.6$ Oe, as determined by a separate fit to the room temperature (293 K) data. We assume $|\gamma|/(2\pi) = 0.0028$ GHz/Oe. We do not perform a fit to the 37 K data because these data cover an insufficient range of frequency to constrain the fit parameters.

The fits indicate that $A(T)$ is approximately proportional to $1/T$, and the relaxation time τ increases with decreasing temperature so that $2\pi f\tau$ increases toward 1 as the temperature is reduced toward the temperature of the linewidth maximum. These behaviors are consistent with the usual expectations within the slowly-relaxing impurity model [11, 59].

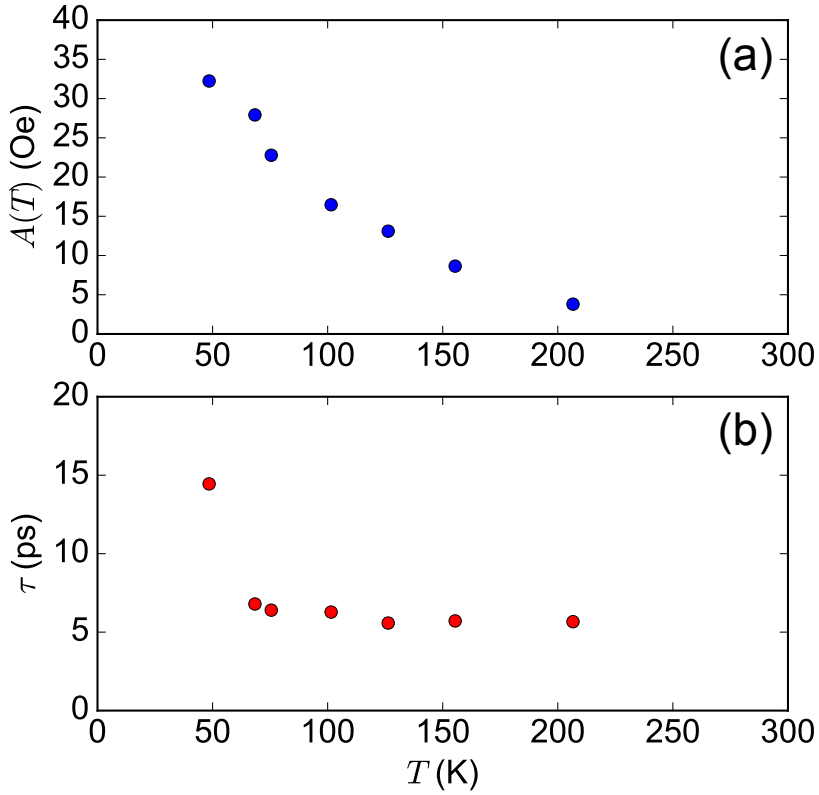

Figure 4.12: Temperature dependence of the fit parameters from Fig. 4.9 and Eq. 4.6.

4.5.5 Linewidth thickness dependence

In addition to the 15.4 nm YIG film, we measured the temperature dependence of the linewidth in two thicker YIG films: 164 nm and 250 nm. All three films are grown using the same methods described in Section 4.3. All three films exhibit a peak in the linewidth as a function of changing temperature in the range 25-30 K. As shown in Fig. 4.13, the maximum value of ΔH increases as a function of decreasing film thickness. This scaling might suggest that the impurities which cause the increased linewidth at low temperature could be located preferentially near the YIG interfaces, although the dependence on film thickness is weaker than a simple $1/t$ form.

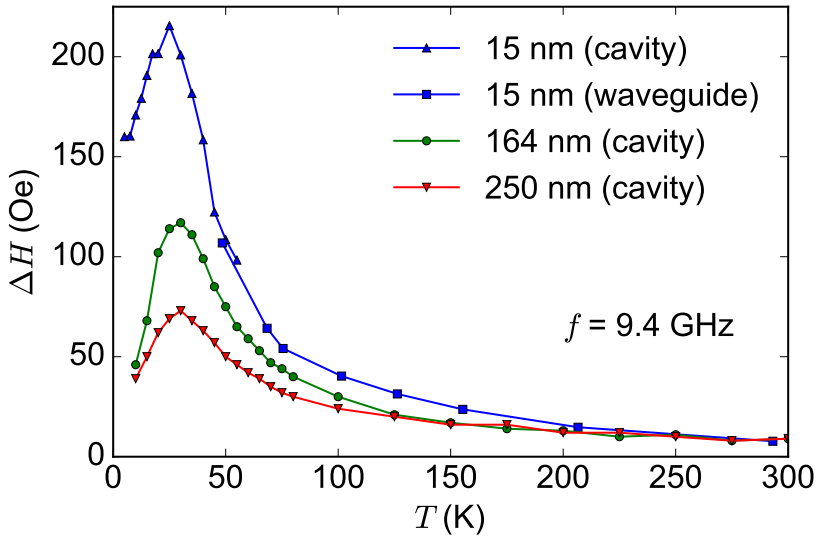

Figure 4.13: Measurements of the FMR linewidth as a function of temperature for (blue triangles, blue squares) the 15.4 nm film from Fig. 4.10, (green circles) a 164 nm film, and (red upside-down triangles) a 250 nm films. Lines are guides to the eye.

4.6 Discussion

Our measurements illustrate the dramatic increase in the linewidth that can occur when impurity relaxation mechanisms are active. As shown in Fig. 4.8, at low temperatures the signal in the broadband system approaches the noise floor. In this section, I suggest improvements to the cryogenic FMR system to better handle these broad linewidths.

During the operation of the FMR system, I increased the modulation field to enhance the signal-to-noise of broad resonances. The modulation field can reach 1/4 of the linewidth without causing distortion in the FMR spectra, which I have verified by systematically varying the modulation field strength. However, there is a limit to the field capability of the Helmholtz coils, as alluded to in Chapter 2. This stems from the amount of current that can be passed through

the coils, without the audio amplifier overheating and automatically shutting off for safety. In addition to the current limit, the oscillating magnetic field must penetrate the stainless steel cryostat. This can be seen in Fig. 4.2, where the cryostat sits in between the Helmholtz coils. Therefore, the cryostat FMR system can benefit from a better method of applying a modulation field on the sample. As discussed in Section 2.3, reducing the Helmholtz coil size can significantly enhance the maximum field strength. The space available in the cryostat should be sufficient for two small coils to be built into the base mount. The challenge in this design is to bring enough current into the cryostat to power the coils, without causing thermal effects on the sample. If this technique is successful, the FMR system can be significantly more sensitive to broad linewidths, expanding the opportunities for broadband measurements.

As I presented in Section 4.2.1, the transmission through the full RF circuit has considerably more loss than that of the room temperature waveguide (see Section 2.2.3). This reduces the overall signal-to-noise ratio in the measurements. Therefore, the measurements can benefit from further reduction of the microwave losses. The SMA to SMPM adapters can be improved by replacing them with 2.92 mm to SMPM adapters, which was not done originally for cost. These adapters could be removed from the system entirely if the RF cables in the cryostat have SMPM connectors. However, in this situation again the cost of implementing these improvements do not clearly out-weigh the transmission improvements. These are important considerations for trying to enhance the signal strength.

4.7 Conclusion

In conclusion, even when a YIG film has a narrow linewidth at room temperaure indicating an apparently high-quality film, the linewidth can still increase dramatically at low temperature, by well over an order of magnitude. This is generally undesirable. For example, this will make manipulation of YIG films by anti-damping spin-transfer torques much less efficient at low temperature, and may block it entirely for practical purposes. Based on measurements of the temperature and frequency dependence of the effect, we suggest that the increased low-temperature linewidth is due to slowly relaxing impurities, perhaps rare earth or Fe^{2+} impurities introduced during growth [11]. Given the high degree of sensitivity of the low-temperature linewidth to these impurities, we suggest that the low-T linewidth can serve as a useful figure of merit for optimizing growth protocols for ultra-thin YIG films.

CHAPTER 5

SWITCHING OF YIG NANOMAGNETS WITH SPIN-TRANSFER TORQUE

5.1 Introduction

Magnetic memory designs that take advantage of the electron spin have attracted significant scientific and commercial interest, since they promise to deliver non-volatile storage with performance and power improvements over conventional semiconductor technology. Recent research has shown that spin-transfer torque (STT) driven by the spin-Hall effect (SHE) in heavy metals (such as Pt [6], β-Ta [1], and β-W [7]) can be an efficient mechanism for switching magnetic material in a memory device. However, these devices suffer losses from shunting currents that flow through the electrically-conducting magnet (such as NiFe (Py) and CoFeB), since these currents do not contribute to the torque that switches the state of the magnet. This effect limits further research on the promising spin-Hall efficiencies of topological insulators [9, 10] and other highly resistive materials, where an electrically-insulating magnet is best suited.

Advances in the growth of the iron-garnet magnets by pulsed-laser deposition (PLD), off-axis sputtering, and molecular-beam epitaxy (MBE) now enable electrically-insulating magnets to be grown sufficiently thin to be applied in STT memory. The low intrinsic magnetic damping makes yttrium iron garnet ($Y_3F_5O_{12}$, YIG) an interesting candidate, since the critical-current density J_c required to switch the state of the magnet by spin-transfer torque scales proportionally with the damping α. In the limit where the magnet is sufficiently small in dimension to approximate a single spin (macrospin limit),

Table 5.1: Dependencies of the critical-current density in Eq. (5.1) at room temperature for YIG (10 nm) compared to CoFeB (4 nm), from Ref. [1].

Symbol	YIG (10 nm)	CoFeB (4 nm)	Name
θ_{SH}	12%	12%	Spin Hall angle of β-Ta
M_s	200 kA/m	1100 kA/m	Saturation magnetization
t	10 nm	4 nm	Magnet thickness
α	0.007	0.008	Effective magnetic damping
H_c	5 kA/m	8 kA/m	Coercive field
M_{eff}	250 kA/m	1030 kA/m	Effective magnetization

$$J_c = \frac{2e}{\hbar}\left(\frac{1}{\theta_{\mathrm{SH}}}\right)\mu_o M_s t\alpha\left(H_c + \frac{M_{\mathrm{eff}}}{2}\right) \tag{5.1}$$

in terms of the variables described in Table 5.1, and the electronic charge e, the permeability of free space μ_o, and the reduced-Planks constant $\hbar$. The feasibility of using YIG depends on the ability to build memory devices of the material that not only eliminate shunting currents, but also have properties that are advantageous to Eq. (5.1). For comparison, Table 5.1 also describes the properties of CoFeB, which have significantly larger M_s and M_{eff}. The effective damping is significantly higher in YIG than expected from the intrinsic value alone (for a 10 nm thick film in Table 5.1), since the spin-pumping effect introduces additional relaxation pathways. In addition to the optimization of J_c, the device geometry and spin-transparency are important factors that determine the actual current required to perform a switch.

In addition to the fabrication of efficient YIG devices, suitable measurement techniques for electrically-insulating memory are required. Previous studies on

YIG/Pt devices have quantified the STT generated by passing current through the Pt layer using magnetic-resonance force microscopy (MRFM) [22, 24] and magneto-optical Kerr effect (MOKE) imaging [23]. In multi-domain devices on the micron-scale, Avci *et al.* have shown that spin-transfer torque can drive reversible switching of an iron garnet at current-densities that are well below those in all-metal devices, using Hall resistance measurements on multi-domain structures [69]. Building and sensing single-domain devices that use this switching technique remains an open challenge, where the device sizes must be orders of magnitude smaller.

In this chapter, I present the fabrication of memory elements that consist of YIG nanomagnets adjacent to β-Ta spin-Hall channels. In collaboration with the Moler group at Stanford University, lead by Aaron Rosenberg, we demonstrate the detection of their magnetic state through scanning Superconducting QUantum Interference Device (scanning SQUID) microscopy. Despite our observations of magnetic switching, we do not observe STT-driven switching in these devices. In this context we discuss in detail the non-trivial constraints of fabricating devices with epitaxial YIG at the nano-scale, the effect of spin-pumping and magnetic damping on the critical-current, and the role of spin-transparency at the YIG/β-Ta interface. These insights provide directions for improvements in future designs and create the groundwork for analyzing the feasibility of single-domain YIG-based memory.

5.2 Fabrication process

The fabrication of the YIG switching devices took 5 major iterations to develop reproducible results that overcome issues with nanometer contact alignment, Joule heating, and crystal alignment. In this section, I describe the final working process by which YIG nanomagnets are fabricated, and electrical leads are attached to these structures to make working devices. Appendix B contains the worksheets that I developed for executing the process, that outline each step of the process for each layer.

Currently, epitaxial YIG films that are sufficiently thin for spin-transfer torque applications (few-tens of nanometers) have only been grown successfully on gadolinium gallium garnet ($Ga_3Ga_5O_{12}$, GGG) substrates because of the close lattice match between the two materials. While 30 nm of YIG has been crystallized on Pt [70], this requires a rapid thermal anneal after growth that may not be compatible with β-Ta. The epitaxy of as-grown films constrains our memory design to have the spin-Hall metal on top of the YIG layer, in reverse of most of the successful switching devices made of magnetic metals. Flowing current into the spin-Hall metal requires two important considerations that are unique to this geometry (Fig. 1(a)). First, for spin-Hall metals that form a native oxide (such as β-Ta and β-W), we require a capping layer that prevents oxidation, while conducting current. Second, the electrical contacts to the nanomagnets must be made without shorting significant portions of the spin-Hall metal. In this section, I present our fabrication of devices that addresses these unique challenges presented by the YIG epitaxy, and show the caveats to our approach.

5.2.1 Iron garnet and spin-Hall metal growth

We start the fabrication by growing ultra-thin YIG films on $10 \times 10 \times 0.5$ mm GGG substrates by either off-axis sputtering (with our collaborators in the Yang group at Ohio State, see Chapter 4) or molecular-beam epitaxy (with our collaborators in the Schlom group, see Chapter 3). We use (110)-oriented substrates to establish four-fold magneto-crystalline anisotropy in the plane of the YIG [45] (see Fig. 5.1(c)). Since the [001] directions have an energy barrier roughly 4 times larger than the [110] directions in the plane, this crystal orientation provides a good approximation to a two-state system (unlike (111)-oriented films that have three-fold anisotropy). It is important to note that the manufacturers MTI and CrysTec cut the GGG substrates along different crystal axes in the plane, so the alignment of the devices with respect to the crystal direction are done using a variety of angled designs on the same sample (see Section 5.2.4). Figure 5.1 shows the crystal orientations of the MTI and CrysTec substrates relative to the notches, which are used for off-axis sputtering and molecular-beam epitaxy respectively. For the remainder of this chapter, I focus on the high-quality YIG films of 10 nm thickness, grown by off-axis sputtering on MTI GGG substrates.

On the YIG films, we deposit the spin-Hall metal β-Ta and the conductive capping layer Ru, of thicknesses 6 and 4 nm respectively. To ensure the quality of the YIG/β-Ta interface, we use back-sputtering in the vacuum chamber to clean the surface before β-Ta growth, as we perform this step in a separate chamber. Variation in the spin-Hall magnetoresistance (SMR), which relates to the quality of the interface, does not have a clear correlation to this back-sputtering process in our observations. The Ru capping layer prevents the oxidation of the β-Ta layer during the device lifetime, and retains a resistivity of roughly 50 $\mu\Omega$

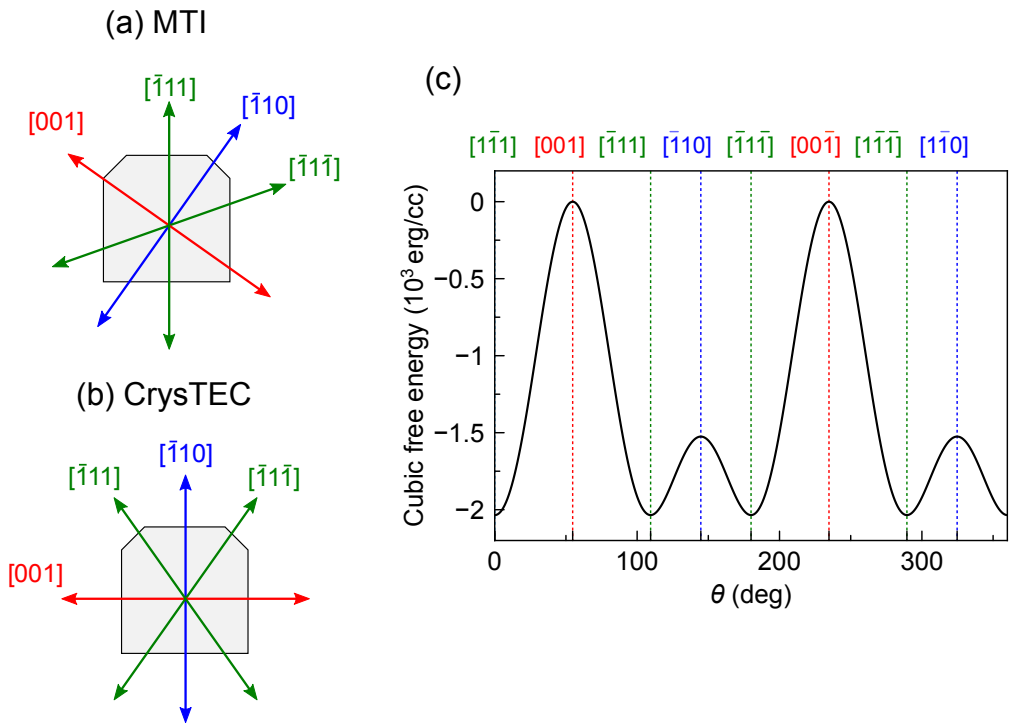

Figure 5.1: The crystal orientations of the (a) MTI and (b) CrysTec GGG substrates relative to the notches, which are used for off-axis sputtering and molecular-beam epitaxy respectively. (c) Cubic free energy prediction for YIG at room temperature, showing the relative energy landscape in the plane as a function of in-plane angle θ.

cm despite forming its own self-limiting native oxide [71]. While the Ru layer enables our design to pass current to the spin-Hall metal from the top of the device and protect the β-Ta from oxidation, this layer presents a significant disadvantage since the Ru shunts current from the β-Ta, which has a resistivity of roughly 300 $\mu\Omega$ cm [1, 72]. Through reactive ion etching experiments that simulate our most oxygen-aggressive fabrication step (Section 5.2.3), we find 4 nm of Ru to be a minimum thickness necessary to achieve consistent protection for the β-Ta.

The small size of the $10 \times 10 \times 0.5$ mm substrates requires special attention. Unlike Si-based processes, our YIG samples can not be used in many of the fabrication tools that use 4" wafers. In addition, they can be difficult to handle since there is not a significant area to grasp. I developed a technique for holding the samples using a specific type of flat tip tweezers (TDI 35A-SA) that enables the samples to be reliably processed in chemicals, and removed from hotplates. The technique ensures that the top side of the sample does not flip over, preventing scratching or damage to the devices. First I lay down a beta-wipe cloth and use normal tweezers to transfer the sample onto the beta-wipe. Then using the flat-tip tweezers, I grab the sides of the chip. Since the flat-tip tweezers have broad tips, they distribute the force across the chip edges. Lifting the sample up, the top side always faces up and the sample can be moved into a chemical bath. In the bath, the flat-tip tweezers can again grasp the edges to remove the sample. Before nitrogen drying, I place the sample on the beta-wipe and switch back to the normal tweezers, which have a more robust grip under the gas pressure. This technique also works for removing the sample from a hot-plate, where the normal tweezers can not easily get underneath the sample. This technique illustrates one of the significant operational challenges that these YIG samples pose, and is essential in the successful execution of the following fabrication layers.

5.2.2 Alignment marks

The first fabrication layer patterns the alignment marks by photolithography. Before each lithography step, I clean the samples in Acetone (typically sonicating for roughly 5 min), Isopropanol (IPA), and then dry with nitrogen gas. I also always perform a dehydration bake above 150°C for more than 4 min, which re-

Table 5.2: Photo-resist recipe for the marks layer.

Resist	Spin	Pre-bake	Approx. Thickness
LOR3A	3 krpm, 60 sec	180°C, 5 min	330 nm
S1805	3 krpm, 60 sec	115°C, 1 min 30 sec	500 nm

moves water from the sample surface and promotes resist adhesion. Table 5.2.2 contains the photo-resist recipe for defining the positive mark features. The LOR3A plays an important role in the liftoff process, by developing an undercut beneath the S1805 exposure to allow liftoff chemicals to reach the resist after metal deposition. I pattern the sample in the 5X optical-stepper using a 0.27 sec exposure and focus of 77 in transparent mode. I coarse align the sample using the notches that designate the crystal orientation and I fine align the full chip using the edges. Figure 5.2 illustrates the procedure for loading the sample and mask into the 5X, so that the reflected pattern appears correctly, relative to the crystal orientation. After exposure, I develop the sample in MIF 726 for 1 min 20 sec, rinse the sample in DI water, and dry it with nitrogen. With the positive resist developed, the open areas constitute the region where I deposit the metal marks.

The marks consist of three types. The first is a large 1×1 mm square that can be seen easily with the naked eye. This orientation-mark ensures that I can quickly distinguish the direction in which to load the sample for lithography patterning, which saves the considerable effort of repeating a pattern if the orientation is incorrect. The second marks are for the 5X stepper, to allow the large features of later layers to be aligned within 10 µm. The final marks are the global and chip alignment marks for electron-beam (e-beam) lithography. These marks are essential for the smallest features of the later layers to be aligned within 10

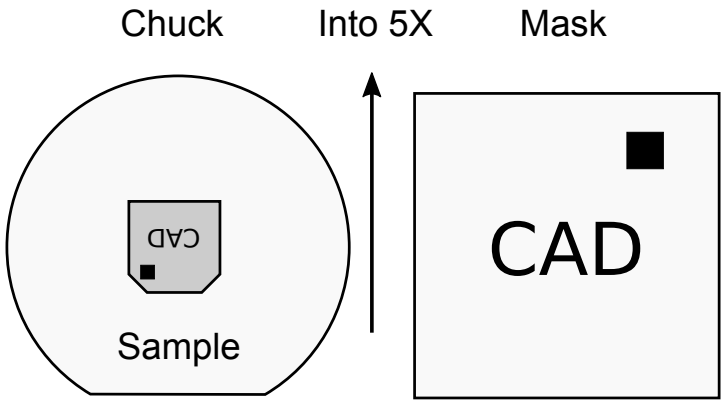

Figure 5.2: Schematic of loading of the sample and mask into the 5X, relative to the crystal notches on the GGG substrate. The (black square) orientation mark identifies the rotation of the sample, since the notches are less visible than illustrated.

nm. In the sputtering chamber, a 1 min backsputtering process provides a descum to remove resist in the patterned areas. Into these areas, I deposit 5 nm of Ti and 150 nm of Pt, using sputtering deposition. The remaining resist is removed by sonicating the pattern in the chemical 1165. In addition to the LOR3A undercut, the sonication helps to break the fencing that can occur, since the semi-conformal deposited metal from sputtering can hinder the chemical flow in the liftoff process. From 1165, I rinse the sample in IPA, and dry with nitrogen. This finishes the first lithography layer.

5.2.3 Nanomagnets

The second layer contains the nanomagnet structures, which we pattern with e-beam lithography using a JEOL 6300 tool. After the marks, the sample undergoes the same cleaning procedure and dehydration bake to prepare the sample for resist coating. Table 5.2.3 contains the e-beam resists that I apply, based

Table 5.3: Electron-beam resist recipe for the nanomagnet layer.

Resist	Spin	Pre-bake	Approx. Thickness
Omnicoat	3 krpm, 60 sec	170°C, 1 min	13 nm
PMMA 495 K 4%	3 krpm, 60 sec	170°C, 2 min	168 nm
HSQ (XR-1541) 6%	3 krpm, 60 sec	170°C, 1 min	96 nm

on the process developed by Liu [73]. When exposed to electrons, the HSQ forms silicon dioxide as a negative resist. The pattern consists of circles of outer-diameters 150, 250, 500, 800, and 1600 nm, which become the nanomagnets composed of YIG/β-Ta/Ru. The Ru layer provides essential adhesion to the resist stack. Without this layer, the HSQ process does not work effectively for the 150 or 250 nm features, which skate on the sample surface and lose their place in the aligned patterns. A more robust fabrication process involves a carbon hard-mask, originally developed by Albert [74], which I spent time investigating and applied successfully for the SQUID calibration devices [56, 75]. The carbon process can achieve superior device dimensions and consistency. However, since the HSQ process is considerably faster to execute and has less steps that can fail I use this method for the device fabrication.

The e-beam process aligns the pattern to the global and chip marks. The chip marks are partially exposed during the alignment process, so the etching pattern contains square exposures that cover the relevant chip marks. This step protects the chip marks for subsequent alignment in the next layer, which can be otherwise damaged by the partial etching. I use two beam currents to define the small and large features separately; 1 nA for the nanomagnets, and 10 nA for the four-point resistance bars (see Section 6.1), on-chip waveguide material, spin-torque FMR (ST-FMR) devices (see Section 6.2), and rectangular bars for

longitudinal spin-Seebeck detection. Writing the 1 nA features at 1250 $\mu C/cm^2$ first ensures that the beam is best stabilized for the features that need precise positioning. Using 10 nA for the larger features reduces the write time considerably for the large areas, since the beam size scales with the beam current. I apply proximity effect correction (PEC) to modulate the exposure for the larger features to account for the stochastic electron-scattering in the resist, that otherwise tends to balloon features in their horizontal dimensions. In this PEC, I use a base dose of 500 $\mu C/cm^2$ for the HSQ-PMMA-Omnicoat stack.

With the features written, I develop the sample in MIF 726 for 1 min 30 sec, which causes the exposed HSQ to form silicon dioxide. Rinsing this in DI water, and drying with nitrogen, the sample is ready to transfer the pattern from the silicon dioxide to the PMMA-Omnicoat layers. Using reactive ion etching, the sample is oxygen etched at 100 W, 50 mTorr, and 20 sccm of O_2 for 1 min 30 sec. Its important to also perform a standard oxygen clean in the chamber for at least 5 min beforehand to remove any remnant chemicals from the previous user. At this stage, the HSQ-PMMA-Omnicoat stands as a pillar above the YIG/β-Ta/Ru layer, and provides an effective negative resist for ion mill etching. The sample is etched at 150 V accelerating voltage and 35 mA beam current at 90° (170° in the tool software). To reduce heating and improve resist removal, I etch using a duty cycle with 20 sec of etching followed by 40 sec of cool-down. Figure 5.3 shows the mass spectrometry measured during a YIG(10)/β-Ta(6)/Ru(4) sample. The Ga element signal indicates the etching has passed beyond the YIG layer, which I use to judge when to stop the etching process. After the pillar etching, the sample is tilted to 30° (110° in the tool software) to clean the pillar side-wall for 1 min. This helps to remove side-wall features or crowns that may prevent the edge wires from making electrical contact.

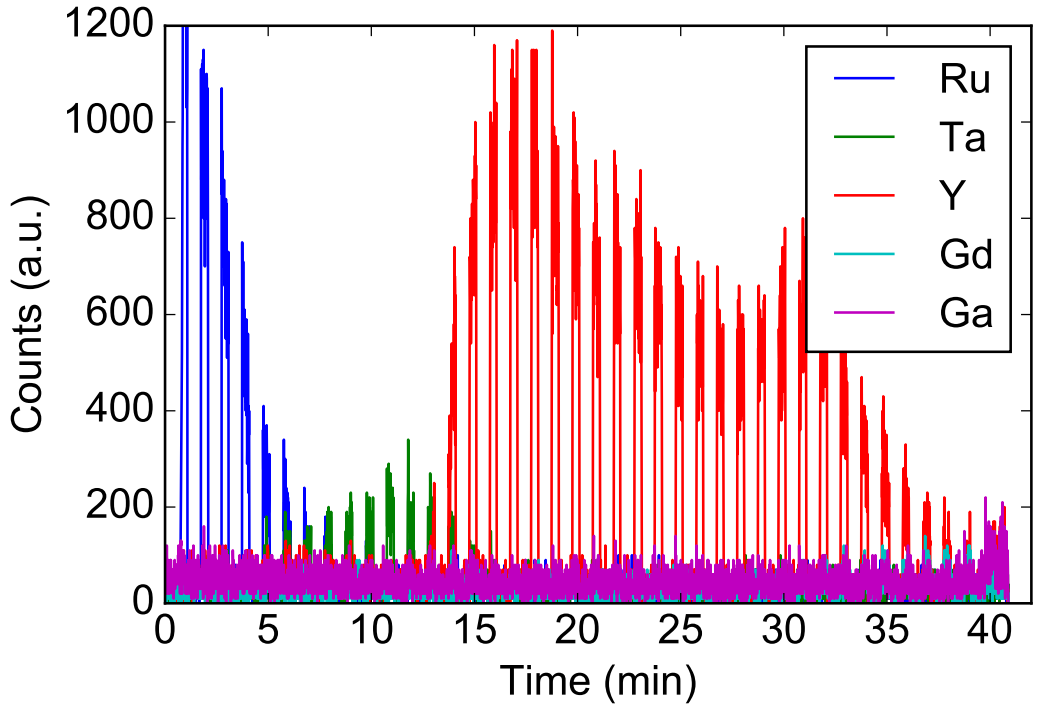

Figure 5.3: Mass spectrometer measurements of a YIG(10)/β-Ta(6)/Ru(4) device, showing the element detection of Ru, Ta, Y, Gd, and Ga as a function of etch time. A duty cycle of 20 sec of etching and 40 sec of cool-down helps prevent resist from being difficult to remove.

After the etching process, I remove the HSQ-PMMA-Omnicoat layer by soaking the sample in Remover PG on a hotplate at 170°C for 6 hr. Once the heated bath has cooled (typically the next day), I place the beaker with the Remover PG and the sample into a sonicator for 1 hr. From there, I transfer the sample to IPA, for a brief 1 min sonication, IPA spray, and nitrogen dry. Despite these steps the etching process can make the resist difficult to remove, so it is often wise to check the height of the pillar using atomic force microscopy (AFM) to ensure that the resist is gone. Figure 5.4 shows a three-dimensional view of an AFM image, examining a YIG(10)/β-Ta(6)/Ru(4) device with an outer-diameter of 500 nm. After this step, the nanomagnets on the surface need to be electrically

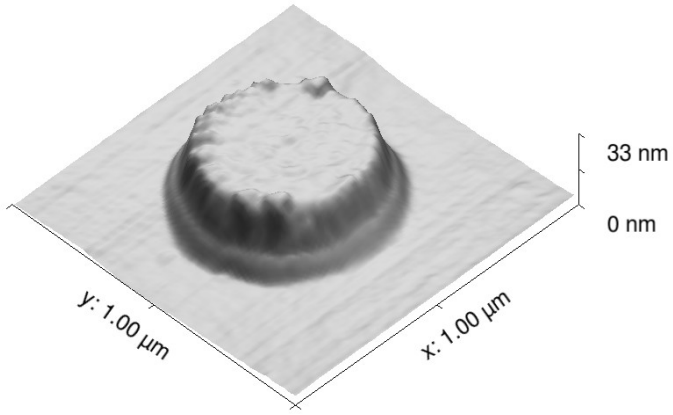

Figure 5.4: Three-dimensional view of an AFM image, examining a YIG(10)/β-Ta(6)/Ru(4) device after etching, with an outer-diameter of 500 nm.

attached.

5.2.4 Nano-scale electrical contacts

The third layer patterns the nano-scale electrical contacts through e-beam lithography. Table 5.2.4 contains the e-beam resist recipe for this layer, which again follows the clean and dehydration procedure beforehand. The PMMA bilayer provides an effective liftoff combination. Since the PMMA 495 K 4% is more sensitive to the exposure than PMMA 950 K 2%, the bottom layer creates a wider opening for liftoff chemicals (undercut) without affecting the feature sizes. The ESpacer conductive polymer provides an electrical sink for the electrons from the exposure beam, since at this step the majority of the sample is the insulating GGG substrate. Without this anti-charging layer, the Coulomb interaction can significantly shift the electrons as the pattern progresses and cause considerable distortion. Thermally evaporated Au can also be substituted as the anti-charging layer, but this process takes much longer and does not lead to

Table 5.4: Electron-beam resist recipe for the nano-scale electrical contact layer.

Resist	Spin	Pre-bake	Approx. Thickness
PMMA 495 K 4%	3 krpm, 60 sec	170°C, ≥15 min	168 nm
PMMA 950 K 2%	3 krpm, 60 sec	170°C, ≥15 min	100 nm
ESpacer 300Z	3 krpm, 60 sec	90°C, 1 min	19 nm

noticeably improved results. The only caveat to ESpacer is its limited availability and high price.

The patterning of the contact features took considerable optimization to achieve reliable electrical behavior, since the margin of error is very small when making electrical contact to the top of devices on the nanometer scale. I align this layer using the same set of alignment marks that were protected in the nanomagnet patterning, which provides overlay accuracy less than 10 nm. I made a number of trial samples that took into consideration both PEC to modulate the dose for sharpness and an additional overlap distance that gave greater precision to correct for the proximity. I exposed these patterns at a base dose of 700 $\mu C/cm^2$ for the PMMA bilayer stack. The final design considers the optimal overlap for each device size, outlined in Table 5.2.4. It is important to note that the overlap region covers a considerable percentage of the device (in CAD dimensions, where actual devices differ slightly), as seen in Table 5.2.4. This is disadvantageous, since in those regions the current shunts through the contacts and not through the device. However, in practice I found these overlaps to be necessary to provide reproducible electrical conduction through the devices, with sufficiently low Joule heating to prevent device burn out at currents below a few mA.

Table 5.5: Optimal CAD properties for the nano-scale electrical contact patterns.

Outer-diameter (nm)	Contact spacing (nm)	Contact Overlap (nm)	Total Overlap (%)	Contact width (nm)
150	70	40	53%	60
250	130	60	48%	100
500	340	80	32%	200
800	640	80	20%	320
1600	1440	80	10%	640

I account for the differing in-plane crystal orientation of the MTI and CrysTec GGG substrates by patterning devices with a variety of angles between the current flow and the crystal axes. This allows devices to be chosen for the switching experiment based on their crystal orientation, and prevents a rotation from having to be made to the entire fabrication pattern. Figure 5.5(c) shows a nanometer-scale electrical lead pattern at 35° to the horizontal (roughly 55° to the $[\bar{1}11]$ in the MTI case). Leads at 0, 35, 54, 90, 125, and 144° are also made. However, the length of the long electrical leads that I discuss in Section 5.2.6 significantly limits the number of combinations of these angles that can be made on a single chip.

5.2.5 Oxide layer for the on-chip waveguides

On the same sample, I also fabricate on-chip waveguides. While these are not discussed in this thesis, I include the necessary fabrication step here, which can

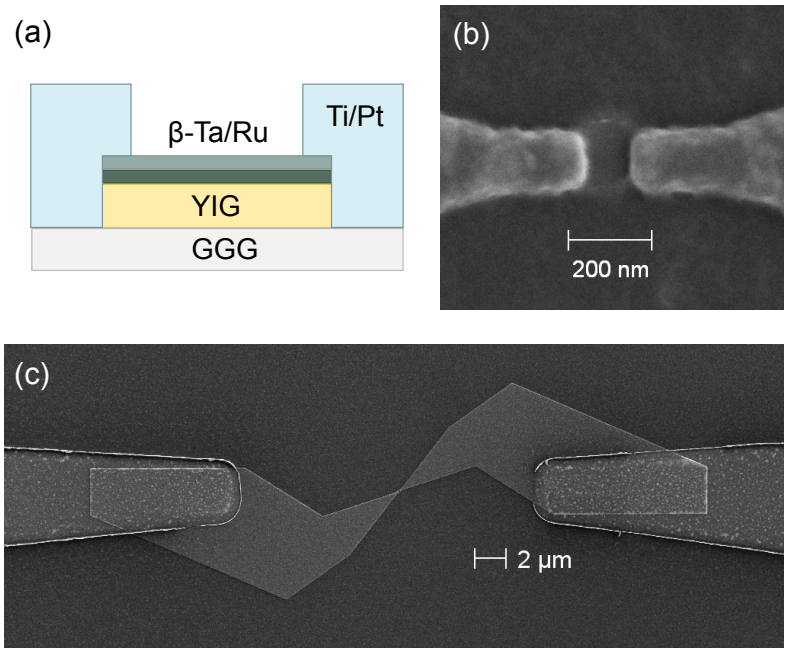

Figure 5.5: (a) Cross-sectional schematic of the device geometry illustrates the layer composition of the YIG/*beta*-Ta/Ru nanomagnet on the GGG substrate, and the Ti/Pt leads. Current flows from the (blue) Ti/Pt wires into the (light and dark green) *beta*-Ta and Ru layers. (b) Scanning electron microscope (SEM) of image of a 250 nm outer-diameter device, showing the circular nanomagnet contacted by top metal leads. A contact overlap of 50 nm is shown. (c) SEM image showing one of the angled electrical lead patterns (at 35 degrees), which illustrates that we can apply current at specific angles to the crystal axis.

otherwise be omitted. The sample undergoes the clean and dehydration procedure, followed by the same resist recipe as shown in Table 5.2.2. Repeating the 5X process of the first layer, I use the 5X alignment marks to overlay the pattern of the waveguide oxide. This step insulates the YIG/*beta*-Ta/Ru from the Ti/Pt waveguide, made in the following electrical leads layer. I deposit 100 nm of SiO_2 using sputtering deposition and liftoff using the same sonication process.

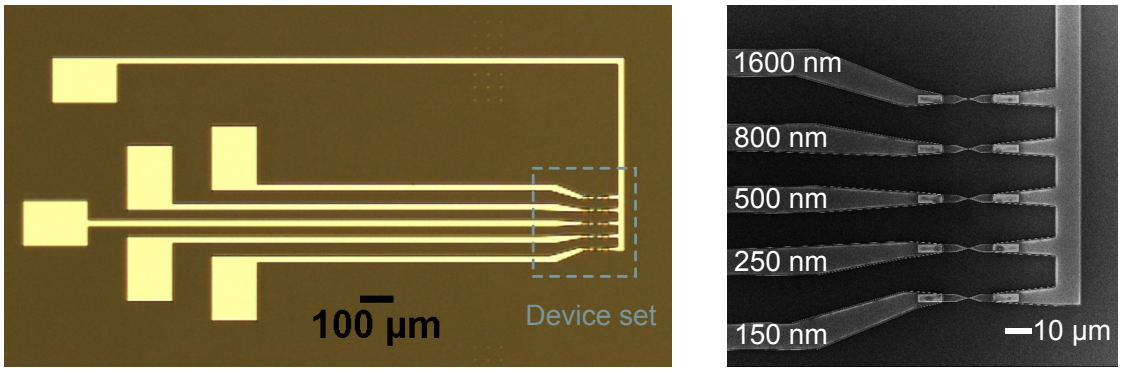

Figure 5.6: (left) Microscope image of the electrical leads pattern, showing the contact pads, the device set, and common group (the top electrical lead). (right) SEM image of the device set, containing the nanomagnets of 150, 250, 500, 800, and 1600 nm in outer-diameter along individually addressable current-paths.

5.2.6 Electrical leads

The final layer of the fabrication process defines the micron- and millimeter-scale electrical leads. I repeat the liftoff process to pattern with the aligned 5X procedure, and deposit the metal of 5 nm of Ti and 200 nm of Pt into the pattern. These leads connect to the nano-scale electrical contacts, to allow current flow through the devices. Figure 5.6 shows a microscope image of the lead pattern, which have large contact pads for wire-bonding. The leads are more than 500 µm long to prevent the scanning SQUID sensor from interfering with the wire bonds. The nanomagnet devices share a common ground, but are separately addressable through individual current paths.

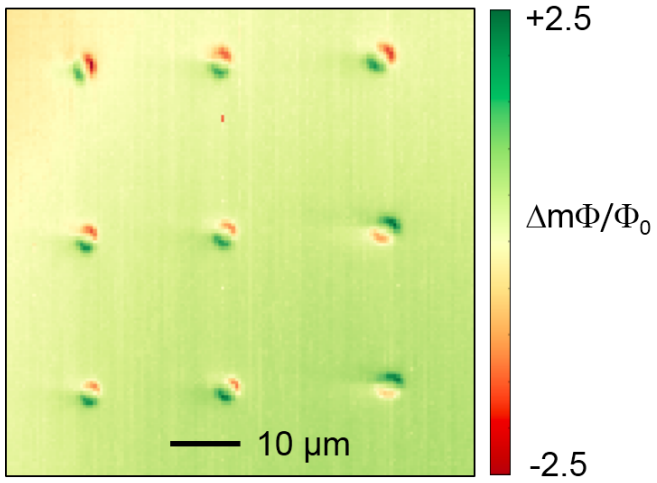

Figure 5.7: Scanning SQUID image of an array of isolated 250 nm nanomagnets of YIG(10)/β-Ta(6)/Ru(4) spaced by 20 μm, measured with a 2 μm diameter SQUID loop. Grown on MTI GGG substrates the easy-axes are in reasonable agreement with the $[\bar{1}11]$ and $[\bar{1}1\bar{1}]$ directions (Fig. 5.1).

5.3 Magnetic orientation detection

We measure the magnetic orientation of our YIG/β-Ta devices using a scanning SQUID microscope in a He^4 refrigerator [56]. The 9 K superconducting transition temperature of our SQUID sensor constrains the temperature range of our measurements. The sensor measures the magnetic flux through an on-chip 2 μm diameter pickup loop, which measures the z-component of the magnetic field convolved with the point-spread function of the pickup loop. We fix the SQUID sensor above the sample, and raster the sample using an attocube piezoelectric stack to record the flux at each point in space. Since the YIG moment lies in the plane of the sample, dictated by the demagnetization and magneto-crystalline anisotropy fields, the SQUID measures the fringe fields of the dipole moment to observe its magnetic state.

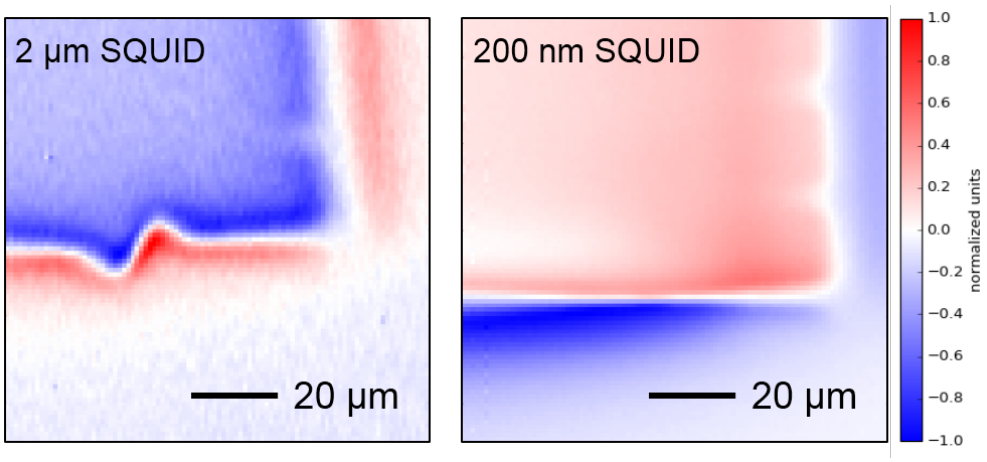

Figure 5.8: Scanning SQUID image of the AC magnetic field generated by AC current flowing in a (left) 54°contact with a 2 µm diameter SQUID and (right) 0°contact with a 200 nm diameter SQUID, detected through a lock-in amplifier. Oersted-field and current flow can be precisely determined at each part of the wire. The smaller SQUID sensor loop provides enhanced signal-to-noise.

We also use the magnetic field detection to both orient the devices in the microscope, and establish the magnetic field direction of the Oersted field produced in the devices. Figure 5.8(b) shows a SQUID image of our electrical leads when applying an AC current. The distinct geometry of our electrical leads allows us to locate the devices by their magnetic field. From DC current images we can also determine the direction of the Oersted field using the right-hand rule. This provides a reference to evaluate the symmetry of any switching events. Since β-Ta has a negative spin-Hall angle, we expect the moments to switch opposite to the Oersted-field if they are actuated by spin-transfer torque. This symmetry distinction is the main advantage of using β-Ta over Pt to generate spin-current, since the positive spin-Hall angle of Pt does not allow this comparison.

In addition to the application of current, our scanning SQUID system has the

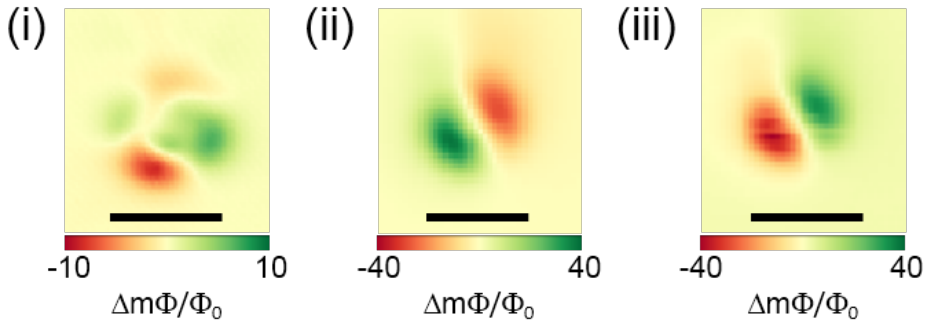

Figure 5.9: Scanning SQUID images of a 1600 nm device, showing (i) the initial magnetization in a multi-domain state, (ii) the saturation of magnetization after +60 Oe applied-field, and (iii) the reversal of the magnetization after -60 Oe applied-field. Each image has a scale bar of 5 µm, where the magnetic field is imaged at roughly 1 µm above the sample.

ability to apply in-plane magnetic fields below 100 Oe. Figure 5.9 shows that the largest YIG/β-Ta device of 1600 nm outer diameter can be initially found in a multi-domain state. By applying a field of 60 Oe at 250 K (measuring at 4 K), we show that we can both saturate the moment and reversibly switch the magnetic orientation of the device. This illustrates the sensitivity of the SQUID to the moment orientation, and the clear distinction between the three states. The multi-domain behavior indicates that our largest devices are not sufficiently exchange-coupled to be treated in the macrospin approximation. Importantly this behavior is not observed for the smaller devices.

We focus our efforts to switch the YIG nanomagnets with spin-transfer torque on the devices with 250 nm outer-diameter, since these are the smallest devices with consistent electrical behavior. As we show in Section IV, the most advantageous temperatures for switching YIG are above 150 K for our samples. Therefore, our measurement procedure consists of (i) recording the initial state of the YIG dipole moment at 4 K, (ii) heating the sample to 170 K, (iii) applying

the current to perform the switch, (iv) cooling the sample back down to 4 K, and then (v) measuring the new state of the dipole moment. In Fig. 3(c) we plot the maximum currents and temperatures that we tried for the 250 and 800 nm devices, along-side critical-current estimates we make in Section 5.4. We account for the misalignment of the initial state by multiplying the current we plot by $sin\theta$ for the angle θ between the current and the initial moment direction. We do not observe switching in any of the attempts, for positive or negative currents.

5.4 Critical-current estimates

Given the lack of current-dependent switching we observe in our devices, we provide quantitative estimates for the critical currents, and use these estimates to comment on the feasibility of improving on our results. All of the parameters in Table 5.1 vary with temperature, so we provide estimates from 50 K to room temperature. We show with Eq. (5.1) that the most important factors that influence the critical currents in our devices are the magnetic damping (including spin-pumping) and shunting currents that flow through the capping layer.

The majority of the parameters in Table 5.1 have a weak dependence on temperature. The spin-Hall angle for β-Ta has been reported to range from roughly 10% to 15% between 300 and 4 K respectively [1, 72], where we find a simple linear model captures the basic trend. The saturation magnetization in YIG monotonically increases at low-temperature, following the molecular-field model to increase by 40% from 300 to 4 K (see Section 4.4). From this M_s dependence, we estimate the strength of the magneto-crystalline anisotropy [45, 65], which constitutes the coercivity in our circular devices that do not otherwise

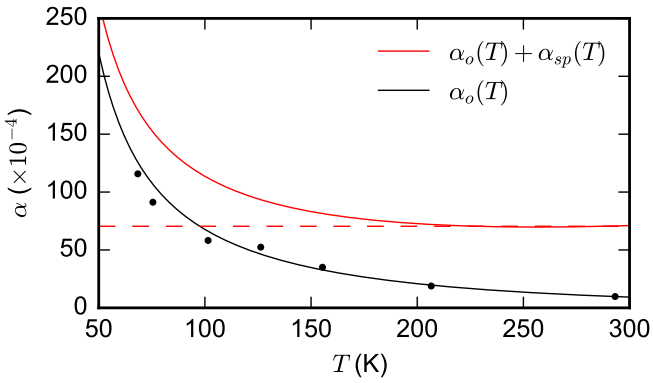

Figure 5.10: Damping estimates as a function of temperature for the (solid blue) YIG material and (solid red) the total damping, including spin pumping. We predict these values based on the worst-case slope of the temperature dependent FMR measurements in Chapter 4.

exhibit in-plane demagnetization fields. The effective magnetization ideally follows directly equivalent to M_s, however in the presence of uniaxial anisotropy, M_{eff} can take significantly higher values (see Section 4.5.3). Following the spin-fluctuation model M_{eff} increases by roughly 65% from 300 to 50 K. Overall θ_{SH}, M_s, H_c, and M_{eff} cause J_c to increase at low temperatures, making spin-torque switching less advantageous in this regime.

The magnetic damping coefficient of the YIG film α_o has a significant role in the temperature dependence of the critical current. Figure 5.10 shows worst-case estimates for the damping based on linear fits to the low-frequency dependence (below 4 GHz) of ferromagnetic resonance (FMR) measurements from Fig. 4.9, which are made on a 15 nm YIG film grown by the same technique as our YIG nanomagnets. These show that the damping increases significantly at low temperatures, and is the primary reason that we focus our measurements above 150 K. While the increase in damping is consistent with measurements

made by Shigematsu *et al.* [62], there are also reports that suggest the damping decreases at low-temperature [55]. Further research is needed to determine the optimal growth of YIG at thicknesses below 40 nm, so that it retains ultra-low damping across temperature, which has been shown to be the best-case in bulk-YIG films [58].

The spin-pumping effect characterizes the rate of spin-angular momentum flowing out of the YIG into the β-Ta, and increases the total damping. This contribution, α_{sp}, depends on the effective spin-mixing conductance $g_{\text{eff}}^{\uparrow\downarrow}$ as,

$$\alpha_{sp} = \frac{\gamma\hbar}{4\pi M_s} \frac{g_{\text{eff}}^{\uparrow\downarrow}}{t_{\text{YIG}}} \tag{5.2}$$

The total damping $\alpha = \alpha_o + \alpha_{sp}$ contributes to Eq. (5.1). We estimate the spin-mixing conductance to be 5.4×10^{18} m^{-2} from measurements in Ref. [25] on a 20 nm YIG film grown by the same method, and assume that this value does not change considerably with temperature. Figure 5.10 shows the significant increase in the damping that spin-pumping produces. This effect raises the damping value of YIG close to that of CoFeB, so that even for ultra-low damping YIG there is no significant advantage for spin-transfer torque. At low temperature, the increasing M_s reduces the overall effect of spin-pumping.

Combining all of the temperature dependencies for the variables in Eq. (5.1), we make three estimates for the critical-current in Fig. 5.12(a). The naive assumption for ultra-low damping YIG ($\alpha = 10^{-4}$) without considering spin-pumping or uniaxial anisotropy fields (affecting M_{eff}), yields J_c values of 0.4×10^9 and 0.6×10^9 A/m^2 at 300 and 50 K respectively. Including spin-pumping increases these value to 25.9×10^9 and 21.9×10^9 A/m^2 respectively. While still

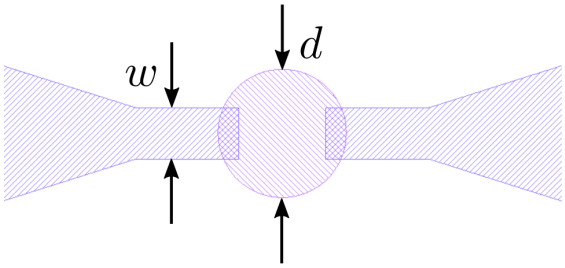

Figure 5.11: Schematic of the device geometry, with a outer-diameter d and contact lead width w.

having a weak temperature dependence, this model shows that spin-pumping constitutes a significant loss-mechanism and negates the benefits of an ultra-low magnetic damping in the material. Finally, Fig. 5.12(a) shows a model that considers all of the relevant estimates we discuss, including the YIG damping increase at low-temperatures and the uniaxial anisotropy in the M_{eff}. These two effects constitute both a large increase at room temperature, to 40.1×10^9 A/m^2, and a significant temperature dependence that negatively effects the ability to use spin-transfer torque. It is important to note that the lower saturation magnetization in YIG plays a significant role in this comparison (see Table 5.1), which is disadvantageous for thermal stability as it results in a lower energy barrier to thermal fluctuations.

The device geometry dictates the current density that flows through the cross-sectional area adjacent to the magnet. We correlate the critical-current density J_c to the critical-current I_c through the geometry specified in Table 5.2.4, which can be visualized in Fig. 5.11. We estimate the cross-sectional area as the product of the β-Ta thickness and the mean of the outer-diameter and the conductor-width. This approach approximates the complex and spatially non-uniform current density for this geometry, and provides a sufficient estimate.

Given the critical current, we are now in a position to evaluate the shunting current from the 4 nm Ru cap (introduced in Section 5.2.1). We determine the shunted current by the ratio of the resistances of the β-Ta and Ru (partially oxidized to RuO_2). We describe the total current as

$$I = I_{\mathrm{Ta}} + I_{\mathrm{Ru}} = I_{\mathrm{Ta}}\left(1 + \frac{\rho_{\mathrm{Ta}} t_{\mathrm{Ta}}}{\rho_{\mathrm{Ru}} t_{\mathrm{Ru}}}\right) \tag{5.3}$$

in terms of the current I, resistivity ρ, and thickness t of the respective layers. For our YIG/β-Ta(6)/Ru(4) devices, using the resistivity values introduced in Section 5.2.1, we find that only 14% of the current flows through the β-Ta layer. This is a significant reduction in the efficiency of the conversion between the current and the spin-transfer torque. However, we find that the Ru capping layer is a practical necessity for retaining low-resistance contacts while protecting the β-Ta from oxidation and enabling our lithography process. Future work can make significant gains by developing a new solution to the capping of β-Ta.

Figure 5.12(b) presents our estimates of the total temperature dependence of the critical current for the 250 and 800 nm devices given the worst-case J_c model. Despite the large influence that the magnetic damping and the Ru shunting current play in the critical-current, these values are in a region that is experimentally reasonable. Figure 5.12(b) also shows the applied currents that are experimentally examined, where no switching is observed. These currents are reduced by a factor of $\sin(54^\circ)$ to account for misalignment of the current and the initial magnetic state, which we measure from the SQUID images. The lack of switching in our devices at currents that exceed our estimates likely suggests that the spin transparency plays an important role, which we do not account for in these models. Spin transparency has the effect of a reduced spin-transfer

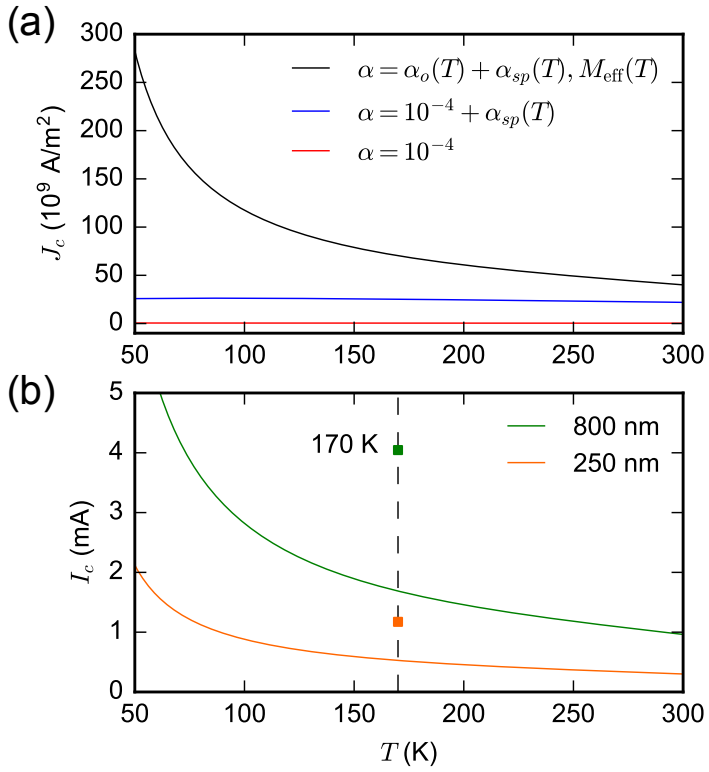

Figure 5.12: (a) Critical-current density estimates for (solid red) the naive case of a constant damping of 10-4 and no uniaxial anisotropy, (solid blue) the naive case including spin-pumping, and (solid black) the best estimates considering all parameters. (b) Critical-current estimates as a function of temperature for the (solid orange) 250 nm and (solid green) 800 nm devices, in comparison to the maximum experimental currents observed without switching for the (orange square) 250 nm and (green square) 800 nm devices. Experimental currents are reduced by sin(54°) to account for misalignment of the current and the initial magnetic state.

torque efficiency relative to effective spin-mixing conductance determined from spin pumping [76, 77], which would increase our estimates. If our assumption of macrospin behavior breaks down, the excitation of non-uniform spin-wave modes (the Suhl instability) can significantly impact our predictions.

We can also predict the Oersted field generated by the current flowing in the devices. We estimate the Oersted-field by integrating the Biot-Savart law, approximating the device as a rectangular wire using the dimensions from the cross-sectional area discussion. As in that analysis, these estimates can be made more precise by simulating the current flow. We find that for all device sizes with currents below 10 mA, the fields are less than 3 Oe. Therefore, the Oersted-field plays a very small role in comparison to the coercivity and the spin-transfer torque predicted for these currents.

5.5 Spin-Hall magnetoresistance

Given that we observe a lack of switching in our devices, it is important to examine the spin transparency of the YIG/β-Ta interface. Since the spin-Hall magnetoresistance (SMR) relies on both a sufficiently strong inverse-spin Hall effect (ISHE) and STT across the interface, the strength of the SMR is indicative of the flow of spin-angular momentum in both directions across the interface.

The four-point devices that we study for SMR are from the same sample as the SQUID devices. Figure 5.13(a) shows the device geometry. We measure the DC voltage for a given current, along different in-plane angles θ, by rotating a fixed applied field $\vec{H}_{ext}$ of 800 Oe. This field is far above the coercivity of the YIG, so the moment tracks the applied field.

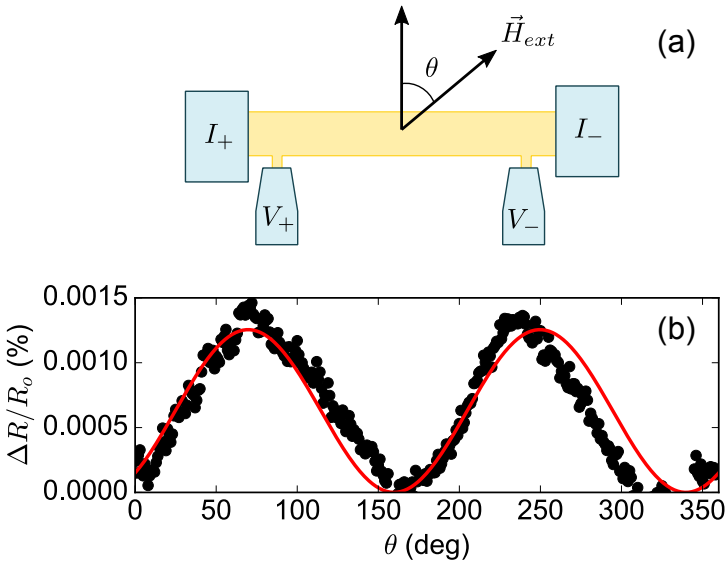

Figure 5.13: (a) Schematic of 10 µm by 80 µm four-point device for SMR measurements, made on the same sample as the SQUID devices. (b) (black) SMR measurements, in terms of the in-plane field angle. The applied field is fixed at 800 Oe. Despite minor discrepancies, the data follows the (solid red) expected sine-squared behavior.

Figure 5.13(b) shows the angular dependence of the SMR, for a base resistance of 1233.43 Ω and a total magnetoresistance (MR) of 0.0013%. At this signal strength we observe systematic drift in our measurements from thermal fluctuations, which create noticeable deviations in Fig. 5.13(b) from the sine-squared expectations. Although this MR is almost 2 orders of magnitude smaller than typical reports on Pt [78], the shorter spin-diffusion length in β-Ta has been attributed to these differences [78], and this explanation is qualitatively consistent with our results. These SMR measurements suggest that the STT effect is active, but the limited literature results prevent a strong correlation to the spin transparency of the interface.

5.6 Discussion

In demonstrating a method for fabricating YIG nanomagnets for memory devices actuated by spin-transfer torque and observing their magnetic state, we have faced a number of considerable challenges. In this section, I outline areas of improvement that can have a significant affect on future devices. These focus on using the spin-Hall metal Pt, since many of the issues that we observe are related to the oxidation of β-Ta. The main reason that we chose to focus on β-Ta in our experiments was the clear symmetry distinction in the switching between spin-torque and the Oersted-field. However, our estimates suggest that the Oersted-field should not play a significant role at reasonable values of current. Therefore, the advantages of using Pt are worth the loss of this distinction.

The shunting currents that we observe in the β-Ta(6)/Ru(4) layer through the cap can be reduced significantly by using Pt. Since Pt does not oxidize, we only need a 2 nm layer of Ru to ensure that the HSQ-PMMA-Omnicoat layer has sufficient adhesion during the fabrication (see Section 5.2.3). In Pt(6)/Ru(2), 75% of the current flows in the Pt layer (having a resistivity of 11 $\mu\Omega$/cm at room temperature). This is almost 5 times more current than in the β-Ta(6)/Ru(4) layer that we observed, and constitutes a significant advantage. The spin-Hall angle will be reduced in Pt to roughly 7% [79], which is a slight disadvantage. Unlike β-Ta, the SMR signal can be easily measured for YIG/Pt multi-layers (see Section 6.1), which provides a more effective method for quantifying the spin-transparency of the interface and determining the spin-diffusion length. There is also the potential for quantifying the spin-torque through spin-torque FMR (ST-FMR measurements), as I present Section 6.2.

While I have optimized the HSQ-PMMA-Omnicoat process to enable the reproducible fabrication of nanomagnets, this process has significant disadvantages. The carbon hard-mask process has superior resolution for making smaller devices and in practice I have found it to more reliably produce these small sizes. This would also eliminate the need for the the Ru capping layer completely, so that all of the current could flow in the Pt layer. The carbon hard-mask process uses a Cr layer to pattern the carbon, which needs to be sufficiently thick (around 15 nm) in order to protect the carbon during pattern transfer from the Cr. However, in a shallow etch I have found that the Cr may not be removed during the etch, which is an essential for removing the C/Cr layer from the top of the device. To make top contact to the nanomagnet, this process needs to be refined. I made initial investigations into a new process, where the Cr layer is replaced by Al. This is a considerable advantage over Cr, since the Al can be removed with MIF 726 (the typical developer for photolithography). In this C/Al process, any Al that has not been etched can be removed chemically without damaging the remaining device. Further work is required to demonstrate this C/Al process, but it holds significant promise for replacing the C/Cr hard-mask and enabling the fabrication of smaller devices.

The crystallization of YIG on Pt [70] provides an important step forward in removing the epitaxy constraint that sets our device design. Further investigation is necessary to see if YIG films can be grown in this configuration with thicknesses below 30 nm.

5.7 Conclusion

In conclusion, we have demonstrated the fabrication of YIG nanomagnets with dimensions down to 250 nm. Using scanning SQUID, we show that the in-plane magnetic state of the devices can be accurately determined at these sizes. However, our investigation reveals a number of important challenges for building feasible devices to study the spin-transfer torque effect. The epitaxial constraints of the YIG material limit our ability to fabricate devices, by forcing the spin Hall metal to be deposited on the top of the device. As we show, this is a considerable disadvantage for β-Ta, since it requires a conductive capping layer that shunts the majority of the current from the spin-Hall layer. We also show that the four-fold crystal structure of YIG provides additional complications to the energy landscape, and that temperature plays an important role in the critical-current. Despite these challenges, our critical-current estimates suggest that switching should be experimentally realizable, so our observation of a lack of switching may point to issues with spin transparency. Overall, our investigation provides important groundwork for the further study of spin-torque on electrically-insulating materials and suggests further work with YIG/Pt devices.

CHAPTER 6

OUTLOOK

There are still many promising ways to investigate spin-transfer torque on iron garnets, beyond the nanomagnet devices of Chapter 5. In this final chapter, I examine two measurements that I performed on yttrium iron garnet ($Y_3Fe_5O_{12}$, YIG) samples with the spin-Hall metal Pt. These results suggest that anti-damping torque can influence the YIG moment, and provide new evidence to quantify this effect.

6.1 Spin-Hall magnetoresistance

The spin-Hall magnetoresistance (SMR) measures the angle θ between the magnetic moment $\vec{M}$ and the spin-polarization $\vec{\sigma}$ [78].

$$R = R_o + \Delta R \sin^2 \theta \tag{6.1}$$

By applying an external field parallel or anti-parallel to the spin-polarization direction, the moment is expected to experience a damping or anti-damping torque respectively from spin-transfer torque. Deviations in the moment orientation between these two situations can produce an SMR signal that reflects the strength of the spin-transfer torque. In this section, I investigate YIG/Pt devices that show a significant difference when sweeping the applied field along the spin-polarization direction, and discuss the possibility of using SMR to detect and quantify spin-torque using this technique.

We deposit Pt(6)/Ru(2) onto YIG samples grown by off-axis sputtering by

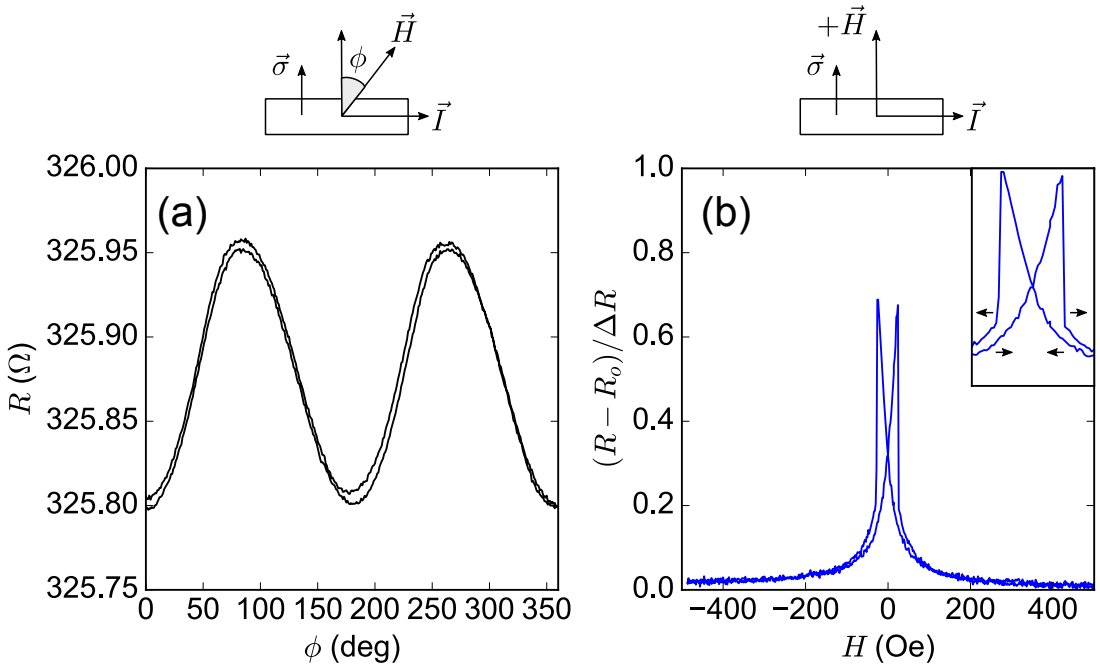

Figure 6.1: SMR of a YIG(10)/Pt(6)/Ru(2) device as a function of (a) sweeping the in-plane angle ϕ keeping the external field fixed at 500 Oe, and (b) sweeping the external field along the direction of the spin-polarization. The current is 3 mA for both measurements, and traces are made from the minimum value up to the maximum, and then back to the minimum to examine hysteresis. The inset in (b) illustrates the sweep direction correspondence.

the Yang group at Ohio State University (see Section 4.3 and 5.2.1). Here I discuss films grown on (110)-oriented gadolinium gallium garnet ($Ga_3Gd_5O_{12}$, GGG) substrates. I pattern 100 µm by 10 µm bars of YIG/Pt(6)/Ru(2) with photolithography using S1805 as a positive etch mask and the 5X process described in Section 5.2.2. I etch the bars with the ion mill following Section 5.2.3. Thick electrical leads in the four-point geometry are patterned using the process from Section 5.2.6, which allow current to flow across the Pt(6)/Ru(2) bars.

I perform DC resistance measurements on these four-point devices using

a current source (Yokogawa 7651) and a voltmeter (Keithley 2000). This configuration has superior dynamic range compared a lock-in amplifier. I apply an external magnetic field in the plane using a projected field magnet (GMW 5201). Figure 6.1(a) shows the SMR of a YIG(10)/Pt(6)/Ru(2) device for an applied field of 500 Oe at different in-plane angles ϕ. This measurement yields the total resistance change ΔR and SMR ratio ($\Delta R/R_o$) of 0.161(4) Ω and 0.049(2)% respectively. In these measurements I assume that the SMR ratio is consistent across devices, and use this ratio to calculate ΔR for the field-swept traces that do not reach the full maximum resistance value. Comparing the signal in field-swept measurements suggests that this is a reasonable approximation to better than 5%.

I measure the dependence of the SMR on the applied field along the direction of the spin-polarization. By aligning the long end of the four-point bar (along the direction of current) perpendicular to the applied field I achieve this orientation within a few degrees using manual alignment. Figure 6.1(b) shows the SMR behavior as a function of sweeping the applied field from negative to positive field, and then back to negative field at 3 mA. I subtract a remnant field of 14 Oe from the projected field magnet determined by the loop center in a 1 mA field-sweep. A clear hysteresis behavior is observed that is symmetric in positive and negative field.

Increasing the current causes a significant difference in the symmetry of the positive and negative field behavior. Figure 6.2 shows that at 10 mA with a negative field the moment does not align with the magnetic field (along the spin-polarization direction) until fields of below -500 Oe. This is in sharp contrast to the positive field behavior, where the moment aligns with the field at less than

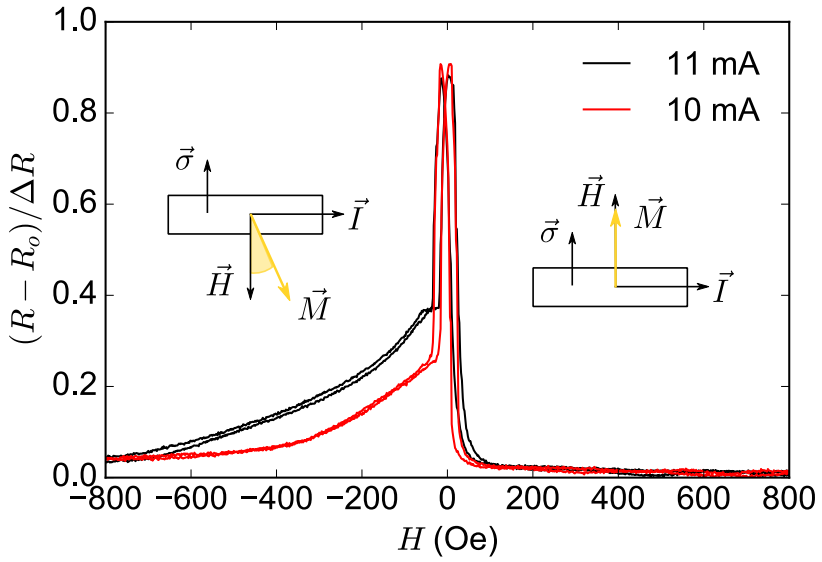

Figure 6.2: SMR of a YIG(10)/Pt(6)/Ru(2) device as a function of sweeping the external field along the direction of the spin-polarization. Compared to SMR behavior at 3 mA in Fig. 6.1(a), there is a significant asymmetry between the positive and negative field behavior at (solid red) 10 and (solid black) 11 mA.

50 Oe. There is no significant shift in the field scale, suggesting that the Oersted field does not play a significant role. At 11 mA the asymmetry increases, requiring more applied field to align the moment with it.

These results are consistent with the action of spin-transfer torque. In the negative field case, the spin-polarization provides an anti-damping torque in opposition to aligning with the applied field. This causes the moment to be misaligned with the applied field for this field polarity. In the positive field case, the spin-polarization enhances the damping torque and causes the moment to align with the applied field. This behavior is symmetric upon reversing both the applied current and magnetic field simultaneously, which is consistent with the action of spin-transfer torque.

I quantify the current dependence of the asymmetry effect by identifying

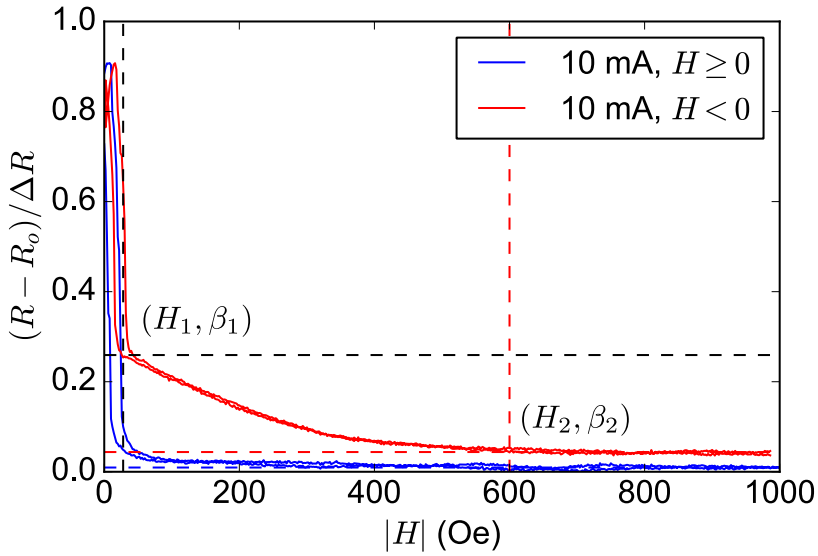

Figure 6.3: SMR as a function of the absolute value of the field for 10 mA, overlaying the (solid blue) positive field and (solid red) negative field behavior. The fields H_1 and H_2 are established systematically by the gradient of the SMR.

three important characteristics. First, H_1 characterizes the field above the low-field hysteresis behavior. Second, H_2 identifies the field required to align the magnetization with the applied field. At both of these fields the $(R - R_o)/\Delta R$ values of β_1 and β_2 respectively yield a misalignment angle.

$$\theta_o = \sin^{-1}(\sqrt{\beta_1 - \beta_2}) \tag{6.2}$$

This angle represents the maximum misalignment angle of the moment outside of the low-field hysteresis. Figure 6.3 shows the 10 mA measurement as a function of absolute value field, and the definition of the parameters. The high field discrepancy between the positive and negative fields necessitates subtracting the β_2 offset in Eq. (6.2). This difference is likely related to thermal effects, such as the spin-Seebeck effect, but I will not investigate it further here.

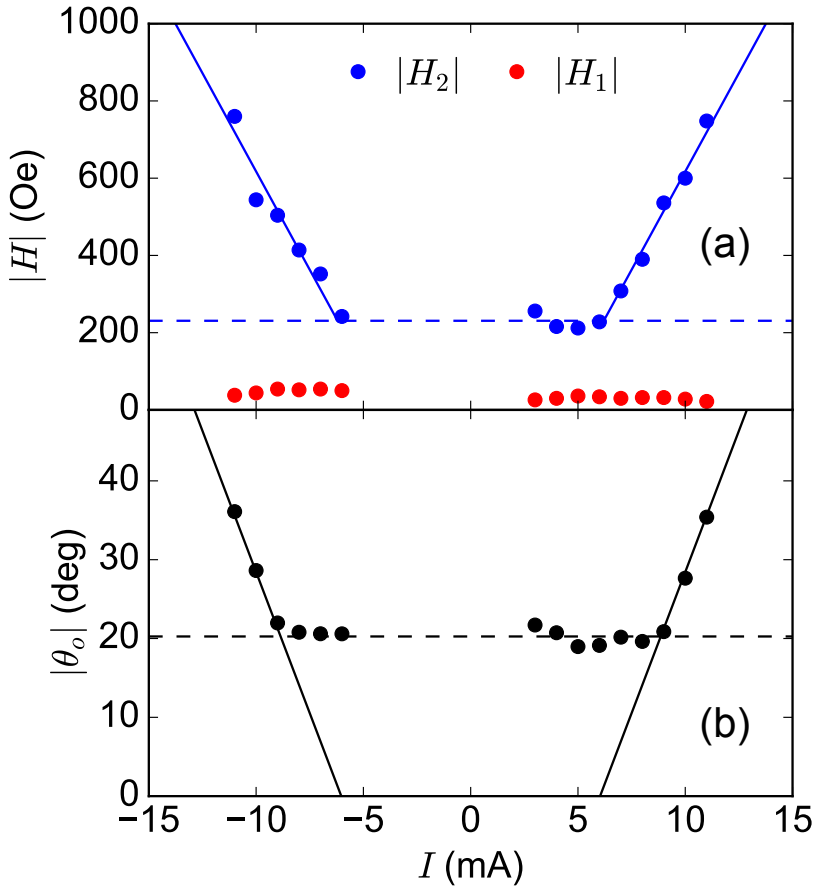

Figure 6.4: (a) The absolute value of the characteristic parameters H_1 and H_2, as well as (b) the misalignment angle θ_o, as a function of current.

Figure 6.4 shows the current dependence of the parameters H_1, H_2, and θ_o. I find a clear linear dependence in both H_2 and θ_o with current. Both effects appear to turn on at roughly 6 mA. They scale as $H_2(I) = I \times 101.8\,\text{Oe/mA} - 400.6\,\text{Oe}$ and $\theta_o(I) = I \times 7.2\,\text{deg/mA} - 43.2\,\text{deg}$. Currents above 11 mA have considerable Joule heating that causes irreversible resistance increases during the measurement. At roughly 15 mA, I find the devices burn out. While this limits our current range, the observations have sufficient signal to noise to demonstrate a clear current dependence.

Further work is necessary to quantify the relationship between spin-transfer torque and the linear dependence that I observe in the H_2 and θ_o parameters. Minh-Hai Nguyen in the Buhrman group at Cornell University has already made significant progress in interpreting the data using macrospin models. Since this measurement is extremely easy to perform on YIG devices, if we can establish a method for quantifying the spin-transfer torque from this data, then we can quickly characterize the quality of the interface between the YIG and a spin-Hall material. It is important to note that in similar devices with 20 nm YIG, two times thicker than the films shown here, I do not see this effect. This evidence gives a preliminary look at the strength of spin-transfer torque in these systems. With further research, this technique may provide rapid and quantitative characterization of spin-torque in iron garnet devices.

6.2 Spin-torque ferromagnetic resonance

Spin-torque ferromagnetic resonance (ST-FMR) has been established as an effective technique for measuring spin-transfer torque in devices with metallic ferromagnets [1, 9, 79–81]. Recently ST-FMR has been theorized [82] and experimentally demonstrated in YIG devices [83, 84]. In this section, I describe ST-FMR measurements that I performed using a DC current bias to examine the strength of spin-transfer torque on iron garnets. I measured devices from the same YIG(10)/Pt(6)/Ru(2) sample as those in Section 6.1, where I have described the fabrication details. The ST-FMR devices follow the same design from Ref. [9] and full technique details can be found in the theses of Liu [73] and Mellnik [85].

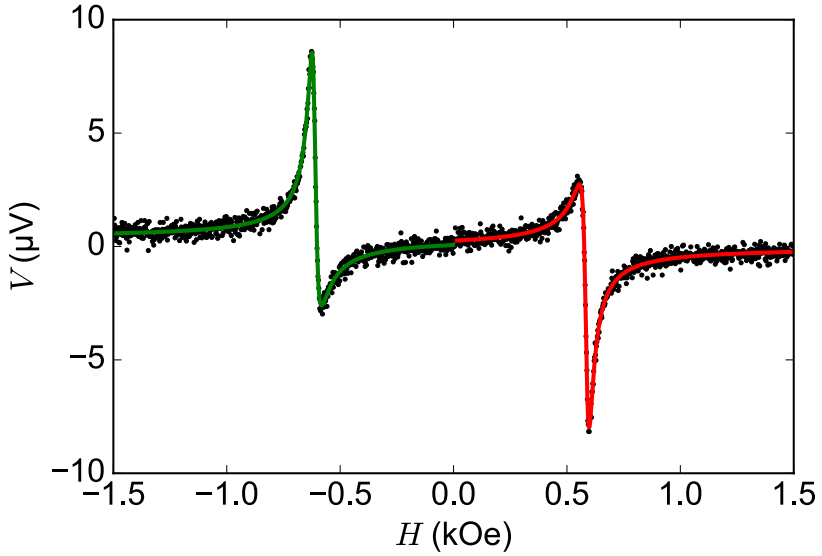

Figure 6.5: ST-FMR mixing voltage as a function of applied field at 4 GHz without DC current, showing the (black circles) raw data, (solid green) negative field fit, and (solid red) positive field fit.

Figure 6.5 shows a representative ST-FMR measurement at 4 GHz without an applied DC current. I fit the experimental data separately in the positive and negative field regions, using the sum of an anti-symmetric and symmetric Lorentzian [73, 85]. Performing measurements from 2 to 6 GHz, I examine the linewidth Δ change as a function of frequency f (shown in Figure 6.6), from both the positive and negative field fits. I extract the damping from the average of these results. A linear dependence $\Delta = 2\pi f/|\gamma|$ characterizes the damping as $\alpha = 0.0096(3)$ and inhomoegenous linewidth of $\Delta_o = 4.4(3)$ with a gyromagnetic ratio of $|\gamma|/2\pi = 0.0028$ GHz/Oe. This large damping value is consistent with the effect of spin pumping from the Pt spin-Hall layer.

Using a microwave bias-tee, I apply DC current along the length of the ST-FMR device to measure the change in linewidth. Figure 6.7 shows the affect of current on the positive and negative field linewidths at 4 GHz. These prelimi-

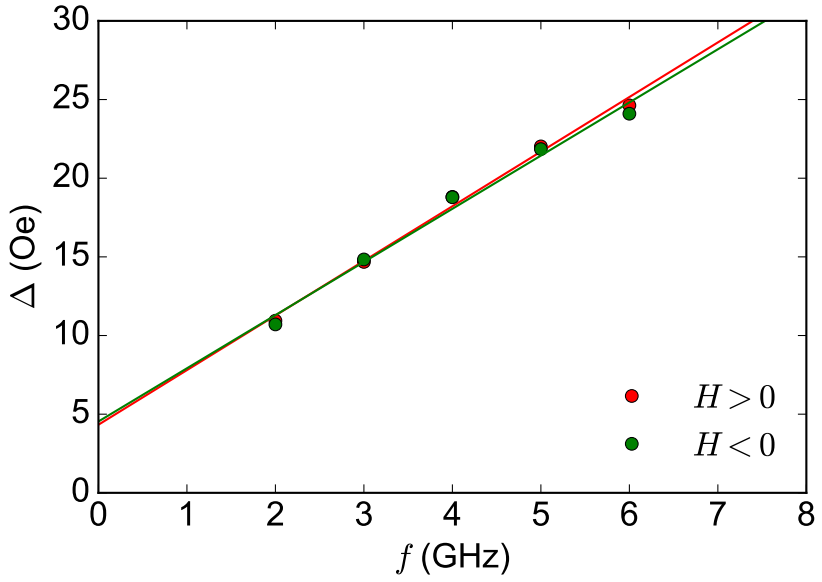

Figure 6.6: ST-FMR linewidth as a function of frequency showing the (red circle) positive linewidth and (green circle) negative linewidth data. Solid lines are fits to linear damping respectively.

nary measurements have a clear linear dependence for $|I| < 4$ mA. In this region I find slopes of 0.7(3) Oe/mA and -1.1(2) Oe/mA, which are in reasonable agreement with lines of negative slope. This YIG(10)/Pt(6)/Ru(2) device has an 8 µm wide bar, for a cross-sectional area of 4.8×10^{-10} cm^2, where only 75% of the current flows through the Pt due to the Ru cap. On average this provides a damping change per unit current-density of $\Delta\alpha/J_c = 6(1) \times 10^{-11}$ (A/cm^2)$^{-1}$, which is similar to the value of $\Delta\alpha/J_c = 9.0(1) \times 10^{-11}$ (A/cm^2)$^{-1}$ found for Pt(6)/Py(4) [79]. In Fig 6.7 at 6 mA, the mixing voltage has a large background signal that interferes with the determination of the linewidth.

The zero linewidth intercepts of the extrapolated linear-fits in Fig. 6.7 provide an estimate from the critical current. The average intercept magnitude is 10.3±3.5 mA, which translates to a critical-current density of $287(97) \times 10^9$ A/m^2 for our YIG(10)/Pt(6)/Ru(2) device, considering the shunting through the Ru

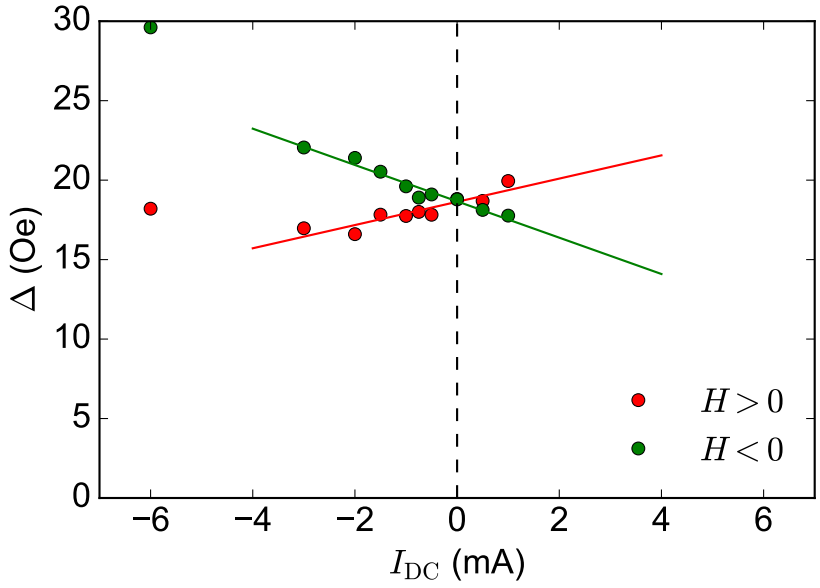

Figure 6.7: Current dependence of the ST-FMR linewidth at 4 GHz, showing the (red circle) positive linewidth and (green circle) negative linewidth data. Solid lines are linear fits respectively.

layer. This is roughly 7 times larger than the critical-current density estimates in Section 5.4 for YIG(10)/β-Ta(6)/Ru(2) devices at room temperature. However, our YIG/Pt estimate compares well with the value of 234×10^9 A/m^2 found in in thulium iron garnet ($Tm_3Fe_5O_{12}$, TmIG) samples of TmIG(8)/Pt(5) [69]. These results highlight the importance of understanding the spin transparency, which were not considered in the YIG/β-Ta estimates.

The change in damping as a function of current density relates to the spin-current density at the interface J_s [73, 79].

$$\frac{\Delta\alpha}{J_c} = \frac{\sin\theta}{(H_{\text{ext}} + 0.5M_{\text{eff}})\mu_o M_s t}\left(\frac{\hbar}{2e}\right)J_s \tag{6.3}$$

This depends on the external field H_{ext} and its angle θ (we use 45° and -135° consistent with the standard technique), the effective magnetization M_{eff}, satu-

ration magnetization M_s, YIG thickness t, permeability of free space μ_o, reduced Plank's constant $\hbar$, and electron charge e. I determine an effective magnetization of M_{eff} = 181 emu/cc from the resonance field behavior at zero current. Assuming a saturation magnetization of 140 emu/cc (see Fig. 4.6), yields a value of J_s/J_c = 0.007(3). This is significantly smaller than reports in Pt(6)/Py(4) of 0.048(7) [79], where M_{eff}, M_s, and t are consistent with the difference given $\Delta\alpha/J_c$. This again suggests that our YIG(10)/Pt(6)/Ru(2) sample is less efficient at exciting spin-transfer torque because a significant fraction of the spin current does not transfer across the interface.

Further research is necessary to examine YIG films of different thickness, and to perform a more detailed study of the current dependence. While I demonstrate that making current-dependent measurements with YIG/Pt devices is feasible, I find a weaker effect of spin-torque than expected from previous Pt/Py measurements. This may suggest that the YIG/Pt interface can be improved. Overall, ST-FMR provides a quantitative technique for characterizing the spin-transfer torque in these systems.

6.3 Conclusion

In this chapter, I have shown that the SMR and ST-FMR techniques provide electrical detection of spin-transfer torque on iron garnets. The ability to make these measurements on a common iron garnet sample with a simple fabrication process, compared to the nanomagnets of Chapter 5, will allow many samples to be characterized. This is important to establish if there is a significant effect of spin transparency, or variation in the interface quality between samples. While

my preliminary analysis provides an initial quantification of spin-torque, further research is necessary to establish the SMR analysis method for relating the misalignment angle with the torque, and to examine different thicknesses with both techniques to determine agreement between them. Overall, these results lay the groundwork for the next stage of investigating spin-transfer torque in iron garnets.

APPENDIX A

PYMEASURE AUTOMATION SOFTWARE

This appendix gives a basic overview of the PyMeasure software and provides directions to access the software documentation and source-code.

PyMeasure makes scientific measurements easy to set up and run. The package contains a repository of instrument classes and a system for running experiment procedures, which provides graphical interfaces for graphing live data and managing queues of experiments. Both parts of the package are independent, and when combined provide all the necessary requirements for advanced measurements with only limited coding.

We published the source code under the open-source MIT license on GitHub.

`https://github.com/ralph-group/pymeasure`

Documentation for the software can be found at ReadTheDocs.

`http://pymeasure.readthedocs.io/en/latest/`

APPENDIX B

FABRICATION WORKSHEETS

The following pages of this appendix contain the worksheets that I developed to ensure accurate and efficient fabrication of the nanomagnetic devices, which I discuss in Chapter 5.

Sample: | Date

Version 5 Layer 1: Marks – Magnetic Insulator Switching Experiment

(1.1) ☐Clean Sample: ☐Acetone (sonicate ~5 min), ☐IPA, ☐Dry with Nitrogen

(1.2) ☐Dehydration bake at 180° C for more than 4 min (SU-8 spinner room)

(1.3) ☐Spin resist stack

	Resist	Spin	Pre-bake	Approx. Thickness
☐	LOR3A	3 krpm, 60 sec	180° C, 5 min	330 nm
☐	S1805	3 krpm, 60 sec	115° C, 1 min 30 sec	500 nm

(1.4) ☐Expose in 5x using mask *V4 L1 Marks* (8/11/14)

— exposure time: 0.27 sec, mode: transparent, focus: 77

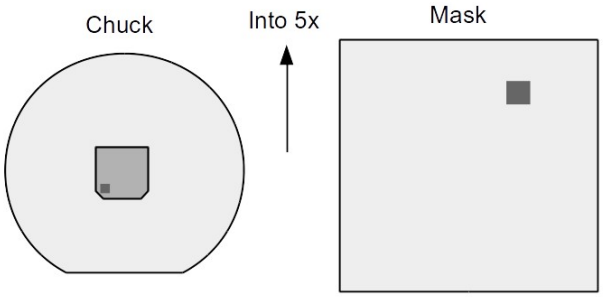

(1.5) ☐Develop in MIF 726 for 1 min 20 sec

(1.6) ☐Rinse with DI water, ☐Dry with Nitrogen

(1.7) ☐Back-sputter clean process for 60 sec in CNF AJA to descum

(1.8) ☐Sputter deposit in AJA: ☐Ti (5 nm, 30 sec) / ☐Pt (150 nm, 320 sec)

(1.9) ☐Soak in 1165 to liftoff (sonicate as necessary)

(1.10) ☐Rinse in IPA, ☐Dry with Nitrogen

Notes:

Sample: | Date

Version 5 Layer 2: Magnets – Magnetic Insulator Switching Experiment

(2.1) ☐Clean Sample: ☐Acetone (sonicate), ☐IPA, ☐Dry with Nitrogen

(2.2) ☐Dehydration bake at 170° C for more than 4 min

(2.3) ☐Spin e-beam resist stack

	Resist	Spin	Pre-bake	Approx. Thickness
☐	Omnicoat	3 krpm, 60 sec	170° C, 1 min	13 nm
☐	PMMA 495 K 4%	3 krpm, 60 sec	170° C, 2 min	168 nm
☐	HSQ (XR-1541) 6%	3 krpm, 60 sec	170° C, 1 min	96 nm

(2.4) ☐E-beam expose small features in JEOL 6300 using 1 nA (*clj72_1nA_Ap60)*

(2.4.1) ☐Measure P and Q marks relative to reference mark before loading

P mark	X:	Y:
Q mark	X:	Y:

(2.4.2) ☐Correct for wobble on lens 4 using SEM on BE mark

Initial Aperture	X:	Y:
Final Aperture	X:	Y:

(2.4.3) ☐Correct for astigmatism using BSEM on gold particles

Initial Stig.	X:	Y:
Final Stig.	X:	Y:

(2.4.4) ☐Preform calibration: *INITBE, INITAE, SFOCUS, PDEF, SUBDEF, DISTBE*

(2.4.5) ☐Measure the reference mark using BSEM at last known location

Reference	X:	Y:

Notes:

Sample: | | Date | |

(2.4.6) ☐ Compute expected P position from the JEOL 6300 Settings spreadsheet

P expected	X:	Y:

(2.4.7) ☐ Measure actual position of the P mark using the BSEM

P actual	X:	Y:

(2.4.8) ☐ Compute offset position from the JEOL 6300 Settings spreadsheet

Offset	X:	Y:

(2.4.9) ☐ Apply previous gains to *SETWFR* and *CHIPAL* or use *AGCRG* (automatic)

BE Coarse: 1, BE Middle Gain: 5, Wave offset: 103

BE Fine gain: 0, BE Offset: 2293

(2.4.10) ☐ Run *SETWFR* with the P (-3000, 0) and Q (3000, 0) marks

Global mark dimensions: 500 µm and 5 µm

(2.4.11) ☐ Run *CHIPAL* with (-2900, 2900), (2900, 2900), (2900, -2900), (-2900, -2900)

Chip mark dimensions: 60 µm and 3 µm

(2.4.12) ☐ Update jobs with offset: L2_1nA.sdf and L2_10nA.sdf

Jobs directory: ~/job/user/clj72/Garnets/V5/

(2.4.13 ☐ Recompile the job (*schd L2_1nA* and *schd L2_10nA*)

(2.4.14) ☐ Check offset positions with array check program

(2.4.15) ☐ Apply BE mark position to *DRIFT* and *SAVE*

(2.4.16) ☐ Expose using file: L2_1nA.mgn

(2.5) ☐ E-beam expose large features in JEOL 6300 using 10 nA (*clj72_10nA_Ap60)*

(2.5.1) ☐ Correct for wobble on lens 4 using SEM on BE mark

Initial Aperture	X:	Y:
Final Aperture	X:	Y:

Notes:

Sample: _____ Date _____

(2.5.2) ☐ Correct for astigmatism using BSEM on gold particles

Initial Stig.	X:	Y:
Final Stig.	X:	Y:

(2.5.3) ☐ Preform calibration: *INITBE, INITAE, SFOCUS, PDEF, SUBDEF, DISTBE*

(2.5.4) ☐ Apply previous gains to *SETWFR* and *CHIPAL* or use *AGCRG* (automatic)

BE Coarse: 1, BE Middle Gain: 5, Wave offset: 103

BE Fine gain: 0, BE Offset: 2293

(2.5.5) ☐ Run *SETWFR* with the P (-3000, 0) and Q (3000, 0) marks

Global mark dimensions: 500 µm and 5 µm

(2.5.6) ☐ Run *CHIPAL* with (-2900, 2900), (2900, 2900), (2900, -2900), (-2900, -2900)

Chip mark dimensions: 60 µm and 3 µm

(2.5.7) ☐ Apply BE mark position to *DRIFT* and *SAVE*

(2.5.8) ☐ Expose at 500 µC/cm^2 using file: L2_10nA.mgn

(2.6) ☐ Develop in MIF 726 for 1 min 30 sec

(2.7) ☐ Rinse in DI water, ☐ Dry with Nitrogen

(2.8) ☐ Transfer pattern to PMMA/Omnicoat in Oxford 80 RIE

(2.8.1) ☐ Oxygen Clean to clean chamber before use for 5 min

(2.8.2) ☐ Oxygen Clean at 100 W, 50 mTorr, 20 sccm for 1 min 30 sec

---

Notes:

Sample: | Date

(2.9) ☐ Ion mill etch at 150 V accelerating voltage, 35 mA beam current

- (2.9.1) ☐ Etch at 170° for pillar etching
- (2.9.2) ☐ Stop etching at Ga / Gd signal from mass spectrometer
- (2.9.3) ☐ Etch at 110° to clean sidewall for 1 min

(2.10) ☐ Soak in Remover PG on hotplate (MEM2) for 6 hr to strip resist

(2.11) ☐ Sonicate for 1 hr in Remover PG

(2.12) ☐ Sonicate for 1 min in IPA, ☐ Dry with Nitrogen

Notes:

Sample: | Date

Version 5 Layer 3: Bridges – Magnetic Insulator Switching Experiment

(3.1) ☐Clean Sample: ☐Acetone (sonicate), ☐IPA, ☐Dry with Nitrogen

(3.2) ☐Dehydration bake at 170° C for more than 4 min

(3.3) ☐Spin e-beam resist stack

	Resist	Spin	Pre-bake	Approx. Thickness
☐	PMMA 495 K 4%	3 krpm, 60 sec	170° C, > 15 min	168 nm
☐	PMMA 950 K 2%	3 krpm, 60 sec	170° C, > 15 min	100 nm
☐	ESpacer 300Z	3 krpm, 60 sec	90° C, 1 min	19 nm

(3.4) ☐E-beam expose in JEOL 9300 at 1 nA (*clj72_1nA_Ap60)*

(3.4.1) ☐Measure P and Q marks relative to reference mark before loading

P mark	X:	Y:
Q mark	X:	Y:

(3.4.2) ☐Correct for wobble on lens 4 using SEM on BE mark

Initial Aperture	X:	Y:
Final Aperture	X:	Y:

(3.4.3) ☐Correct for astigmatism using BSEM on gold particles

Initial Stig.	X:	Y:
Final Stig.	X:	Y:

(3.4.4) ☐Preform calibration: *INITBE, INITAE, SFOCUS, PDEF, SUBDEF, DISTBE*

Notes:

Sample: | | Date | |

(3.4.5) ☐ Measure the reference mark using BSEM at last known location

Reference	X:	Y:

(3.4.6) ☐ Compute expected P position from the JEOL 6300 Settings spreadsheet

P expected	X:	Y:

(3.4.7) ☐ Measure actual position of the P mark using the BSEM

P actual	X:	Y:

(3.4.8) ☐ Compute offset position from the JEOL 6300 Settings spreadsheet

Offset	X:	Y:

(3.4.9) ☐ Apply previous gains to *SETWFR* and *CHIPAL* or use *AGCRG* (automatic)
BE Coarse: 1, BE Middle Gain: 5, Wave offset: 103
BE Fine gain: 0, BE Offset: 2293

(3.4.10) ☐ Run *SETWFR* with the P (-3000, 0) and Q (3000, 0) marks
Global mark dimensions: 500 μm and 5 μm

(3.4.11) ☐ Run *CHIPAL* with (-2900, 2900), (2900, 2900), (2900, -2900), (-2900, -2900)
Chip mark dimensions: 60 μm and 3 μm

(3.4.12) ☐ Update job with offset: ~/job/user/clj72/Garnets/V5/L3.sdf

(3.4.13) ☐ Recompile the job (*schd L3*)

(3.4.14) ☐ Check offset position with array check program

(2.4.15) ☐ Apply BE mark position to *DRIFT* and *SAVE*

(3.4.16) ☐ Expose at 700 μC/cm^2 using file: ~/job/user/clj72/Garnets/V5/L3.mgn

Notes:

Sample: | Date

(3.5) ☐ Rinse in DI water to remove ESpacer, ☐ Dry with Nitrogen

(3.6) ☐ Develop in MIBK : IPA (1:3) for 1 min

(3.7) ☐ Rinse in IPA, ☐ Dry with Nitrogen

(3.8) ☐ Back-sputter clean process for 60 sec in CNF AJA to descum

(3.9) ☐ Sputter deposit in AJA: ☐ Ti (5 nm, 30 sec) / ☐ Pt (100 nm, 213 sec)

(3.10) ☐ Soak in methylene chloride : acetone (1:1) to liftoff (sonicate as necessary)

(3.11) ☐ Rinse in IPA, ☐ Dry with Nitrogen

Notes:

Sample: | Date

Version 5 Layer 4: Oxide – Magnetic Insulator Switching Experiment

(1.1) ☐Clean Sample: ☐Acetone (sonicate ~5 min), ☐IPA, ☐Dry with Nitrogen

(1.2) ☐Dehydration bake at 180° C for more than 4 min (SU-8 spinner room)

(1.3) ☐Spin resist stack

	Resist	Spin	Pre-bake	Approx. Thickness
☐	LOR3A	3 krpm, 60 sec	180° C, 5 min	330 nm
☐	S1805	3 krpm, 60 sec	115° C, 1 min 30 sec	500 nm

(1.4) ☐Expose in 5x using *V5 L4 Oxide* (07/17/15)

— exposure time: 0.27 sec, mode: transparent, focus: 77

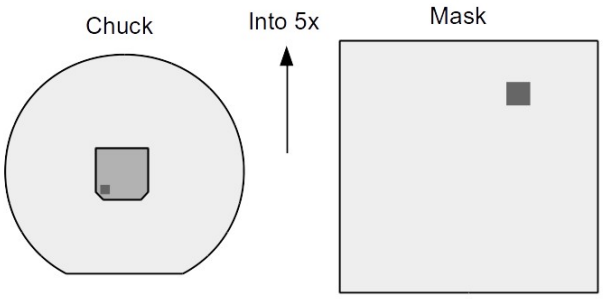

(1.5) ☐Develop in MIF 726 for 1 min 20 sec

(1.6) ☐Rinse with DI water, ☐Dry with Nitrogen

(1.7) ☐Back-sputter clean process for 60 sec in CNF AJA to descum

(1.8) ☐Sputter deposit in AJA: ☐SiO2 (100 nm, 1250 sec)

(1.9) ☐Soak in 1165 to liftoff (sonicate as necessary)

(1.10) ☐Rinse in IPA, ☐Dry with Nitrogen

Notes:

Sample: | Date

Version 5 Layer 5: Leads – Magnetic Insulator Switching Experiment

(5.1) ☐Clean Sample: ☐Acetone (sonicate ~5 min), ☐IPA, ☐Dry with Nitrogen

(5.2) ☐Dehydration bake at 180° C for more than 4 min (SU-8 spinner room)

(5.3) ☐Spin resist stack

	Resist	Spin	Pre-bake	Approx. Thickness
☐	LOR3A	3 krpm, 60 sec	180° C, 5 min	330 nm
☐	S1805	3 krpm, 60 sec	115° C, 1 min 30 sec	500 nm

(5.4) ☐Expose in 5x using *V5 L5 Leads* (02/11/15)

— exposure time: 0.27 sec, mode: transparent, focus: 77

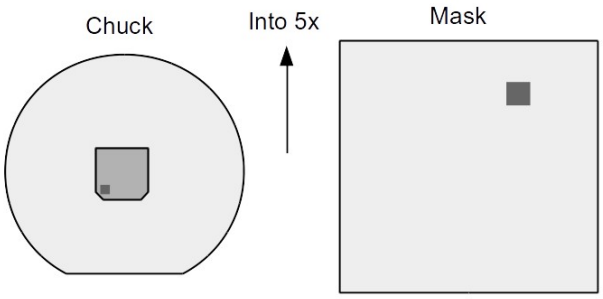

(5.5) ☐Develop in MIF 726 for 1 min 20 sec

(5.6) ☐Rinse with DI water, ☐Dry with Nitrogen

(5.7) ☐Back-sputter clean process for 60 sec in CNF AJA to descum

(5.8) ☐Sputter deposit in AJA: ☐Ti (5 nm, 30 sec) / ☐Pt (200 nm, 426 sec)

(5.9) ☐Soak in 1165 to liftoff (sonicate as necessary)

(5.10) ☐Rinse in IPA, ☐Dry with Nitrogen

Notes:

Sample: | Date

Version 5 Packaging 1: Dicing – Magnetic Insulator Switching Experiment

(1.1) ☐Clean Sample: ☐Acetone (sonicate ~5 min), ☐IPA, ☐Dry with Nitrogen

(1.2) ☐Spin resist stack to protect top surface

	Resist	Spin	Pre-bake	Approx. Thickness
☐	S1805	3 krpm, 60 sec	115° C, 1 min 30 sec	500 nm

(1.3) ☐Dice along S-V marks to separate chips

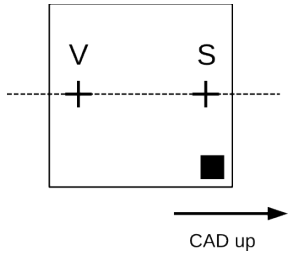

(1.4) ☐Dice along the P mark

(1.5) ☐Dice along

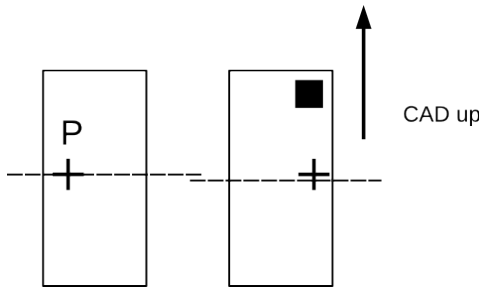

(1.6) ☐Soak in 1165 to remove resist (sonicate as necessary)

(1.7) ☐Rinse in IPA, ☐Dry with Nitrogen

Notes:

BIBLIOGRAPHY

[1] L. Liu, C.-F. Pai, Y. Li, H. W. Tseng, D. C. Ralph, and R. A. Buhrman, Science **336**, 555 (2012).

[2] C. L. Jermain, H. Paik, S. V. Aradhya, R. A. Buhrman, D. G. Schlom, and D. C. Ralph, Appl. Phys. Lett. **109**, 192408 (2016).

[3] E. Anderson, Phys. Rev. **134**, A1581 (1964).

[4] R. O'Handley, *Modern Magnetic Materials* (Wiley, 2000).

[5] J. Slonczewski, J. Magn. Magn. Mater. **159**, L1 (1996).

[6] L. Liu, R. A. Buhrman, and D. C. Ralph, (2011), arXiv:1111.3702 .

[7] C.-F. Pai, L. Liu, Y. Li, H. W. Tseng, D. C. Ralph, and R. a. Buhrman, Appl. Phys. Lett. **101**, 122404 (2012).

[8] Y. Sun and M. Wu, Solid State Phys. **64**, 157 (2013).

[9] A. R. Mellnik, J. S. Lee, A. Richardella, J. L. Grab, P. J. Mintun, M. H. Fischer, A. Vaezi, A. Manchon, E. A. Kim, N. Samarth, and D. C. Ralph, Nature **511**, 449 (2014).

[10] Y. Fan, P. Upadhyaya, X. Kou, M. Lang, S. Takei, Z. Wang, J. Tang, L. He, L.-t. Chang, M. Montazeri, G. Yu, W. Jiang, T. Nie, R. N. Schwartz, Y. Tserkovnyak, and K. L. Wang, Nat. Mater. **13**, 699 (2014).

[11] M. Sparks, *Ferromagnetic-Relaxation Theory* (McGraw-Hill, New York, 1964) p. 226.

[12] S. S. Kalarickal, P. Krivosik, M. Wu, C. E. Patton, M. L. Schneider, P. Kabos, T. J. Silva, and J. P. Nibarger, J. Appl. Phys. **99**, 093909 (2006).

[13] C. Bilzer, T. Devolder, P. Crozat, C. Chappert, S. Cardoso, and P. P. Freitas, J. Appl. Phys. **101**, 074505 (2007).

[14] T. Anderson, in *1999 IEEE International Symposium on Electromagnetic Compatability. Symposium Record (Cat. No.99CH36261)*, Vol. 2 (IEEE, 1999) pp. 601–604.

[15] E. R. Javor and T. Anderson, in *Electromagnetic Compatibility, 1998. 1998 IEEE International Symposium on*, Vol. 2 (1998) pp. 912–917.

[16] *The Design & Test of Broadband Launches up to 50 GHz on Thin & Thick Substrates*, Tech. Rep. (Southwest Microwave, Tempe, AZ).

[17] B. C. Wadell, *Transmission Line Design Handbook* (Artech House, Boston, MA, 1991).

[18] K. C. Gupta, R. Garg, I. Bahl, and P. Bhartia, *Microstrip Lines and Slotlines*, 2nd ed. (Artech House, Boston, MA, 1996) p. 535.

[19] D. Pozar, *Microwave Enginnering*, 4th ed. (John Wiley & Sons, 2012).

[20] I. M. Miron, K. Garello, G. Gaudin, P.-J. Zermatten, M. V. Costache, S. Auffret, S. Bandiera, B. Rodmacq, A. Schuhl, and P. Gambardella, Nature **476**, 189 (2011).

[21] O. d'Allivy Kelly, A. Anane, R. Bernard, J. Ben Youssef, C. Hahn, A. H. Molpeceres, C. Carretero, E. Jacquet, C. Deranlot, P. Bortolotti, R. Lebourgeois, J.-C. Mage, G. de Loubens, O. Klein, V. Cros, and A. Fert, Appl. Phys. Lett. **103**, 082408 (2013).

[22] C. Hahn, V. V. Naletov, G. de Loubens, O. Klein, O. d'Allivy Kelly,

A. Anane, R. Bernard, E. Jacquet, P. Bortolotti, V. Cros, J. L. Prieto, and M. Muñoz, Appl. Phys. Lett. **104**, 152410 (2014).

[23] M. Montazeri, P. Upadhyaya, M. C. Onbasli, G. Yu, K. L. Wong, M. Lang, Y. Fan, X. Li, P. Khalili Amiri, R. N. Schwartz, C. A. Ross, and K. L. Wang, Nat. Commun. **6**, 8958 (2015).

[24] A. Hamadeh, O. d'Allivy Kelly, C. Hahn, H. Meley, R. Bernard, A. H. Molpeceres, V. V. Naletov, M. Viret, A. Anane, V. Cros, S. O. Demokritov, J. L. Prieto, M. Muñoz, G. de Loubens, and O. Klein, Phys. Rev. Lett. **113**, 197203 (2014).

[25] H. L. Wang, C. H. Du, Y. Pu, R. Adur, P. C. Hammel, and F. Y. Yang, Phys. Rev. Lett. **112**, 197201 (2014).

[26] S. Geller, A. Paoletti, P. Hansen, J. C. Slonczewski, A. P. Malozemoff, P. E. Wigen, R. W. Teale, A. Tucciarone, U. Enz, J. F. Dillon, R. Metselaar, P. K. Larsen, G. B. Scott, C. Rudowicz, W. Jantz, W. Wettling, J. Schneider, R. Krishnan, and W. Tolksdorf, *Proc. Int'l School Phys.Enrico Fermi, Course LXX*, edited by A. Paoletti, Vol. 14 (North-Holland Company, Amsterdam, 1978) pp. 1490–1490.

[27] D. G. Schlom, L. Chen, X. Pan, A. Schmehl, and M. A. Zurbuchen, J. Am. Ceram. Soc. **91**, 2429 (2008).

[28] L. Van Uitert, E. Gyorgy, W. Bonner, W. Grodkiewicz, E. Heilner, and G. Zydzik, Mater. Res. Bull. **6**, 1185 (1971).

[29] S. Geller and M. M. Gilleo, J. Phys. Chem. Solids **3**, 30 (1957).

[30] G. P. Espinosa, J. Chem. Phys. **37**, 2344 (1962).

[31] H. L. Wang, C. H. Du, Y. Pu, R. Adur, P. C. Hammel, and F. Y. Yang, Phys. Rev. B **88**, 100406 (2013).

[32] T. Liu, H. Chang, V. Vlaminck, Y. Sun, M. Kabatek, A. Hoffmann, L. Deng, and M. Wu, J. Appl. Phys. **115**, 17A501 (2014).

[33] H. Chang, P. Li, W. Zhang, T. Liu, A. Hoffmann, L. Deng, and M. Wu, IEEE Magn. Lett. **5**, 1 (2014).

[34] J. T. Brangham, K.-Y. Meng, A. S. Yang, J. C. Gallagher, B. D. Esser, S. P. White, S. Yu, D. W. McComb, P. C. Hammel, and F. Yang, Phys. Rev. B **94**, 054418 (2016).

[35] P. C. Dorsey, S. E. Bushnell, R. G. Seed, and C. Vittoria, J. Appl. Phys. **74**, 1242 (1993).

[36] S. A. Manuilov, S. I. Khartsev, and A. M. Grishin, J. Appl. Phys. **106**, 123917 (2009).

[37] S. A. Manuilov and A. M. Grishin, J. Appl. Phys. **108**, 013902 (2010).

[38] B. Heinrich, C. Burrowes, E. Montoya, B. Kardasz, E. Girt, Y.-Y. Song, Y. Sun, and M. Wu, Phys. Rev. Lett. **107**, 066604 (2011).

[39] M. C. Onbasli, A. Kehlberger, D. H. Kim, G. Jakob, M. Kläui, A. V. Chumak, B. Hillebrands, and C. A. Ross, APL Materials **2**, 106102 (2014).

[40] B. M. Howe, S. Emori, Hyung-Min Jeon, T. M. Oxholm, J. G. Jones, K. Mahalingam, Yan Zhuang, N. X. Sun, and G. J. Brown, IEEE Magn. Lett. **6**, 3500504 (2015).

[41] C. Tang, M. Aldosary, Z. Jiang, H. Chang, B. Madon, K. Chan, M. Wu, J. E. Garay, and J. Shi, Appl. Phys. Lett. **108**, 102403 (2016).

[42] Y. Sun, Y.-Y. Song, H. Chang, M. Kabatek, M. Jantz, W. Schneider, M. Wu, H. Schultheiss, and A. Hoffmann, Appl. Phys. Lett. **101**, 152405 (2012).

[43] C. Hauser, T. Richter, N. Homonnay, C. Eisenschmidt, M. Qaid, H. Deniz, D. Hesse, M. Sawicki, S. G. Ebbinghaus, and G. Schmidt, Sci. Rep. **6**, 20827 (2016).

[44] A. Ichimiya and P. I. Cohen, *Reflection High-Energy Electron Diffraction* (Cambridge University Press, Cambridge, 2004).

[45] D. Stancil and A. Prabhakar, *Spin Waves* (Springer US, Boston, MA, 2009).

[46] R. Arias and D. L. Mills, Phys. Rev. B **60**, 7395 (1999).

[47] D. L. Mills and S. M. Rezende, Top. Appl. Phys. **87**, 27 (2003).

[48] K. Lenz, H. Wende, W. Kuch, K. Baberschke, K. Nagy, and A. Jánossy, Phys. Rev. B **73**, 144424 (2006).

[49] A. Azevedo, A. B. Oliveira, F. M. de Aguiar, and S. M. Rezende, Phys. Rev. B **62**, 5331 (2000).

[50] S. A. Manuilov and P. A. Grünberg, J. Magn. Magn. Mater. **340**, 32 (2013).

[51] D. C. Worledge, G. Hu, D. W. Abraham, J. Z. Sun, P. L. Trouilloud, J. Nowak, S. Brown, M. C. Gaidis, E. J. O'Sullivan, and R. P. Robertazzi, Appl. Phys. Lett. **98**, 022501 (2011).

[52] A. A. Jalali, S. Kahl, V. Denysenkov, and A. M. Grishin, Phys. Rev. B **66**, 104419 (2002).

[53] A. M. Kalashnikova, V. V. Pavlov, A. V. Kimel, A. Kirilyuk, T. Rasing, and R. V. Pisarev, Low Temp. Phys. **38**, 863 (2012).

[54] H. Wang, C. Du, P. C. Hammel, and F. Yang, Phys. Rev. Lett. **113**, 097202 (2014).

[55] M. Haidar, M. Ranjbar, M. Balinsky, R. K. Dumas, S. Khartsev, and J. kerman, J. Appl. Phys. **117**, 17D119 (2015).

[56] J. R. Kirtley, L. Paulius, A. J. Rosenberg, J. C. Palmstrom, C. M. Holland, E. M. Spanton, D. Schiessl, C. L. Jermain, J. Gibbons, Y. K. K. Fung, M. E. Huber, D. C. Ralph, M. B. Ketchen, G. W. Gibson, and K. A. Moler, Rev. Sci. Instrum. **87**, 093702 (2016).

[57] J. F. Dillon and J. W. Nielsen, Phys. Rev. Lett. **3**, 30 (1959).

[58] E. G. Spencer, R. C. LeCraw, and R. C. Linares, Phys. Rev. **123**, 1937 (1961).

[59] P. E. Seiden, Phys. Rev. **133**, A728 (1964).

[60] W. P. Wolf, M. Ball, M. T. Hutchings, M. J. M. Leask, and A. F. G. Wyatt, J. Phys. Soc. Japan **17**, 443 (1962).

[61] W. Gunsser, U. Wolfmeier, and J. Fleischhauer, in *Part A: Garnets and Perovskites*, edited by K.-H. Hellwege and A. M. Hellwege (Springer Berlin Heidelberg, Berlin/Heidelberg, 1978) pp. 272–275.

[62] E. Shigematsu, Y. Ando, R. Ohshima, S. Dushenko, Y. Higuchi, T. Shinjo, H. Jürgen von Bardeleben, and M. Shiraishi, Appl. Phys. Express **9**, 053002 (2016).

[63] M. Maryško, Czechoslov. J. Phys. **39**, 116 (1989).

[64] M. Maryško, J. Magn. Magn. Mater. **101**, 159 (1991).

[65] H. Callen and E. Callen, J. Phys. Chem. Solids **27**, 1271 (1966).

[66] D. P. Pappas, J. Vac. Sci. Technol. B Microelectron. Nanom. Struct. **14**, 3203 (1996).

[67] C. Kittel, J. Appl. Phys. **31**, S11 (1960).

[68] A. M. Clogston, Bell Syst. Tech. J. **34**, 739 (1955).

[69] C. O. Avci, A. Quindeau, C.-F. Pai, M. Mann, L. Caretta, A. S. Tang, M. C. Onbasli, C. A. Ross, and G. S. D. Beach, Nat. Mater. **1** (2016), 10.1038/nmat4812.

[70] M. Aldosary, J. Li, C. Tang, Y. Xu, J.-G. Zheng, K. N. Bozhilov, and J. Shi, Appl. Phys. Lett. **108**, 242401 (2016).

[71] H. Li, D. B. Farmer, R. G. Gordon, Y. Lin, and J. Vlassak, J. Electrochem. Soc. **154**, D642 (2007).

[72] Q. Hao and G. Xiao, Phys. Rev. B **91**, 224413 (2015).

[73] L. Liu, *Manipulation of Magnetic Moment Using the Spin Current from Magnetic and Non-Magnetic Materials*, Ph.D. thesis, Cornell University (2012).

[74] F. J. Albert, *The Fabrication and Measurement of Current Perpendicular To the Plane Magnetic Nanostructures for the Study of the Spin Transfer Effect*, Ph.D. thesis, Cornell University (2003).

[75] J. R. Kirtley, L. Paulius, A. J. Rosenberg, J. C. Palmstrom, D. Schiessl, C. L. Jermain, J. Gibbons, C. M. Holland, Y.-K.-K. Fung, M. E. Huber, M. B. Ketchen, D. C. Ralph, G. W. Gibson, and K. A. Moler, Supercond. Sci. Technol. **29**, 124001 (2016).

[76] C. F. Pai, Y. Ou, L. H. Vilela-Leão, D. C. Ralph, and R. A. Buhrman, Phys. Rev. B **92**, 064426 (2015).

[77] W. Zhang, W. Han, X. Jiang, S.-H. Yang, and S. S. P. Parkin, Nature Phys. **11**, 496 (2015).

[78] C. Hahn, G. De Loubens, O. Klein, M. Viret, V. V. Naletov, and J. Ben Youssef, Phys. Rev. B **87**, 174417 (2013).

[79] L. Liu, T. Moriyama, D. C. Ralph, and R. A. Buhrman, Phys. Rev. Lett. **106**, 036601 (2011).

[80] K. Ando, S. Takahashi, K. Harii, K. Sasage, J. Ieda, S. Maekawa, and E. Saitoh, Phys. Rev. Lett. **101**, 036601 (2008).

[81] C.-F. Pai, L. Liu, Y. Li, H. W. Tseng, D. C. Ralph, and R. A. Buhrman, Appl. Phys. Lett. **101**, 122404 (2012).

[82] T. Chiba, G. E. Bauer, and S. Takahashi, Phys. Rev. Appl. **2**, 034003 (2014).

[83] J. Sklenar, W. Zhang, M. B. Jungfleisch, W. Jiang, H. Chang, J. E. Pearson, M. Wu, J. B. Ketterson, and A. Hoffmann, Phys. Rev. B **92**, 174406 (2015).

[84] M. B. Jungfleisch, W. Zhang, J. Sklenar, J. Ding, W. Jiang, H. Chang, F. Y. Fradin, J. E. Pearson, J. B. Ketterson, V. Novosad, M. Wu, and A. Hoffmann, Phys. Rev. Lett. **116**, 057601 (2016).

[85] A. Mellnik, *Measurements Of Spin Torques Generated By Topological Insulators And Heavy Metals*, Ph.D. thesis, Cornell University (2015).